In Vivo Examination of Lamina Cribrosa Microarchitecture and Optic Nerve Head Geometry in Normal Human Aging and Early Glaucoma

By

Amitabha S. Bhakta
B.Optom.

DISSERTATION

In partial satisfaction of the requirements for the degree of

DOCTOR OF PHILOSOPHY

in

PHYSIOLOGICAL OPTICS

Presented to the

Graduate Faculty

of the

College of Optometry
University of Houston

May, 2016

Approved:

Jason Porter, Ph.D. (Chair)

Laura J. Frishman, Ph.D.

Nimesh B. Patel, O.D., Ph.D.

Danica J Marrelli, O.D.

Christopher C. Bowd, Ph.D.

Committee in Charge

Acknowledgements

First and foremost, my sincere and heartiest thanks to my advisor, Jason Porter for all the guidance, support, motivation and help since the day I joined the lab. I would also extend my thanks to Laura J Frishman for her sustained guidance during the entire length of my graduate studies at University of Houston. I am very grateful to my family, friends and fellow graduate students for the motivation, inspiration, and support provided by them throughout my life and career. I would also like to grab this opportunity to thank my other committee members, Danica J Marrelli, Nimesh B Patel, Christopher Bowd, Ronald Harwerth and Michael D Twa for advice, guidance and encouragement. I would like to thank for all the help and support from Hope Queener, Nripun Sredar, Kevin Ivers, Gongpu Lan, Alex Schill and Harold E Bedell at University of Houston, College of Optometry. Finally I would also like to acknowledge the grant support by NIH grants R01 EY021783 and P30 EY07551.

In Vivo Examination of Lamina Cribrosa Microarchitecture and Optic Nerve Head Geometry in Normal Human Aging and Early Glaucoma

By

Amitabha S. Bhakta, B.Optom.

DISSERTATION

In partial satisfaction of the requirements for the degree of

DOCTOR OF PHILOSOPHY

in

PHYSIOLOGICAL OPTICS

Presented to the Graduate Faculty of the

College of Optometry
University of Houston

May 2016

Abstract

Purpose: The lamina cribrosa likely plays an important role in the pathogenesis of glaucoma. The goals of this dissertation were to better understand differences in lamina cribrosa microarchitecture and optic nerve head (ONH) geometry in normal human eyes with axial length and aging and determine whether any differences found in older, normal eyes were similar to changes associated with early glaucoma, but potentially to a lesser extent.

Methods: (1) Images of the ONH were acquired via spectral domain optical coherence tomography (SDOCT) and used to quantify Bruch's Membrane Opening (BMO) area, mean anterior lamina cribrosa surface depth (ALCSD), mean minimum rim width (MRW) and scaled MRW in young normal subjects to examine ONH structure in eyes with different axial lengths. (2) The aforementioned and additional SDOCT parameters (anterior lamina cribrosa surface [ALCS] radius of curvature [RoC], prelaminar tissue volume [PTV], neuroretinal rim volume) were quantified in normal young (20-30 years) and older (> 50 years) eyes. Images of the ALCS microarchitecture were acquired using adaptive optics and used to quantify mean ALCS pore area, elongation, and nearest neighbor distance (NND). ALCS pore and ONH parameters were compared between fellow eyes of normal subjects and between young and older normal eyes. (3) Images of the ONH and ALCS microarchitecture were also acquired in glaucoma suspects and primary open angle glaucoma (POAG) patients. Global and local ALCS pore geometries and ONH parameters were compared between suspect/POAG and age-matched normal eyes. The relationships between ONH and ALCS pore parameters were also examined.

Results: (1) Mean MRW was significantly thinner in young, normal eyes with more

posteriorly-located laminar surfaces (*P*<.01) and larger BMO areas (*P*<.01). However, scaled MRW and BMO area were not correlated (*P*=.77), potentially indicating that all eyes have the same number of axons regardless of the size of the disc. While eyes with longer axial lengths had larger BMO areas (*P*<.01), no significant relationships were found between axial length and mean MRW (*P*=.09) or mean ALCSD (*P*=.07). (2) ONH and mean global ALCS pore parameters were not statistically different between fellow normal eyes. With the exception of mean MRW (significantly thinner in older eyes), all ONH and ALCS pore parameters were similar between older and young eyes. (3) PTV, rim volume, mean MRW and mean RNFL thickness were significant reduced, and ALCS was more posteriorly located and more steeply curved in suspect/POAG eyes compared to normal eyes. ALCS pores were more closely spaced (smaller global mean NND) in suspect/POAG eyes. Local pore analyses revealed that ALCS pores were significantly smaller in the superior-temporal sector of suspect/POAG eyes compared to normal eyes (*P*=.03). In addition, there were no significant relationships between any ALCS pore and ONH parameter within older normal eyes or suspect/POAG eyes.

Conclusions: This dissertation provides increased understanding of ONH and laminar structure in normal young and older eyes, as well as differences in these structural properties between normal and suspect/POAG eyes. The larger BMO areas found in young eyes with increased axial lengths could result from retinal and scleral stretching forces that occur during development. As the normal eye ages, there is a reduction in mean MRW that likely reflects an age-related loss in retinal ganglion cell axons. In addition to profound differences in ONH structure, we found significant differences in ALCS pore area in the superior-temporal sector of suspect/POAG eyes (relative to normal, older eyes), corresponding to a region that is known to be prone to the development of retinal nerve fiber layer defects in glaucoma.

Table of Contents

List of Figures

List of Tables

CHAPTER 1

General Introduction

1.1 Introduction

Glaucoma is the leading cause of irreversible blindness worldwide. The number of individuals with glaucoma in 2010 was estimated to be about 60.5 million (Quigley and Broman, 2006). This estimate increased to 64.3 million in 2013 (Tham et al., 2014) and is projected to rise to 76.0 million in 2020 and 111.8 million in 2040. This rapid increase in the number of individuals with glaucoma is attributed to an increase in the aging population worldwide, as well as an increased rate of affected individuals in Asia and Africa (Figure 1-1).

The risk and type of glaucoma varies accross races and continents. The prevalence of primary open angle glaucoma (POAG) is highest in Africa and people with African ansestry (Rudnicka et al., 2006) while the prevalence of Primary Angle Closure Glaucoma (PACG) is highest in Asia (Foster and Johnson, 2001). North America is estimated to have almost 4 million people affected by glaucoma in 2020 (Tham et al., 2014). In the United States, more than 130,000 people were estimated to be blind due to glaucoma in 2000 (Quigley and Vitale, 1997). Glaucoma accounts for over 10 million visits to Optometrists and Ophthalmologists every year, resulting in an expense to the United States government of more than $1.5 billion annually (Center for Disease Control and Prevention/National Center for Health Statistics, 2010 & 1995; NEI, Report of the Glaucoma Panel, Fall 1998). Given the potential impact of glaucoma on the visual system, as well as this increasing financial burden, it is important to identify the mechanisms for this disease, as well as suitable treatments.

The work in this dissertation begins by quantifying relationships in ONH and lamina cribrosa structure in young, normal eyes of different axial lengths. Next, the dissertation examines inter-eye differences in anterior lamina cribrosa surface (ALCS) microarchitecture and ONH structure *in vivo* in normal human eyes, followed by a characterization of differences in ALCS microarchitecture and ONH structure between

normal, young and older eyes. The dissertation concludes with a comparison of structural differences in the ONH and ALCS microarchitecture between older, normal eyes and eyes diagnosed as glaucoma suspects or with POAG.

.

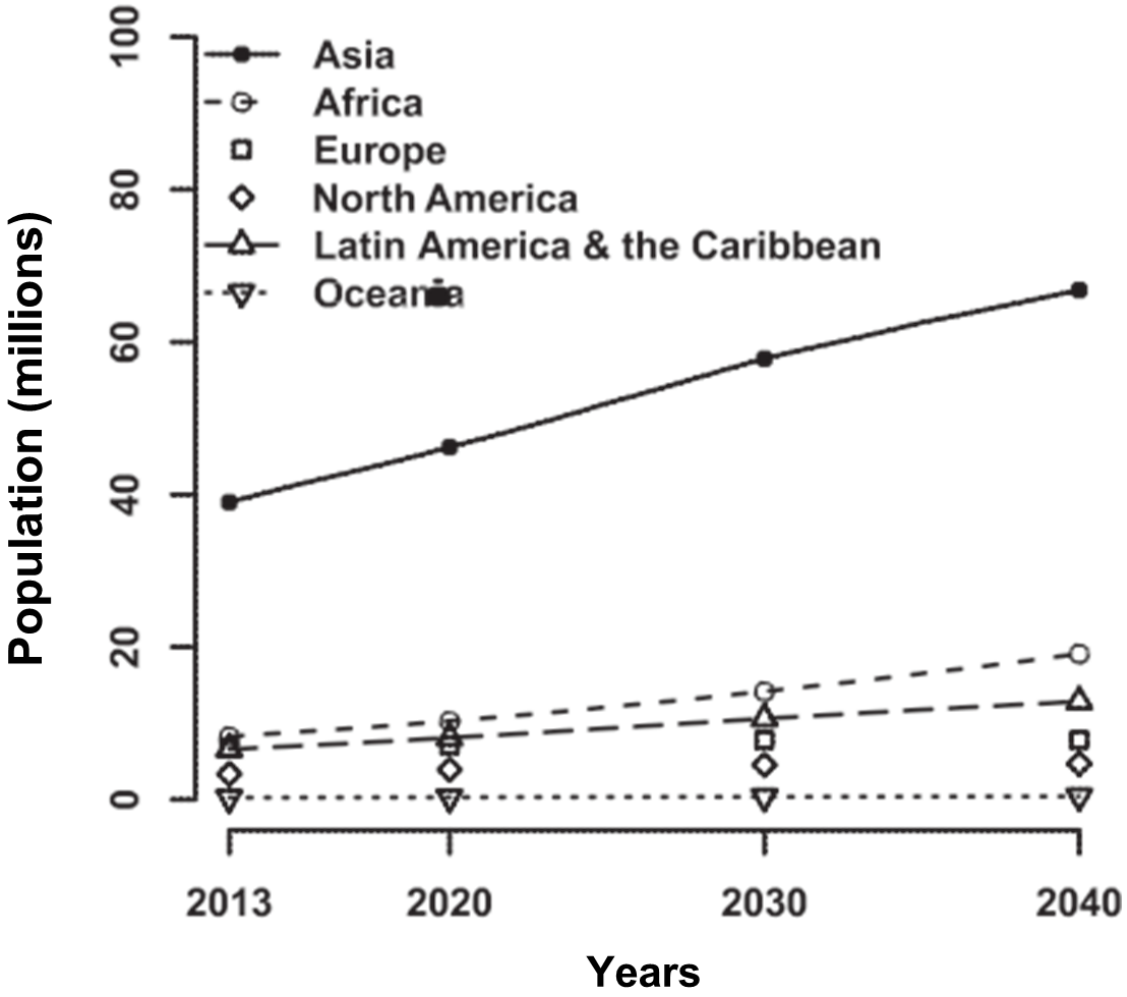

Figure 1-1. Projected rate of increase in individuals with glaucoma worldwide based on geographical region from 2013 through 2040. These projections are based on a meta analysis performed on data from major population-based studies of glaucoma prevalence. Reprinted with permission (Tham et al., 2014).

1.2 Glaucoma as a disease and hypotheses of its pathophysiology

Glaucoma is defined as a group of progressive optic neuropathies that results in the death of retinal ganglion cells (Quigley et al., 1981). This condition clinically presents as structural changes in optic nerve head (ONH) cupping, retinal nerve fiber (RNFL) thinning and functional losses in vision (Quigley and Broman, 2006) (Figure 1-2). Multiple studies have reported a deepening of the ONH in early glaucoma, as the connective tissue within the ONH posteriorly deforms and bows backwards (Figure 1-3) (Burgoyne, 2011; Quigley, 2011). Several reports based on animal models have also shown that damage to retinal ganglion cell (RGC) axons is central to the pathophysiology of glaucoma (Johnson et al., 1996; Burgoyne et al., 2004; Downs et al., 2007; Howell et al., 2007; Yang et al., 2010).

The lamina cribrosa has been suggested as the initial site of damage to RGC axons in glaucoma (Quigley and Anderson, 1976a). For example, alterations and disruptions in axoplasmic flow have been reported to occur within the lamina cribrosa following the elevation of intraocular pressure (IOP) in normal, non-human primate eyes (Anderson and Hendrickson, 1974; Quigley and Anderson, 1976a; Minckler et al., 1977). While the mechanisms underlying RGC axonal damage are not well understood, several factors likely contribute to the onset and progression of glaucomatous neuropathy. Currently, three main hypotheses have been proposed to describe how axons are damaged in glaucoma. The mechanical hypothesis suggests that an increase in IOP imparts stress on the lamina cribrosa, which, in turn, results in a strain and deformation of the entire laminar structure. These deformations can include alterations in the biomechanical dynamics (or compliance) of the load-bearing laminar beams, as well as changes in laminar beam and pore microarchitecture that can subsequently result in mechanical alterations (e.g., compression, shearing) of the RGC axons passing through the altered pore structure (Bellezza, 2000; Bellezza et al., 2003; Burgoyne et al., 2005;

Downs et al., 2008; Roberts et al., 2009b; Sigal and Ethier, 2009). The vascular theory suggests that increase in IOP and alterations in Cerebrospinal Fluid (CSF) pressure causes a change in the trans-laminar pressure gradient, which results in perfusion instabilities within the ONH. This imbalance gives rise to alterations in ocular blood flow and a reduced blood supply to ONH and laminar capillaries that nourish RGC axons, ultimately leading to their demise (Fechtner and Weinreb, 1994; Grieshaber et al., 2007; Jonas et al., 2013). The glial hypothesis suggests that increases in IOP result in an activation of astrocytes and glial cells that initially serves to protect the neuronal tissue. However, this activated response could also reduce neurotrophic support to RGC axons and create a harmful, neurotoxic environment (Neufeld et al., 1997; Hernandez, 2000; Tezel, 2009). For example, studies in human glaucoma and in a rat model of experimental glaucoma suggest that reactive astrocytes and other glial cells synthesize nitric oxide synthase (NOS-2), an enzyme that may be neurotoxic to RGC axons in the ONH (Neufeld et al., 1997; Neufeld, 1999; Neufeld et al., 1999). However, it is likely that all of these hypothesized mechanism contribute to the onset and progression of glaucoma and that none of these hypotheses are mutually exclusive.

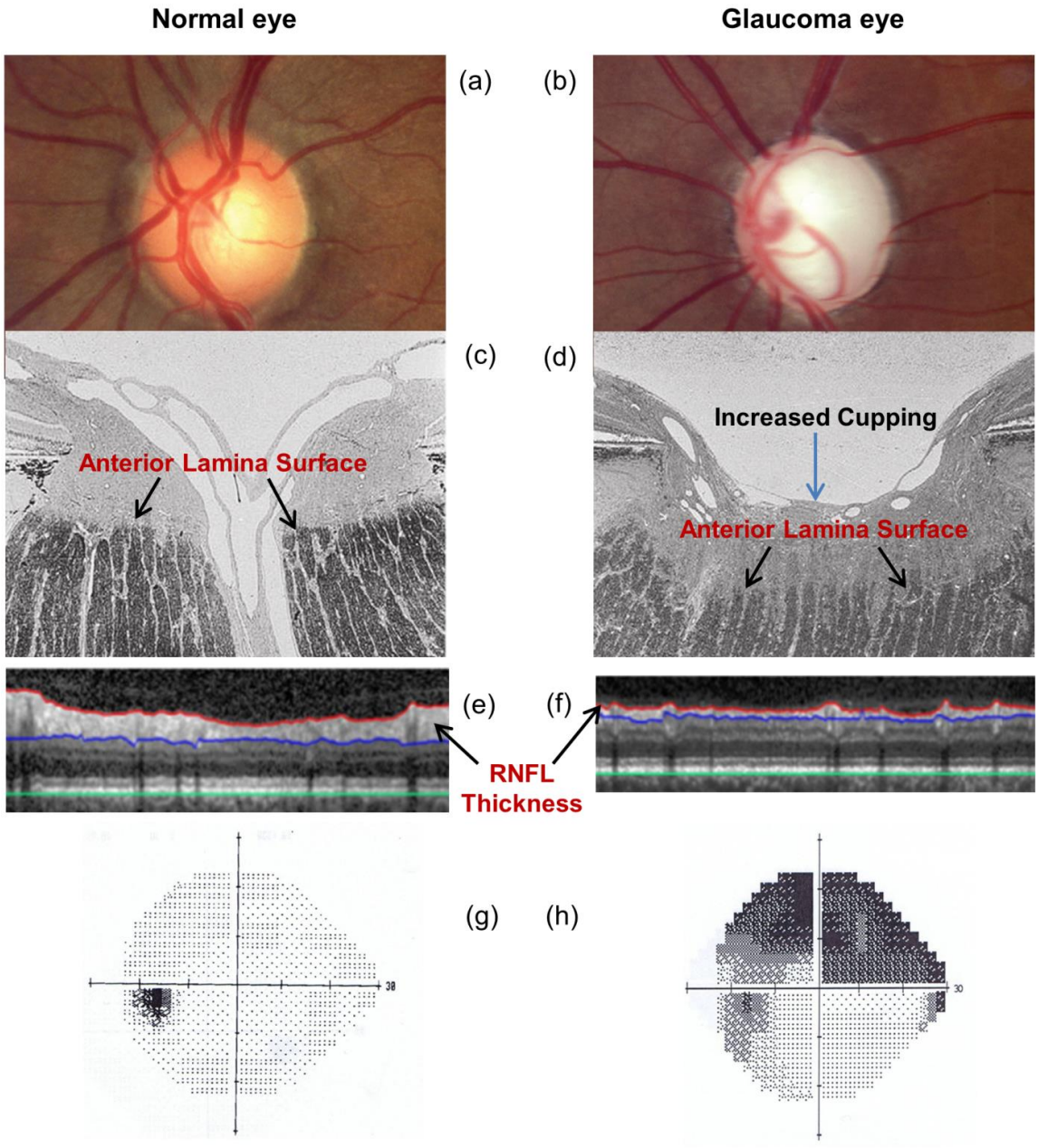

Figure 1-2. Typical changes that occur clinically in eyes with glaucoma (right column) compared to normal eyes (left column). (a,b) *En face* image of the ONH in which the white (or yellow) area represents the cup and the surrounding orange region represents the rim, or neuroretinal tissue. In glaucoma eyes the neuroretinal (rim) tissue is typically reduced, yielding a higher percentage of the disk that is occupied by the cup (larger white region) and a higher cup-to-disk ratio. (c,d) Cross sectional *ex vivo* images of the ONH from human eyes (different than those in [a,b]). Glaucomatous eyes have increased ONH cupped due to axonal loss and subsequent thinning of the neuroretinal

rim, as well as posterior bowing of the lamina cribroa. (a,b,c and d) Reprinted with permission (Quigley, 2011). (e,f) Optical Coherence Tomography (OCT) cross sectional images of the peripapillary retina surrounding the ONH in which the retinal nerve fiber layer (RNFL) is segmented as the layer between the red and blue boundaries. Glaucomatous eyes have a reduced thickness of the RNFL (i.e., thinner RNFL) due to the loss of axons. (e and f) Reprinted with permission (Mayer et al., 2010). (g,h) Humphery visual field report in (g) normal and (b) glaucomatous eyes indicating that glaucomatous eyes typically have increased visual filed loss (denoted by black shaded regions) compared to normal eyes.

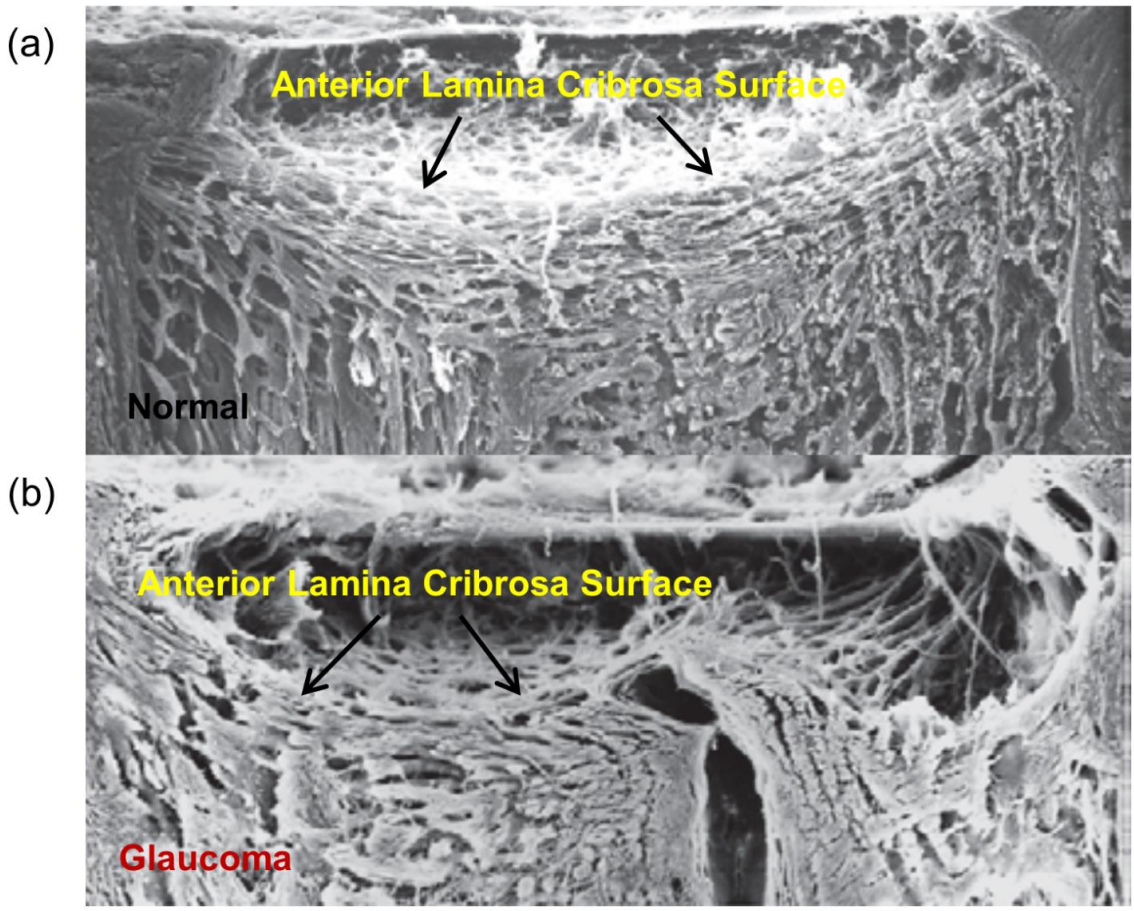

Figure 1-3. Electron microscope cross-sectional images of the human lamina cribrosa from (a) a normal eye and (b) a glaucomatous eye. The anterior lamina cribrosa surface (ALCS) tends to bow backward and become more curved as the ONH becomes more excavated in glaucoma. Reprinted with permission (Quigley, 2011).

1.3 Anatomy of the normal human ONH and lamina cribrosa

In normal human eyes, approximately one million RGC axons transmit visual signals from the eye to the brain (Sanchez et al., 1986; Mikelberg et al., 1989; Jonas et al., 1992). RGC axons travel from all parts of the retina and dive sharply over the neuroretinal rim as they make their way through the ONH and lamina cribrosa to the lateral geniculate nucleus (LGN). Many studies have examined the size of the physiologically normal ONH. Quigley et al. calculated mean vertical and horizontal optic disc diameters (from Bruch's Membrane) of 1.87 ± 0.17 mm and 1.76 ± 0.19 mm, respectively, in 60 adult human donor eyes, with a mean aspect ratio of 1.06 (i.e., nearly circular as the aspect ratio = 1 for a circle) and a mean disc area of 2.58 mm^2 (Quigley et al., 1990). However, these values can vary considerably across the population, particularly with race/ethnicity. For example, in the same study, Quigley et al. found that African-American eyes had larger vertical disk diameters (1.96 ± 0.16 mm) than compared to Whites (1.82 ± 0.15 mm).

The shape and diameter of the ONH can also vary with depth within the canal. In most normal eyes, the canal is conically-shaped with more posterior locations being larger in diameter than more anterior locations (Figure 1-4) (Hayreh, 2011). At the anterior portion of the ONH, the optic disc margin (a clinical construct used to determine cup-to-disc ratio) has been identified as coinciding with Bruch's Membrane Opening (BMO) and/or the border tissue of Elschnig (Reis et al., 2012). Jiang et al. examined the diameter of the normal BMO in 112 eyes (from 65 subjects) using spectral domain optical coherence tomography and measured a mean value of 1,524 ± 142 µm (Jiang et al., 2015). Just slightly deeper in the canal, histomorphometric reconstructions of the ONH in 10 human donor eyes revealed a slightly larger mean diameter for the scleral canal opening of 1,818 µm (range = 1,346 µm to 1,949 µm) with nearly circular openings (mean aspect ratio = 0.99) (Sigal et al., 2010).

The ONH is primarily composed of the central retinal artery and vein, retinal nerve fiber layer, and the prelaminar, laminar, and retrolaminar regions (Figure 1-4). The prelaminar region consists of glial "columns," or collections of glial tissue that surround axon bundles in a columnar fashion before entering the lamina cribrosa. This bed of glial tissue is attached centrally to the connective tissue of the central retinal vessels and peripherally attaches to the choroid (Hayreh and Vrabec, 1966). Axons next pass through the lamina cribrosa, a three dimensional meshwork of densely packed connective tissue beams that bridges the scleral canal and is predominantly composed of collagen and elastin (Figure 1-5) (Hernandez et al., 1989; Morrison et al., 1989; Hernandez et al., 1990). Centrally, the lamina binds to the connective tissue surrounding the central retinal artery and peripherally anchors to the surrounding sclera. RGC axons then enter the retrolaminar region where they become and remain myelinated throughout the ONH (Hayreh, 2011).

The lamina cribrosa provides structural and functional support to the RGC axons that course through it. The lamina's largely collagenous beams are surrounded by astrocytes and contain capillaries that are supplied by the short posterior ciliary arteries (Figure 1-6). Oxygen, nutrients and neurotrophic factors are supplied to the RGC axons from these capillaries and from the extracellular matrix and surrounding astrocytes (Anderson, 1969).

The vast majority of studies that have examined structural properties of the human lamina cribrosa have been performed *ex vivo* in donor eyes. The anterior lamina cribrosa surface is centrally elevated in normal eyes, with a ridge running in the nasal-temporal axis, and is depressed in the mid-periphery in the superior and inferior meridians (Quigley and Addicks, 1981; Park et al., 2012b). In separate studies, Jonas et al. and Kotecha et al. found the central lamina cribrosa to be approximately 450 µm thick. Jonas et al. measured a mean central lamina cribrosa thickness of 457.7 ±

163.7 µm (range: 92 – 1,008 µm) in 42 normal, donor eyes, while Kotecha et al. measured a mean central lamina thickness of 451.3 ± 56.5 µm (range: 345 – 556 µm) in 27 normal, donor eyes (Jonas et al., 2003; Kotecha et al., 2006).

Studies of laminar microarchitecture performed using transmission and scanning electron microscopy have found approximately 200 to 400 pores on the anterior laminar surface. The diameter of each pore changes continuously throughout the extent of the lamina and was reported to range from as small as 10 µm to greater than 100 µm (Quigley and Addicks, 1981). Increasing efforts have been placed into imaging the human lamina cribrosa microarchitecture *in vivo* (Bhandari et al., 1997; Ivers et al., 2011; Wang et al., 2013). Typically, it is not possible to image the entire anterior lamina cribrosa surface (ALCS) due to fact that the neuroretinal rim and overlying vessels can cast shadows onto the ALCS, making it challenging to visualize all of the ALCS microarchitecture. Sigal et al. recently estimated that 69% (range 58%-83%) of the anterior lamina cribrosa surface is visible through the scleral canal opening, on average, with the residual 31% of anterior lamina cribrosa surface extending beyond the canal opening (Sigal et al., 2010). Despite these challenges, a small number of published studies have quantified lamina cribrosa pore geometry in living normal and glaucomatous human eyes using adaptive optics and swept-source optical coherence tomography (SSOCT) (Ivers et al., 2011; Akagi et al., 2012; Wang et al., 2013; Zwillinger et al., 2016). For example, Wang et al. measured mean pore area and diameter to be 1970 ± 310 μm^2 and 24.6 ± 2.56 µm, respectively, throughout the entire extent of the lamina cribrosa using SSOCT in 19 healthy, normal eyes (Wang et al., 2013). Using an adaptive optics scanning laser ophthalmoscope, Akagi et al. calculated the mean area of ALCS pores to be 2,508 ± 826 μm^2 in 20 normal eyes and 3,013 ± 857 μm^2 in 20 glaucomatous eyes (Akagi et al., 2012; Wang et al., 2013; Zwillinger et al., 2016). While multiple studies have separately examined ONH and laminar microarchitecture in living

eyes, knowledge of any possible relationships between the laminar microarchitecture and its surrounding ONH structure have remained elusive in normal and glaucomatous eyes.

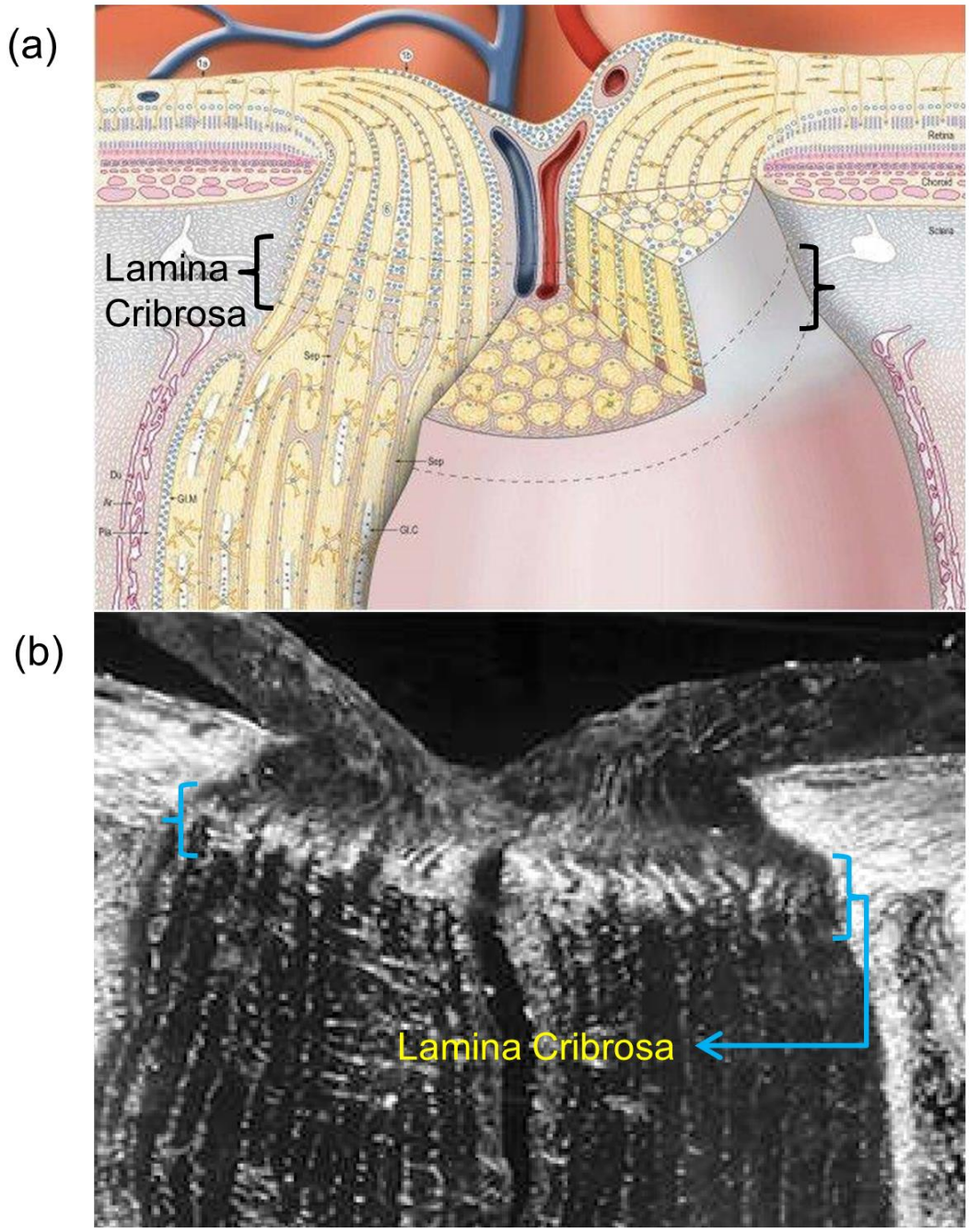

Figure 1-4. (a) A schematic illustrating the optic nerve head. Dashed lines represent the anterior and posterior borders of the lamina cribrosa. Bundles of RNFL axons (yellow) converge at and dive into the ONH. Axons first traverse through glial “columns” (network of blue circles) in the prelaminar region (region above the anterior laminar surface, or top dashed line). At the level of lamina cribrosa, axons bundles weave their way through pores created by laminar beams (pink) before exiting the lamina and emerging into the retrolaminar space (region below the posterior laminar surface, or bottom dashed line).

Reprinted with permission (Downs et al., 2008). Histological cross-section of the normal human ONH acquired using light microscopy. The hyper-reflective horizontal band represents the lamina cribrosa and the dark columns represent axon bundles. Reprinted with permission (Sigal et al., 2012).

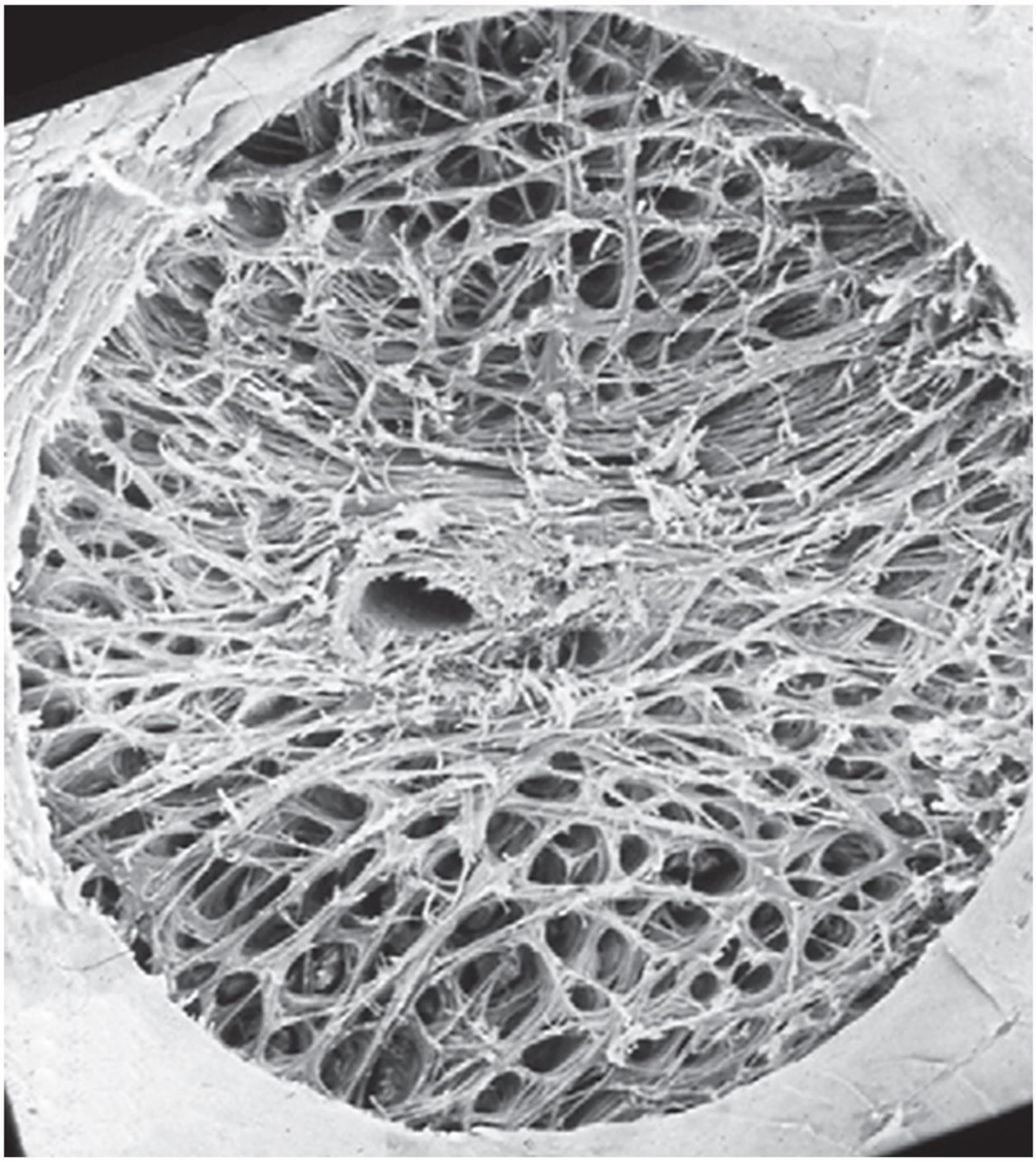

Figure 1-5. Representative *en face* image of normal laminar crobrosa beam and pore structure acquired using scanning electron microscopy. Collagenous beams forms a highly complex network through which the RGC axon bundles pass. Reprinted with permission (Quigley, 2011).

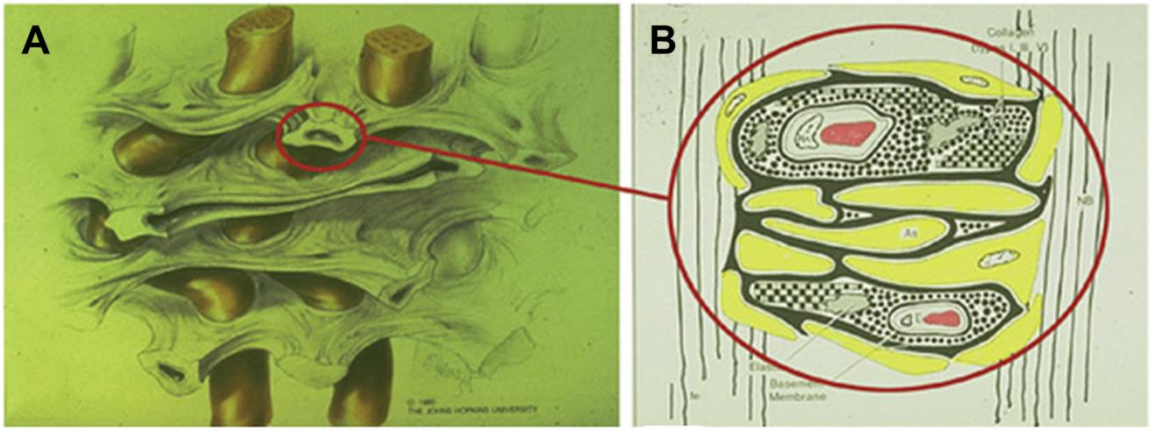

Figure 1-6. (Left) Cartoon illustrating axon bundles (red) weaving through lamina cribrosa pores. (Right) Magnified cross-sectional sketch of a single lamina cribrosa beam. Capillaries (red) course through laminar beams while astrocytes (yellow masses) surround the beams. Reprinted with permission (Morrison et al., 1989).

1.4 Risk factors for developing glaucoma

Multiple studies, such as the multicenter Ocular Hypertensive Treatment Study (OHTS), have determined several factors that increase an individual's risk for the development and progression of POAG, including older age, race (e.g., African American), sex (e.g., male), large vertical and horizontal cup-to-disc ratio, higher IOP, greater Humphrey visual field pattern standard deviations, heart disease and thinner central corneal thicknesses (CCTs) (Gordon et al., 2002). Part of the work described in this dissertation focuses on 2 potential risk factors, namely high myopia and older age.

1.4.1 High Myopia

There is no universal consensus on whether high levels of myopia inherently predispose the eye to the onset of glaucomatous neuropathy. The OHTS study (conducted in a predominantly white, non-Hispanic population) found no significant relationship between an individual's myopic error and the likelihood to develop glaucoma (Gordon et al., 2002). Conversely, the Barbados and Beijing Eye Studies found myopic refractive error to be a risk factor for open angle glaucoma (Leske et al., 1995; (Xu et al., 2007) while the Blue Mountain Eye Study found that glaucoma occurred with 2-3x higher frequency in myopic compared to non-myopic participants (Mitchell et al, 1999). In addition, the Beaver Dam Eye Study (Wong et al., 2003) found that myopic individuals were 60% more likely to have glaucoma compared to those who were not myopic. These reports raise the possibility that high myopia is associated with an individual's likelihood for developing the disease. Therefore, it is important to understand ONH structure in normal and glaucomatous eyes with different refractive states (or axial lengths).

A number of studies have examined retinal and ONH structure with axial length and refractive error in normal and glaucomatous eyes. The ONH in highly myopic, normal eyes (> -8.00 D) is distinctly different from normal eyes of low myopes,

emmetropes and hyperopes (Jonas et al., 1988). Multiple studies have shown that optic disc size (disc area) increases with increasing axial length and refractive error in normal, myopic eyes (Jonas et al., 1988; Oliveira et al., 2007). Lamina cribrosa thickness and RNFL thickness have also been shown to decrease with increasing axial length in myopic eyes (Ren et al., 2009; Lee et al., 2015; Malakar et al., 2015). In addition, ONH structure can vary dramatically with axial length within glaucomatous eyes, as well as between highly myopic glaucoma eyes and highly myopic normal eyes. POAG eyes that are highly myopic have more elongated secondary macrodiscs (defined as discs with an overall area greater than 2.82 mm^2), shallower and more concentric disc cupping, larger peripapillary atrophy, and a lower frequency of localized RNFL defects compared to POAG eyes with low to moderate myopia and/or hyperopia (Jonas and Dichtl, 1997). Despite these results from more traditional clinical measures, there is a lack of information detailing relationships between more recently defined ONH structural parameters (based on spectral domain optical coherence tomography imaging) and ocular biometry. In order to better understand these measured ONH parameters in glaucomatous eyes (including newly developed parameters that may earlier predict the onset of disease, such as mean ALCS depth and mean minimum rim width), it is important to know their variability in normal eyes, as well as their relationships with each other and with possible risks factors for disease (such as axial length). Chapter 2 of this dissertation will focus on this topic.

1.4.2 Age

Several studies have reported age as a major risk factor for the onset and progression of glaucoma. A meta-analysis performed on data from many prevalence studies found that the odds ratio of developing POAG is 1.73 for each decade of increasing age. This prevalence and odds ratio data, however, vary with geographic region and race (Figure

1-7) (Tham et al., 2014). Individuals from Africa have the highest prevalence of developing POAG through the 6th decade of life (Figure 1-7a). After the age of 60 years, there are dramatic increases in the prevalence rates for individuals from Latin America and the Caribbean, Oceania and North America to manifest overall prevalence levels that equal or exceed those seen in individuals in Africa by 80 years of age. Across race (Figure 1-7b), people of African ancestry have the highest prevalence of POAG for any decade of life. However, Hispanics have a steep increase in the prevalence of POAG after the 6th decade of life (Friedman et al., 2004; Tham et al., 2014).

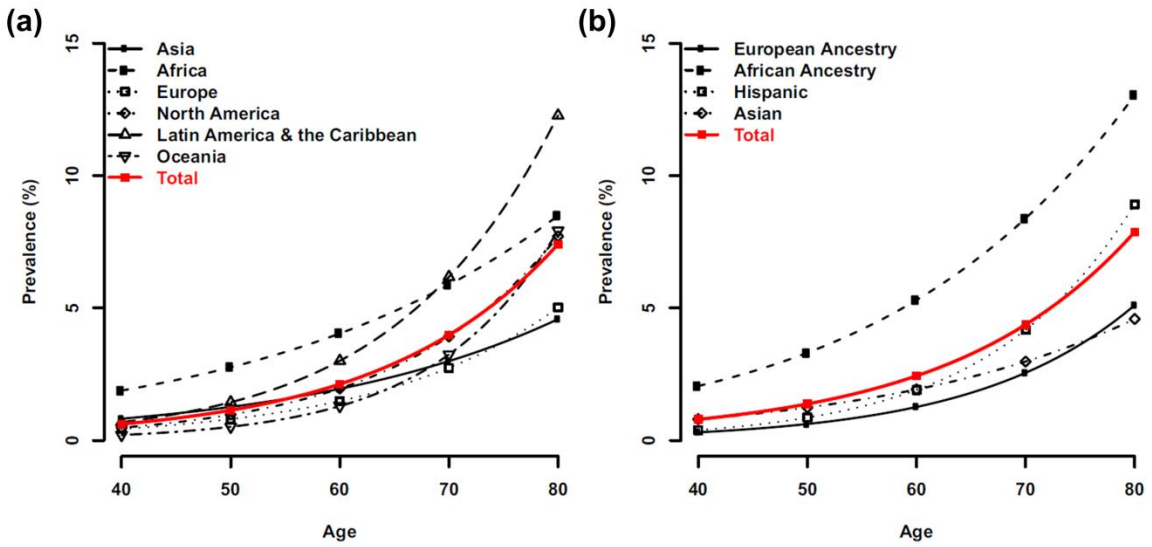

Figure 1-7. Prevalence of primary open angle glaucoma (POAG) worldwide broken down according to (a) geographical region and (b) race. Overall prevalence data were based on a meta-analysis of major population-based studies of glaucoma prevalence. Reprinter with permission (Tham et al., 2014).

Results from multiple reports suggest that age-related changes in the lamina cribrosa mimic changes also seen during glaucoma but to a lesser extent. For example, increases in lamina cribrosa thickness have been measured during very early stages of experimental glaucoma in non-human primates (Roberts et al., 2009a) and during normal aging in human eyes (at a rate of ~14 µm / decade; Figure 1-8) (Kotecha et al., 2006). In addition, increases in advanced glycation end products (AGEs) have been reported in the normal, aging lamina (Albon et al., 1995) and in higher concentrations in the glaucomatous lamina compared to normal, aged-matched eyes (Tezel et al., 2007). During the normal aging process, sugar crosslinks with a protein or lipid in a nonenzymatic reaction to produce AGEs that accumulate in every type of cell and tissue in the body, including the ONH and retina (Albon et al., 1995). AGEs are considered to exacerbate the degenerative disease process by interfering with the normal function of the tissue, as well as with protein and axonal transport (Cullum et al., 1991). Methylglyoxal, a precursor of AGEs, has also been associated with increased stiffness in the human lamina cribrosa and peripapillary sclera during the normal aging process (Spoerl et al., 2005; Tezel et al., 2007). When combined with the results from immunohistochemical studies that have reported increases in elastin and the total amount of collagen within the lamina with increasing age (Hernandez et al., 1989; Albon et al., 1995), these observations could result in a nonmalleable, stiffer lamina which may potentially increase the eye's susceptibility to glaucomatous damage. Changes in the constituents of the structural matrix of the lamina cribrosa during normal aging may alter its ability to provide structural and functional support to the RGC axon bundles passing through it and result in an increased susceptibility of the axons to damage.

.

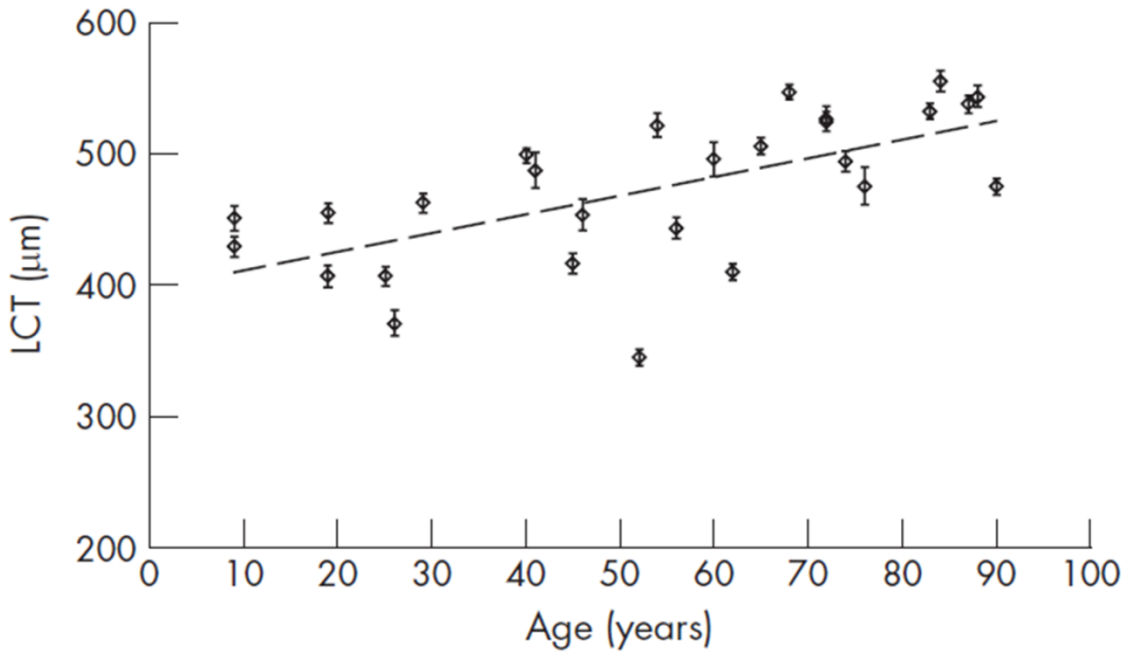

Figure 1-8. Differences in total lamina cribrosa thickness (LCT) with increasing age from 27 donor eyes (range = 9-90 years) were measured under hydrated conditions using light microscopy. Lamina cribrosa thickness increased with increasing age. Reprinted with permission (Kotecha et al., 2006).

With the aforementioned similarities between laminar changes seen during the physiologically normal aging process and glaucomatous progression, we could hypothesize a continuum of changes in laminar structure and composition that begins with the young, healthy normal eye, then progresses to a slightly altered state in older normal eyes, and continues to evolve to a more altered state in suspect/early glaucoma eyes, ending with dramatic structural changes in severe glaucoma (Figure 1-9). With this model in mind, glaucoma could potentially be characterized as an accelerated aging process (Tezel et al., 2007). Chapter 3 will examine whether structural differences in the ONH and lamina cribrosa microarchitecture exist between normal young and older eyes, while Chapter 4 will examine ONH and laminar microarchitecture between normal older eyes and glaucoma suspect/eyes with early-moderate POAG.

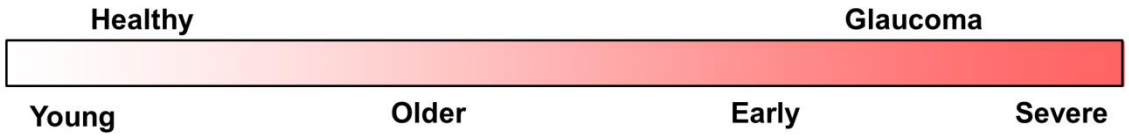

Figure 1-9. A potential continuum of change in ONH and lamina cribrosa microarchitecture could occur as the young, normal eye naturally ages and becomes an older, normal eye. These changes could continue in an accelerated fashion as the older, normal eye becomes a glaucoma suspect and slowly progresses to becoming an eye with early glaucoma, and finally to an eye with a severe stage of glaucoma.

1.5 Simultaneous examination of lamina cribrosa microarchitecture and ONH geometry

RGC axons are thought to be initially damaged at the level of the lamina cribrosa (Quigley and Anderson, 1976a). Under this hypothesis, the health of RGC axons will be dependent on the environment provided by lamina cribrosa within the ONH. Therefore, it is highly important to study RGC axonal integrity, lamina cribrosa morphology and the environment of the ONH hand-in-hand in normal and glaucomatous eyes. To our knowledge, there is a lack of studies that have examined both the neuronal and non neuronal structural elements of the ONH *in vivo* in human eyes. The last half of this dissertation comprehensively examines relationships between the ONH and anterior lamina cribrosa surface microarchitecture in human eyes in light of aging and early glaucoma.

1.6 Specific Aims

1.6.1 Characterize ONH and lamina cribrosa geometry and their relationship with axial length in young, normal eyes

The ONH and lamina cribrosa structurally change during glaucoma. Given the emergence of newly developed ONH parameters as possible predictors of disease (e.g., mean ALCS Depth, mean Minimum Rim Width), it is important to understand their variability in normal eyes, as well as their relationships with each other and with risk factors for disease (such as axial length). We quantified retinal, ONH and lamina cribrosa parameters in a population of normal, young eyes and examined their degree of correlation with axial length. We also investigated the relationships and interactions between ONH and lamina cribrosa parameters across subjects. This study provides increased knowledge on the degree to which spectral domain optical coherence

tomography (SDOCT) derived ONH parameters depend on axial length, as well as a normative database that can be compared with future measurements of these parameters in cross sectional studies of older normal and glaucomatous eyes.

1.6.2 Determine the variability in lamina cribrosa microarchitecture and ONH geometry between fellow eyes of normal subjects and as a function of aging

Age is a risk factor for glaucoma. Several studies suggest that normal aging could increase the susceptibility of the ONH to glaucomatous damage. To ensure that any potential structural differences measured in normal eyes as a function of age are due to natural aging itself and not to the normal variability inherent in these examined parameters between fellow eyes, we first assessed differences in ALCS pore and ONH geometry between fellow eyes of 32 normal subjects *in vivo* using AOSLO and SDOCT imaging, respectively. We then determined whether differences existed in ALCS microarchitecture and ONH structure between young and older normal human eyes. This study provides improved understanding of the intra- and intersubject variabilities of ALCS and ONH morphology present within a normal population and the impact of aging on these structures.

1.6.3 Determine whether differences exist in vivo in lamina cribrosa microarchitecture and ONH geometry between normal and glaucomatous eyes

Previous studies in living normal and glaucomatous human eyes have separately examined lamina cribrosa microarchitecture or ONH geometry. However, to better understand the disease process, it is necessary to examine changes in and relationships between neural, non-neural and supporting structures within the ONH during glaucoma. We measured and compared ONH geometry and ALCS microarchitecture between glaucoma suspects, patients with POAG and age-matched normal subjects. This study

provides increased knowledge of the relationships between ONH structure and ALCS microarchitecture within the eyes of early glaucoma patients and suspects, and their differences when compared to older, normal eyes.

CHAPTER 2

Optic nerve head and lamina cribrosa geometry in normal young eyes and their relationship with axial length

Contributing authors:

Sara Nourani, BS; B. Optom; Nimesh B. Patel, OD, PhD; Jason Porter, PhD

Abstract

Purpose: The optic nerve head (ONH) and lamina cribrosa structurally change during glaucoma. It is important to know the variability of ONH and lamina cribrosa geometry in normal eyes. We sought to understand relationships between ONH geometry, anterior lamina cribrosa surface (ALCS) position and axial length in young, normal eyes.

Methods: Spectral domain optical coherence tomography (SDOCT) radial B-scans centered on the ONH were acquired in one eye of 97 normal subjects (mean age = 26.4 ± 3.9 years). ONH features (Inner Limiting Membrane, Bruch's Membrane termination, ALCS) were semi-automatically marked on SDOCT B-scans using a custom program to calculate Bruch's Membrane Opening (BMO) area, mean ALCS depth (ALCSD) and mean minimum rim width (MRW). Scaled MRW (sMRW) was calculated for each eye by multiplying an eye's mean MRW by the ratio of its BMO circumference to the mean BMO circumference of the population. Ocular biometry (including axial length) was measured and used to laterally scale SDOCT images.

Results: While eyes with longer axial lengths had larger BMO areas (R^2=0.19, *P*<.01), no significant relationships were found between axial length and mean MRW (*P*=.40) or mean ALCSD (*P*=.07). Mean MRW was significantly thinner in eyes with more posteriorly located ALCS's (R^2=0.16, *P*<.01) and larger BMO areas (R^2=0.18, *P*<.01). However, there was no relationship between sMRW and BMO area (*P*=.20).

Conclusions: The larger BMO areas found in longer eyes may be explained by a model in which the retina and sclera stretch as the eye elongates during development. The decreased magnitude of mean MRW in eyes with increased ALCSD's potentially indicates that axons are pulled toward the BMO in eyes with a deeper lamina. The lack of relationship between sMRW and BMO area could imply that the total number of axons in normal young eyes is constant regardless of BMO size (or axial length).

2.1 Introduction

Glaucoma is a group of optic neuropathies that results in the damage of retinal ganglion cell axons and the death of retinal ganglion cells (Quigley et al., 1981). The condition is typically characterized clinically by an increase in optic nerve head (ONH) cupping, thinning and/or notching of the neuroretinal rim and loss of visual field (Quigley, 1996). Multiple risk factors exist for the development and progression of primary open angle glaucoma, including increased age (Gordon et al., 2002; Leske et al., 2003) and, potentially, high levels of axial myopia (Perkins and Phelps, 1982; Mitchell et al., 1999; Xu et al., 2007; Quigley, 2011).

Several structural changes have been shown to occur in the retina, ONH and lamina cribrosa during early stages and the progression of glaucoma. Retinal nerve fiber layer thickness (RNFLT) in the circumpapillary region has become a primary, objective clinical measurement used in the diagnosis of glaucoma. However, recent *in vivo* work in a non-human primate experimental model of glaucoma has shown that changes in the position of the anterior surface of the lamina cribrosa (or anterior lamina cribrosa surface depth, ALCSD) and in minimum rim width (MRW) can precede the earliest changes measured in RNFLT and potentially be earlier structural biomarkers of disease onset (Strouthidis et al., 2011; He et al., 2014b; Patel et al., 2014b; Ivers et al., 2015). Given the emergence of these (and other) parameters as possible predictors of disease, it is important to understand their variability in normal eyes, as well as their relationships with each other and with known risk factors for disease (such as axial length).

A number of studies have examined retinal and ONH structure with axial length and refractive error in both young and older normal eyes. Multiple studies have shown that optic disc size (disc area) increases with increasing axial length and refractive error in normal, myopic eyes (Jonas et al., 1988; Oliveira et al., 2007). Moreover, lamina cribrosa thickness has been shown to decrease with increasing axial length (Ren et al.,

2009). Retinal nerve fiber layer (RNFL) thickness was also found to decrease with increasing axial length and myopia (Lee et al., 2015; Malakar et al., 2015). However, there is a lack of detailed information that describes the inter-relationships between retinal, ONH and biometric parameters within young normal eyes, particularly for more recently developed ONH and lamina cribrosa parameters (e.g., MRW, ALCSD).

The purpose of this study was to better understand relationships in normal ONH and lamina cribrosa geometry, as well as their variation in eyes of different length. We quantified retinal, ONH and lamina cribrosa parameters in a population of normal, young eyes and examined their degree of correlation with axial length. Furthermore, we investigated the relationships and interactions between ONH and lamina cribrosa parameters across subjects. This study provides increased knowledge on the degree to which spectral domain optical coherence tomography (SDOCT) derived ONH parameters depend on axial length in normal, young human eyes.

2.2 Methods

All human subjects research adhered to the tenets of the Declaration of Helsinki and was approved by the University of Houston's Committee for the Protection of Human Subjects. Informed consent was obtained from all subjects prior to examination. Ninety-seven normal subjects (38 men, 59 women) over 18 years of age (mean age = 26.4 ± 3.9 years; range = 21 – 41 years) were recruited from the University of Houston College of Optometry and the University Eye Institute. 48 of the subjects were Caucasian, 43 were Asian, 3 were African-American and 3 were Hispanic. All subjects had best-corrected visual acuities of at least 20/20 with no visual field defects (24-2 SITA standard visual field) and no history of ocular surgery or pathology. Subjects with a history of hypertension and/or diabetes were included only if there was no associated retinal or

optic nerve pathology. One eye was selected from each subject for the study (45 right eyes, 52 left eyes) and dilated for imaging using tropicamide (0.5%).

2.2.1 Spectral domain optical coherence tomography (SDOCT) imaging and analysis

Cross-sectional images of the retina and ONH were acquired using spectral domain optical coherence tomography (SDOCT; Spectralis HRA-OCT, Heidelberg Engineering, Heidelberg, Germany). Retinal nerve fiber layer thickness was quantified from 12° circular scans (Automatic Real Time [ART] averaging of 40 frames) centered on the ONH. The Inner Limiting Membrane (ILM) was automatically segmented in each of 24 radial B-scans (20º field, ART averaging of 20 frames) centered over the ONH using the instrument's segmentation software and any inaccuracies were manually corrected. The termination points of the retinal pigment epithelium (RPE)/Bruch's membrane (BM) interface and anterior lamina cribrosa surface (ALCS) were manually marked in as many B-scans as possible using a custom Matlab algorithm (Figure 2-1).

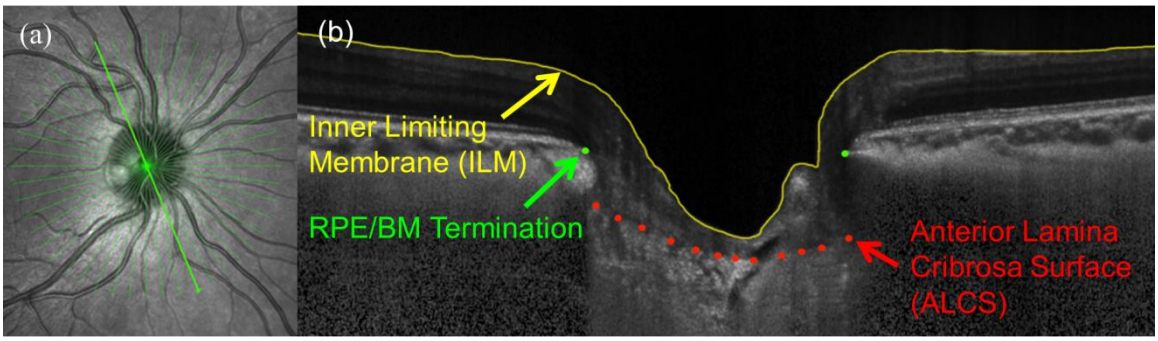

Figure 2-1. Semi-automated delineation of retinal and ONH features from SDOCT images. (a) Representative *en face* view of the ONH illustrating the locations of all 24 radial b-scans (green lines) acquired via SDOCT. (b) Single radial b-scan of the ONH corresponding to the scan location denoted by the bold green line in (a). Automatically segmented and manually marked features included the ILM (yellow line), termination points of the RPE/BM interface (green points) and the anterior lamina cribrosa surface (red points).

Two ONH parameters were calculated from the delineated landmarks. Bruch's Membrane Opening (BMO) area was calculated as the area enclosed by an ellipse best-fit to the marked RPE/BM termination points that denoted the BMO (Figure 2-2a). Mean anterior lamina cribrosa surface depth (ALCSD) was also computed as the mean distance between the BMO plane (a plane best-fit to the BMO ellipse in 3 dimensions) and a thin-plate spline surface that was fit to the marked ALCS points to model the ALCS in 3 dimensions (Figure 2-2b) (Sredar et al., 2013).

Two inner retinal parameters were also calculated from the delineated features. Mean minimum rim width (MRW) was calculated as the mean value of the minimum (perpendicular) distances between each RPE/BM termination point and the ILM across all marked B-scans (Figure 2-3). In addition, we also calculated a scaled version of MRW (sMRW) to account for the differences in disc size across subjects. Previous studies have shown that the ratio of ONH rim area (RA) to disc area decreases with increase in disc size and that RA does not vary with disc area (Girkin et al., 2004; Knight et al., 2012). Therefore, using the method previously described by Patel et al. (Patel et al., 2014a), we accounted for individual disc size in our mean MRW measurement by first calculating the circumference of the BMO ellipse for a given eye as

$$\text{BMO Circumference (μm)} = \pi\left[3(a+b) - \sqrt{10ab + 3(a^2+b^2)}\right] \quad (1)$$

where a and b are the semi-major and semi-minor axes of the BMO ellipse, respectively. Scaled MRW (sMRW) was then calculated for each eye by multiplying an eye's mean MRW by the ratio of its BMO circumference to the mean BMO circumference of a normal population (4,825 μm) (Patel et al., 2014a):

$$sMRW\ (\mu m) = MRW(\mu m) * \frac{BMO\ Circumference\ (individual\ eye)}{Mean\ BMO\ Circumference\ (population)}$$

$$= MRW(\mu m) * \frac{BMO\ Circumference\ (individual\ eye)}{4{,}825\ \mu m} \quad (2)$$

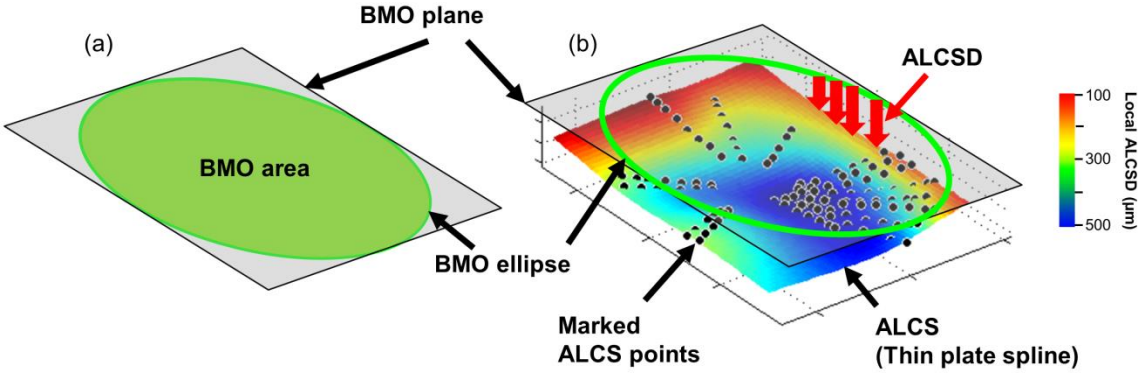

Figure 2-2. Method to calculate BMO area and mean ACLSD. (a) An ellipse (bold, green line) was best-fit in 3-dimensions to the marked RPE/BM termination points and used to define a BMO plane (gray). BMO area was calculated as the area enclosed by the BMO ellipse on the BMO plane. (b) After fitting a thin plate spline to the marked ALCS points (black dots, above and below the thin-plate spline), the mean anterior lamina cribrosa surface depth (ALCSD) was calculated as the mean of the perpendicular distances from the BMO plane to the thin plate spline (red arrows) for points within the BMO ellipse. The depth of the ALCS at each point on the thin-plate spline surface (local ALCSD) is color coded using the scale on the right side of the image. Regions shaded in blue represent locations with increased mean ALCSD values (i.e., more posteriorly located ALCS points within the ONH) while regions shaded in red represent locations with decreased mean ALCSD values (i.e., more anteriorly located ALCS points).

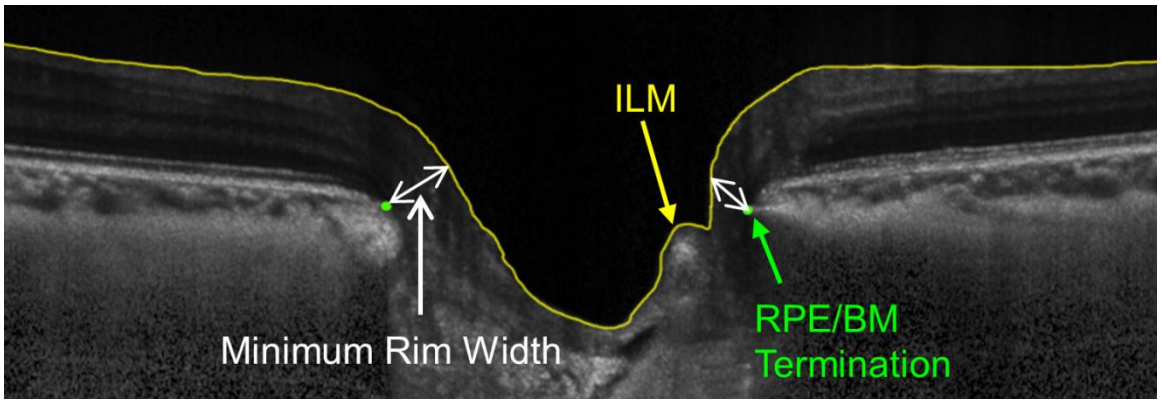

Figure 2-3. Method to calculate mean minimum rim width (MRW). Mean MRW was calculated by averaging the minimum distances measured between the delineated ILM surface (yellow line) and termination points of the RPE/BM interface (green dots) on each side of the neural canal opening (white arrows) across all marked B-scans.

2.2.2 Biometric measurements and image scaling

Measurements of axial length, anterior chamber depth and anterior corneal curvature were acquired using an optical biometer (LenStar LS 900; Haag-Streit, Koeniz, Germany). These biometric parameters were incorporated into a 4-surface model eye as previously described (Li and Roorda, 2007; Ivers et al., 2011) to laterally scale all SDOCT images by converting image dimensions from visual angle (in degrees) to physical retinal size (in micrometers). All image scaling was performed prior to calculating any retinal or ONH parameters.

2.2.3 Statistical Analyses

All statistical tests were performed using a commercially available platform (SigmaPlot; Systat Software Inc., San Jose, CA). Shapiro-Wilk normality tests were performed on all data, including subject age, axial length, BMO area, mean ALCSD, mean MRW and mean sMRW. *P* values < .05 represented distributions that were not normally distributed. Linear regression analyses were performed between axial length and all retinal and ONH parameters, as well as between all retinal and ONH parameters. Multivariate regression analyses were executed using mean ALCSD or mean MRW as the dependent variable and all other retinal/ONH parameters and axial length as independent variables. *P* < .05 represented statically significant correlations for the parameters analyzed.

2.3 Results

Mean values of axial length and all retinal and ONH parameters measured across all eyes are presented in Table 2-1. Based on the Shapiro-Wilk normality test, age and BMO area were the only non-normally distributed parameters.

Table 2-1: Mean measures of age, axial length, and ONH and retinal parameters across all normal young eyes.

	Mean ± Standard deviation	Range		Shapiro-Wilk normality test
		Minimum	Maximum	
Age (years)	26.4 ± 3.9	21.3	42.5	P < 0.01
Axial length (mm)	24.53 ± 1.22	22.02	27.72	*P* = 0.67
BMO area (mm^2)	1.866 ± 0.419	1.665	2.912	*P* < 0.01
Mean ALCSD (µm)	370.4 ± 86.7	209.8	595.4	*P* = 0.15
Mean RNFLT (µm)	101.1 ± 10.3	076	129	*P* = 0.74
Mean MRW (µm)	337.6 ± 64.6	152.7	476.4	*P* = 0.67
Mean sMRW (µm)	334.6 ± 59.9	185.1	476.2	*P* = 0.83

We examined the degree of relationship between all retinal/ONH measures and axial length across eyes (Figure 2-4). BMO area was significantly correlated with axial length (Figure 2-4a), as eyes with increased axial length tended to have larger BMO areas (R^2 = 0.19, *P*<.01). There were no statistically significant relationships between other retinal/ONH parameters and axial length, including mean ALCSD (*P*=.07), mean MRW (*P*=.40) and mean sMRW (*P*=.97). When performing a multivariate regression analysis with mean ALCSD as the dependent variable and axial length, BMO area and mean MRW as independent variables, axial length was still not a predictor for mean ALCSD (*P*=.16). In this multivariate model, only mean MRW was significantly correlated with mean ALCSD (*P*<.01). When performing a multivariate regression analysis with mean MRW as the dependent variable and axial length, BMO area and mean ALCSD as independent variables, axial length was not a predictor for mean MRW (*P* = .69). In this multivariate model, BMO area (*P* <.01) and mean ALCSD (*P* <.01) significantly correlated with mean MRW.

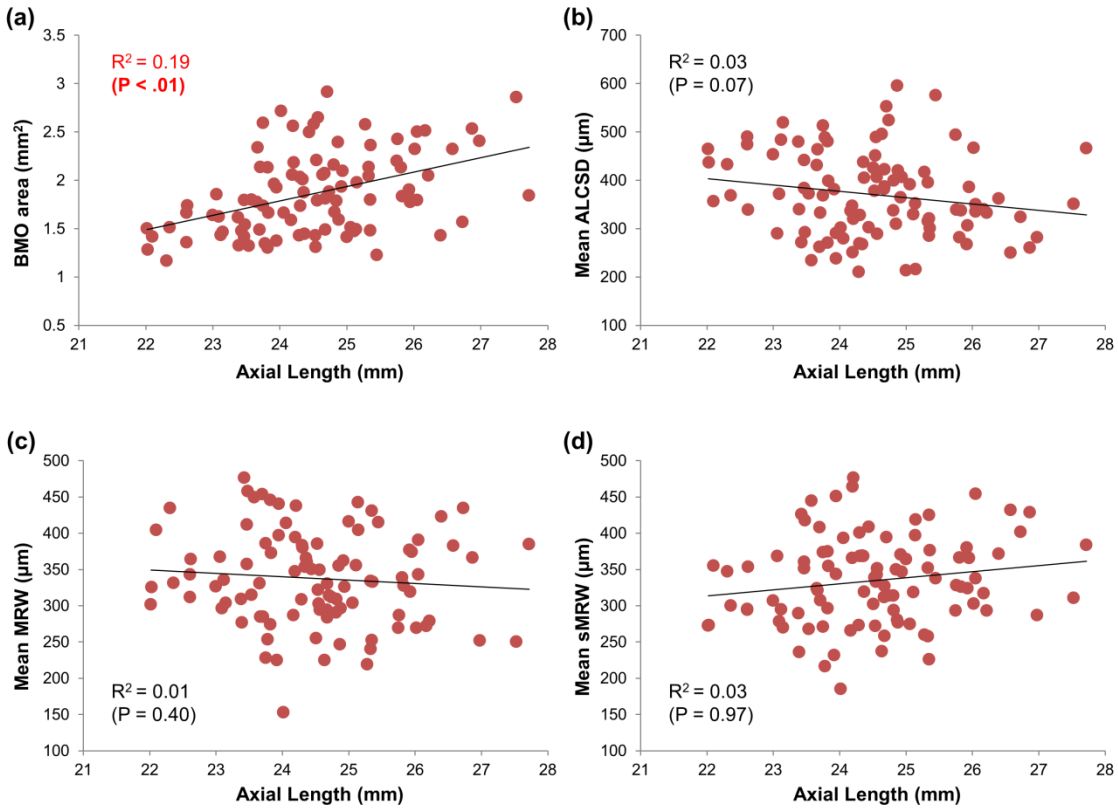

Figure 2-4. Retinal and ONH parameters plotted as a function of axial length across all eyes. Red filled circles represent individual eyes. Solid black lines indicate linear regressions fit to the data points. (a) BMO area significantly increased with increasing axial length (*P*<.01). No other retinal or ONH parameters measured in this study, including (b) mean ALCSD (*P*=.07), (c) mean MRW (*P*=.40) or (d) mean sMRW (*P*=.97), were significantly correlated with axial length.

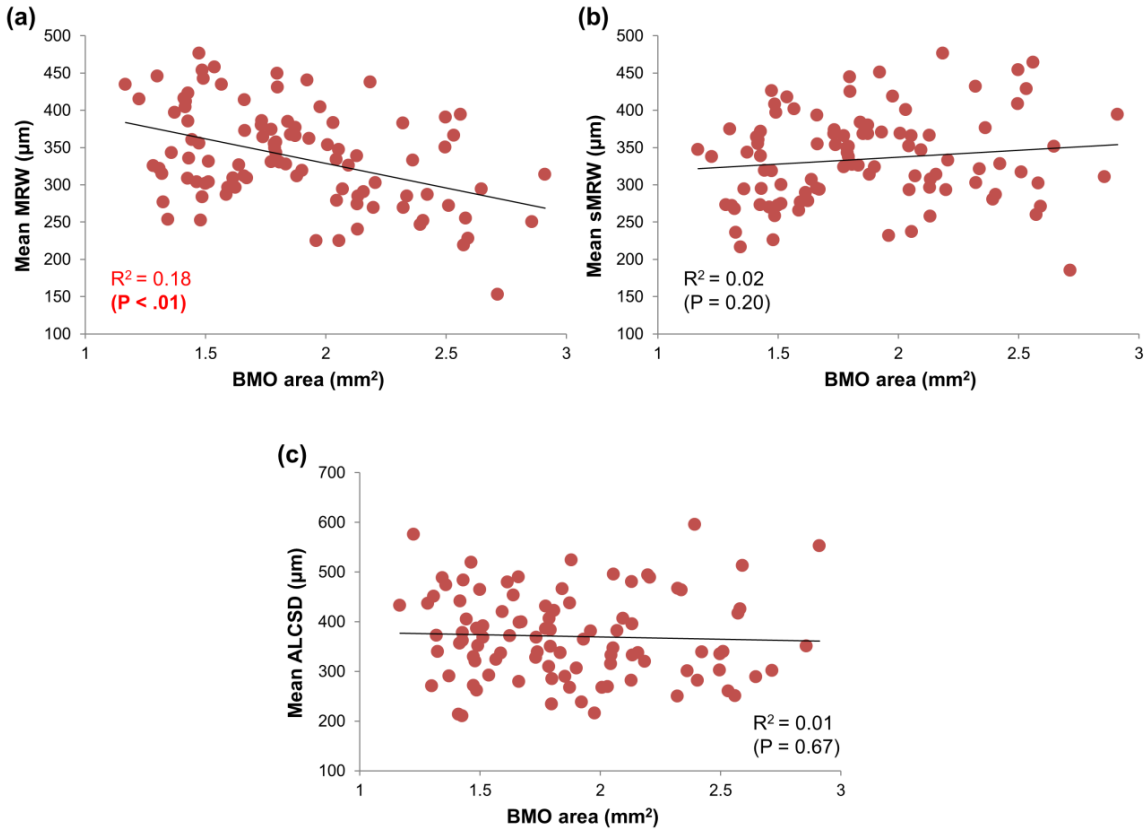

Figure 2-5. Mean MRW, mean sMRW and mean ALCSD plotted as a function of BMO area across all eyes. Red filled circles represent individual eyes. Solid black lines indicate linear regressions fit to the data points. (a) Mean MRW was significantly smaller in eyes with larger BMO areas (*P*<.01). (b) After scaling each eye's mean MRW by the ratio of its specific BMO circumference to an average BMO circumference from a normal population, there was no significant correlation between mean sMRW and BMO area (*P*=.20). (c) There was also no significant relationship between mean ALCSD and BMO area across eyes (*P*=.67), indicating that the depth of the anterior laminar surface was independent of the size of the BMO across eyes.

In addition to investigating relationships between retinal/ONH parameters and axial length, we also examined the degree of correlation between retinal and ONH measurements across eyes. Figure 2-5a illustrates that mean MRW significantly decreased with increasing BMO area across eyes ($R^2 = 0.18$, $P < 0.01$). However, after scaling each eye's mean MRW by the ratio of its own BMO circumference to an average BMO circumference across the population (Figure 2-5b), no statistically significant relationship was found between mean sMRW and BMO area across eyes ($R^2 = 0.02$, P=.20). In addition, no significant correlation was measured between mean ALCSD and BMO area across eyes (Figure 2-5c) ($R^2 = 0.01$, P=.67), indicating that the depth of the anterior laminar surface was independent of the size of the BMO across eyes. In other words, normal young eyes with larger BMOs did not necessarily have more posteriorly-located anterior laminar surfaces.

When examining relationships between retinal/ONH parameters and mean ALCSD, both mean MRW and scaled MRW were significantly correlated with mean ALCSD (Figure 2-6). Mean MRW significantly decreased in eyes with more posteriorly located anterior laminar surfaces ($R^2 = 0.16$, $P < .01$). A slightly stronger relationship was observed between the mean scaled values of MRW (sMRW) and mean ALCSD across eyes (Figure 2-6b; $R^2 = 0.23$, $P < .01$). However, mean MRW did not show any significant correlation with mean RNFL (Figure 2-6c; $R^2 = 0.03$, $P = .09$).

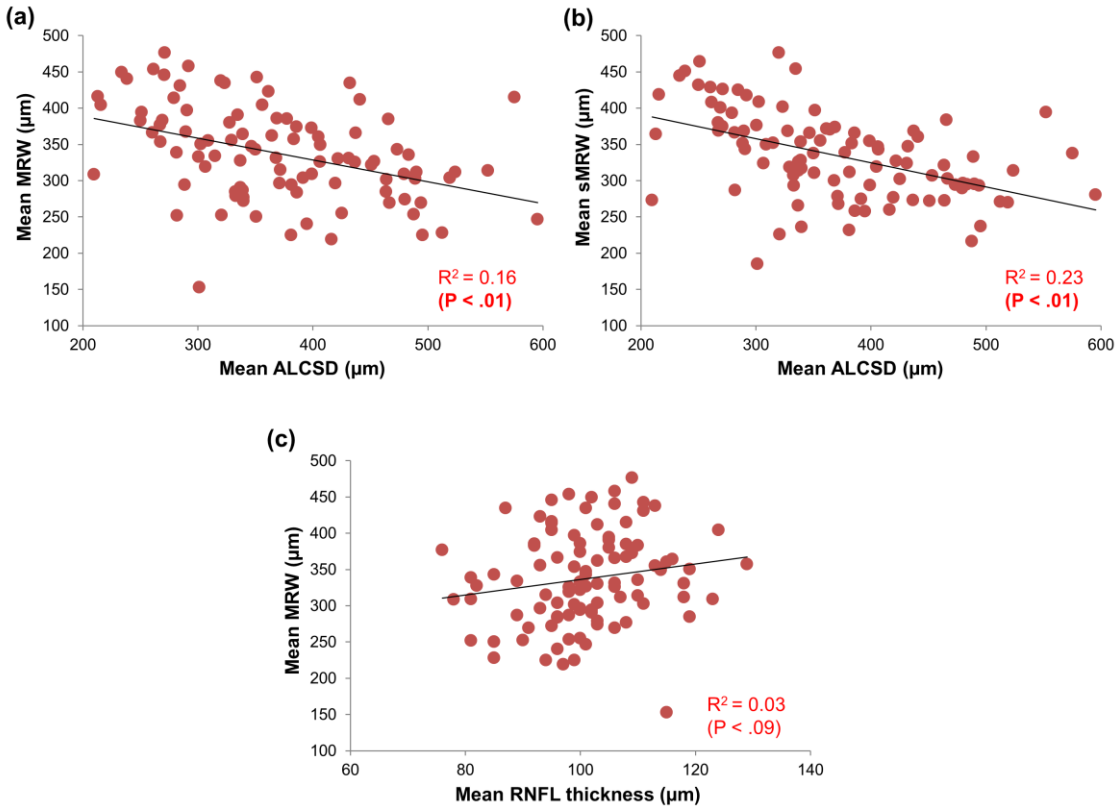

Figure 2-6. Mean MRW and mean sMRW plotted as a function of mean ALCSD across all eyes. Red filled circles represent individual eyes. Solid black lines indicate linear regressions fit to the data points. (a) Mean MRW and (b) mean sMRW significantly decreased ($P < .01$) with increasing mean ALCSD across eyes. (c) Mean MRW plotter as a function of mean RNFL thickness. Mean MRW do not show significant correlation with mean RNFL thickness.

2.4 Discussion

The purposes of this study were to better understand (1) relationships between retinal/ONH parameters and axial length and (2) the extent of relationships between retinal and ONH parameters in a population of young, normal eyes. *In vivo* SDOCT images of the ONH were acquired and scaled using each subject's ocular biometry data to obtain measures of retinal and ONH structure in each examined eye. Across young subjects, longer eyes had larger BMO areas. While eyes with larger BMO areas had decreased mean MRWs, no significant relationship existed between mean sMRW and BMO area or between mean ALCSD and BMO area. However, mean MRW and mean sMRW were both smaller (thinner) in eyes with large mean ALCSDs.

We intentionally studied retinal, ONH and axial length properties in a population of young, normal eyes (mean age = 26.4 ± 3.8 years) to minimize any potentially confounding effects due to normal aging. Age is a well-documented risk factor for the development and progression of glaucoma (Gordon et al., 2002; Leske et al., 2003) and age-related changes have been noted in the normal ONH and lamina cribrosa. For example, increases in total lamina cribrosa thickness and lamina cribrosa beam thickness have been reported in older, normal human eyes.(Kotecha et al., 2006) To minimize the potential impact of normal aging on these data, we restricted our subjects to those with young, healthy eyes.

In vivo measurements of ONH structure made in our population of eyes (Table 2-1) are similar to previously published data from normal eyes. The values of BMO area calculated across our subjects (mean = 1.866 ± 0.42? mm^2; range = 1.665 – 2.912 mm^2) substantially overlap with values reported by Chauhan et al. (median = 1.7 mm^2; interquartile range = 1.4 – 1.9 mm^2) (Chauhan et al., 2013) and by Thakku et al. (mean = 2.29 ± 0.42 mm^2; range = 1.29 – 3.72 mm^2) (Thakku et al., 2015). The average value of mean ALCSD measured across eyes in this study (370.4 ± 86.7 μm) is also similar to

measurements made previously in normal eyes (mean values of 387.7 µm and 403 µm) (Wu et al., 2015) (Thakku et al., 2015). However, the average value of mean MRW for our study population (337.6 ± 64.6 µm) is slightly larger than the mean MRW values reported in normal eyes by Chauhan et al. (median = 316 µm) (Chauhan et al., 2013) and Thakku et al. (280 ± 45 µm) (Thakku et al., 2015). Our slightly greater mean MRW value could be due to the fact that our study consisted of young subjects (mean age = 26.4 ± 3.8 years), while the two aforementioned studies consisted of older subjects (median age = 65 years; mean age = 58 ± 7 years) (Chauhan et al., 2013) (Thakku et al., 2015). Based on previously published data, it is known that axon counts tend to decrease with increasing age.(Harwerth and Wheat, 2008; Patel et al., 2014a) Given that mean MRW could be a surrogate metric for the number of retinal ganglion cell axons passing into the ONH, it is plausible that younger eyes could have slightly elevated values of mean MRW (i.e., larger numbers of axons) compared to older eyes (with fewer numbers of axons).

Reports from previous studies documenting differences in BMO area and mean ALCSD for eyes of different axial length potentially support a model in which the shape of the mature ONH is at least partially driven by retinal/scleral stretching during development. In such a model (Figure 2-7), one would expect retinal/scleral stretching in longer eyes to yield (1) larger (more stretched) BMO areas and (2) decreased mean ALCSDs (i.e., shallower anterior laminar surfaces) as the retina/sclera pull the ALCS to become increasingly taut. Similar to earlier studies (Seo et al., 2014) (Thakku et al., 2015), BMO area was significantly correlated with axial length in our subjects (i.e., eyes that were longer tended to have larger BMO areas). This finding supports a model in which the size of the ONH is driven by retinal/scleral stretching. However, while there was a trend for longer eyes to have decreased values of mean ALCSD in our study (i.e., anterior laminar surface positions that were closer to the BMO), the relationship was not

strong (R^2 = 0.03) or significant in univariate (*P*=.07) and multivariate (*P*=.14) regression analyses. Our finding is in agreement with Seo et al (Seo et al., 2014), who found a trend but no significant relationship between these parameters in univariate (*P*=.09) and multivariate analyses when analyzing only one eye from each subject. Conversely, our finding opposes the result by Thakku et al. (Thakku et al., 2015) who found decreased values of mean ALCSD in longer eyes (*P*=.003). Nevertheless, the finding that longer, young eyes tend to have shallower ALCS's and significantly larger BMO areas supports the idea the retinal/scleral stretching likely plays an important role in driving the development of the normal adult ONH. It is also worth noting that factors other than retinal/scleral stretching may contribute to the final shape of the mature ONH. For example, the proportion of the constituent components comprising the laminar beams (collagen types, elastin, fibriliin) may vary from eye to eye, resulting in different laminar stiffnesses and differing degrees to which the lamina can flexibly change its surface position in the ONH.

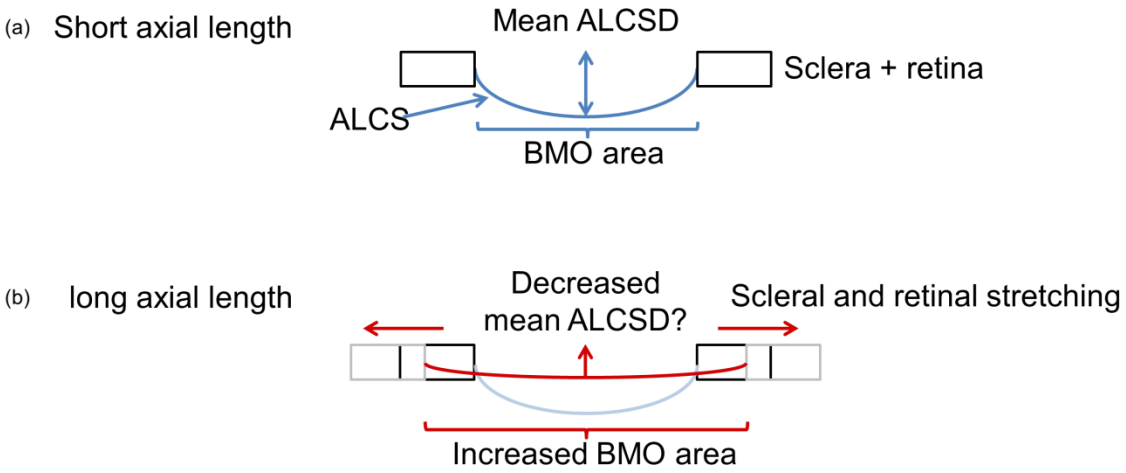

Figure 2-7. Schematic demonstrating the potential impact of scleral and retinal stretching on BMO area and mean ALCSD in an eye with a long axial length. The termination points of the BM/RPE complex, or BMO points, are denoted by black rectangles. BMO area is represented as the horizontal distance between BMO points (black rectangles) while mean ALCSD is the mean distance between the top of the BMO points (black rectangles) and the curved anterior lamina cribrosa surface (ALCS). (a) An eye with a short axial length, a certain BMO area and a certain mean ALCSD is illustrated. (b) If scleral and retinal stretching were the only factors to determine ONH shape, one might predict that a stretching force that pulls laterally on the ONH (red arrows) in an eye with a long axial length would increase the BMO area while decreasing the mean ALCSD as the ALCS is pulled more tautly toward the BMO plane (red curve) relative to the eye with a short axial length in (a) (drawn again in (b) with gray rectangles representing the initial BMO position and the light blue curve representing the initial position of the ALCS).

Mean MRW inversely correlated with BMO area in our subjects. In other words, eyes with larger BMO areas tended to have smaller (thinner) mean MRWs. Given that MRW is thought to be a surrogate metric for the number of axons entering the ONH, this finding might initially suggest that longer eyes with larger BMO areas would have less axons (smaller mean MRW) than shorter eyes with smaller BMO areas (larger mean MRW). Such an interpretation, though, would oppose findings in previous studies in humans and non-human primates that reported an increased number of axons in eyes with larger optic discs (Quigley et al., 1991; Jonas et al., 1992). However, when mean MRW is scaled for individual eyes (taking into consideration the size of each eye's BMO circumference), we found there was no correlation between mean sMRW and BMO area. These two findings - (1) a decrease in mean MRW with increasing BMO area, but (2) no correlation between mean sMRW and BMO area – could imply that the number of axons in normal eyes is relatively constant regardless of the size of the BMO. This notion is potentially a more viable interpretation of our data, as ganglion cells and their axons are formed early in development and much sooner compared to the time course in which the eye undergoes axial elongation to assume its mature, adult length and size. Retinal ganglion cells are the first cell to differentiate and are almost completely formed by birth (Marquardt and Gruss, 2002). However, the eye's axial length continues to increase well after birth, often through the late teenage years in most individuals (Joao et al., 1989). Histology based reports have demonstrated that total retinal ganglion cell counts vary across species within mammals (e.g., mice, rats, rabbits, non-human primates, humans) and, in general, larger eyes have greater numbers of RGC neurons.(Oyster et al., 1981; Perry and Cowey, 1985; Curcio and Allen, 1990; Danias et al., 2002; Salinas-Navarro et al., 2009) However, within a single species (such as non-human primates), retinal ganglion cell counts are fairly consistent (Table 2-2) (Perry and Cowey, 1985; Silveira et al., 1989; Fischer and Kirby, 1991; Herbin et al., 1997).

The idea that all normal, young human eyes could possess similar numbers of axons despite differences in the BMO areas is illustrated in Figure 2-8. In this figure, MRW appears as a “skirt” (shaded blue) that runs along the entire BMO circumference and is bounded on the top by the ILM (yellow line) and the bottom by the BMO ellipse (green line). Based on results from Figure 4-2a, eyes with larger BMO areas have smaller (thinner) mean MRWs (Figure 2-8, bottom row). This result, when coupled with our finding of no significant correlation between mean scaled MRW (sMRW) and BMO area, could imply that very similar numbers of axons exist within segments of the MRW with the same unfolded cross-sectional areas in eyes with different BMO sizes (Figure 2-8, right-most column). In such a scenario, axons would need to stack on top of each other in eyes with smaller BMO areas in order to enter the ONH (producing a larger mean MRW) while less stacking would be required in eyes with larger BMO areas. These results suggest that it is important to examine mean MRW in concert with BMO area when using mean MRW as a metric to assess axon health, as measuring a small value of mean MRW in an eye with a large BMO area (representing a potentially “normal” measeurement) may need to be interpreted differently than a comparably small measured value in an eye with a small BMO area (representing a potentially “abnormal” measurement).

Table 2-2: Total ganglion cell count in various species of mammals, documented in literature.

	Total Ganglion Cell count	Number of eyes	References
Mice	Swiss 49,493 ± 3936	34	Salinas-Navarro et al., 2009
	C57 42,658 ± 1540	26	
Rat	Wistar rats 97,609 ± 3,930	10	Danias et al., 2001
Rabbit	New Zealand red rabbit 406,375 ± 13,646	3	Oyster et al., 1981
Primate	Macaca mulatta 1,500,000	2	Perry et al., 1985
	Papio anubis 1,580,000 ± 169,927	6	Fischer et al., 1991
	Cercopithecus aethiops sabeus 1,228,646 ± 33,773	5	Herbin et al., 1997
	Cebus apella 1,400,000	2	Silveira et al., 1989
Human	1,070,000 ± 400,000	6	Curcio et al., 1990
	2,179,557 ± 508,090	12	Harman et al., 2000

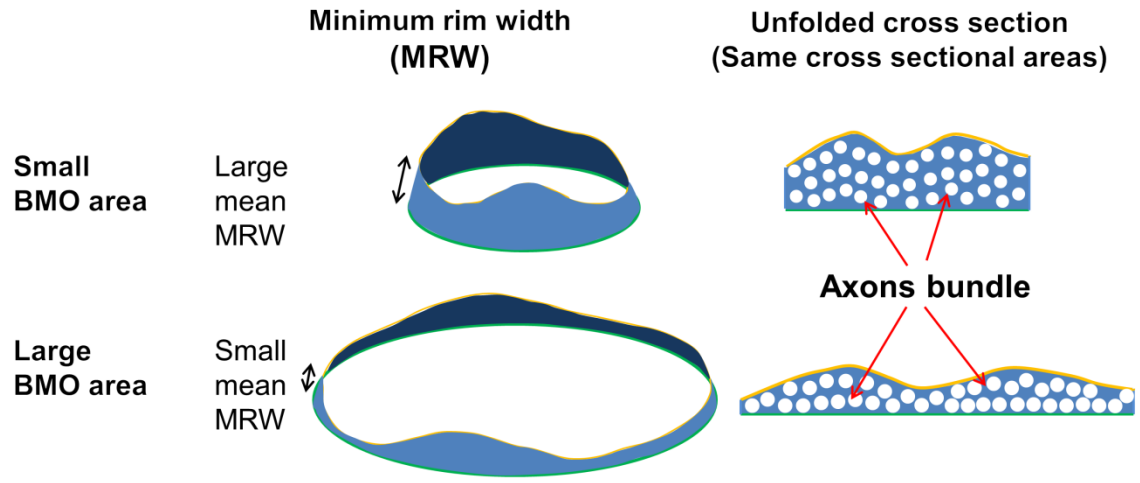

Figure 2-8. Schematic representations of mean MRW in an eye with a small BMO area (top row) and an eye with a large BMO area (bottom row). Based on results from Figure 2-4(a), mean MRW (blue region), given as the mean distance between the BMO ellipse (bottom green line) and ILM (top yellow line), was larger (thicker) in eyes with smaller BMO areas and was smaller (thinner) in eyes with larger BMO areas. However, mean sMRW was not significantly related to the size of the BMO [Figure 2-4(a)]. As depicted in the the right-most column, this result could suggest that relatively similar numbers of axons (white circles) exist within portions of the MRW that contain the same cross-sectional areas in young normal eyes with different sized BMOs. In this model, axons would need to stack on top of each other in an eye with a smaller BMO area in order to enter the ONH, yielding a larger mean MRW. However, less stacking would be required in an eye with a larger BMO area, yielding a thinner mean MRW.

In conclusion, while longer eyes tended to have larger BMO areas, there was no significant relationship between the length of the eye and the depth of the ALCS or the thickness of the MRW in our population of young, normal subjects. When examining relationships between ONH parameters, the fact that mean sMRW showed no relationship with BMO area could suggest that all normal, young eyes possess the same number of axons regardless of the size of the BMO. Furthermore, the decreased magnitude of mean MRW in eyes with more posteriorly-located ALCS's could result from an increased pull on the axons toward the BMO in eyes with a deeper lamina. The results from this study can serve as a normative database which can be compared with future measurements of these parameters in cross sectional groups of older normal eyes for studies examining ONH changes with age and in glaucoma patients to study morphological changes associated with disease.

2.5 Acknowledgements

This research was supported by National Institutes of Health (NIH) Grants R01 EY021783 (JP) and P30 EY007551 (Laura Frishman), and the University of Houston College of Optometry. The authors thank Sherine John, Kelsey Evans and Kwame Antwi-Bosiako for their contribution in data collection. The authors thank Hope Queener and Nripun Sredar for their helpful discussions.

CHAPTER 3

Examination of lamina cribrosa microarchitecture and optic nerve head geometry with normal aging

Contributing authors:

Nripun Sredar, Danica J Marrelli, OD, Hope M. Queener and Jason Porter, PhD

Abstract

Purpose: Age is a risk factor for glaucoma. Several studies suggest that normal aging could increase the susceptibility of the optic nerve head (ONH) to glaucomatous damage. We examined whether differences existed in anterior lamina cribrosa surface (ALCS) microarchitecture and ONH structure between (1) fellow eyes of normal human subjects and (2) younger and older normal eyes.

Methods: Spectral domain optical coherence tomography (SDOCT) images of the ONH and adaptive optics scanning laser ophthalmoscope (AOSLO) images of ALCS microarchitecture were acquired in one eye of 28 young (mean age = 25.7 ± 2.2 years) and 25 older (mean age = 57.5 ± 6.1 years) normal human subjects, and bilaterally in 32 of these subjects. ONH parameters were calculated from manually marked SDOCT radial B-scans. Anterior laminar pores were manually marked in AOSLO images and 3D transformed to calculate mean global pore area, elongation and nearest neighbor distance (NND). A Mann-Whitney rank sum test was used to assess statistical differences when comparing all parameters.

Results: ONH parameters were not statistically different between fellow eyes. Inter-eye differences in mean ALCS pore parameters were not significant in most eyes. Mean minimum rim width (MRW) was significantly smaller (thinner) in older vs young subjects (287.1 ± 35.6 µm vs 317.6 ± 49.5 µm, respectively; P=.02). However, there were no significant differences in any other ONH parameters between young and older eyes, including mean ALCS depth (young = 354.3 ± 83.58 µm, older = 342.6 ± 82.34 µm; P=.70). Mean pore area (young = 1999 ± 577 μm^2, older = 1988 ± 559 μm^2; P=1.0), elongation (P=.56) and NND (P=.19) were not significantly different between young and older eyes.

Conclusions: Most ONH and all mean global laminar pore parameters were similar between our young and older normal eyes. The measured decrease in mean MRW with age is consistent with the fact that retinal ganglion cell axon density decreases with normal aging. These normative data will serve as a basis for differentiating ONH structural changes in glaucoma.

3.1 Introduction

Glaucoma is defined as a group of progressive optic neuropathies that results in damage to retinal ganglion cell axons and the death of retinal ganglion cells (Quigley et al., 1981). This condition clinically presents as structural changes in optic nerve head (ONH) cupping and functional losses in vision (Quigley and Broman, 2006). While the mechanisms underlying glaucomatous neuropathy are not well understood, there is evidence that the initial damage to retinal ganglion cell axons occurs at the lamina cribrosa (Quigley and Anderson, 1976a).

Several studies have compared the structure of the lamina cribrosa and ONH between normal and glaucomatous eyes in human patients and between control and experimental glaucoma eyes in non-human primates (Minckler et al., 1977; Quigley and Anderson, 1977; Burgoyne et al., 2004; Downs et al., 2007; Yang et al., 2010; Quigley and Anderson, 1976). One implicit assumption in studies that select one eye from each subject at a single time-point or compare parameters between a diseased eye and its fellow control eye can be that the parameters under examination are similar between fellow normal eyes of the same subject. Therefore, it is not only important to have a better understanding of the variability inherent in these parameters across normal eyes, but also between fellow normal eyes of the same subjects, particularly when examining subtle changes or differences that occur in the earliest stages of disease in cross-sectional studies.

Few studies have reported the variability in lamina cribrosa microarchitecture and ONH structure between normal, fellow eyes. Using histomorphometric reconstructions, Yang et al. found the physiologic inter-eye percent difference in optic disc area, ONH connective tissue parameters (lamina cribrosa position and thickness), and ONH prelaminar neural tissue parameters (prelaminar tissue thickness and volume) to be relatively small (i.e., no more than 3% to 21%) in non-human primate eyes (Yang et al.,

2009). Ivers et al. (Ivers et al., 2015) later compared ONH structure and anterior lamina cribrosa surface (ALCS) microarchitecture between fellow eyes of 6 living normal monkeys and found ONH and ALCS pore parameters to be similar between right and left eyes. Given these results in normal, non-human primate eyes, it is important to better understand the variability in ONH and laminar pore parameters between fellow eyes of normal humans.

In addition, while multiple factors likely contribute to glaucoma, older age (a major risk factor for the onset and progression of the disease) (Gordon et al., 2002; Leske et al., 2003) could increase the susceptibility of the ONH to glaucomatous damage. Age-related changes have been noted in the normal lamina cribrosa and sclera. For example, increases in advanced glycation end products (AGEs) and in elastin and fibrillar forms of collagen (known to be structurally strong and rigid) have been reported within the extracellular matrix (ECM) of the normal human lamina cribrosa with increasing age (Hernandez et al., 1989; Albon et al., 1995; Albon et al., 2000a; Albon et al., 2000b). The degree of connective tissue fiber alignment within the peripapillary sclera has also been reported to increase with normal aging (Jones et al., 2015). Moreover, some reports suggest that changes in the lamina cribrosa during normal aging may be similar to changes observed during glaucoma. For example, increases in lamina cribrosa thickness have been reported in older, normal human eyes (Kotecha et al., 2006) and in early experimental glaucoma in monkeys (Burgoyne et al., 2004; Roberts et al., 2009a; Yang et al., 2015). Similarly, an accumulation of AGEs has been reported in the normal, aging lamina (Albon et al., 1995) and in the glaucomatous lamina compared to the laminas from normal, aged-matched eyes (Tezel et al., 2007). These normal changes could lead to the increased laminar stiffness reported in the aging eye (Albon et al. 2000b) and changes in laminar microarchitecture with normal

aging, potentially contributing to the increased susceptibility of the aged eye to the onset of glaucoma.

The main purposes of this study were to (1) characterize anterior lamina cribrosa surface (ALCS) microarchitecture and ONH geometry between fellow eyes of normal human subjects, and (2) determine whether differences existed in ALCS microarchitecture and ONH structure between young and older normal human eyes. This study provides improved understanding of the intra- and intersubject variabilities of ALCS and ONH morphology present within a normal population and the impact of aging on these structures.

3.2 Methods

All human subjects research adhered to the tenets of the Declaration of Helsinki. The study protocol was approved by the University of Houston's Committee for the Protection of Human Subjects and informed consent was obtained from each subject prior to the experiment. Young (20-30 years) and older (≥ 50 years) normal subjects were recruited to participate. Twenty-eight young (mean age = 25.7 ± 2.2 years; range = 21 - 30 years) and 25 older (mean age = 57.5 ± 6.1 years; range = 50 - 76 years) normal subjects were enrolled. 20 of our subjects were White (non-Hispanic), 17 were Asian, 7 were African-American and 9 were Hispanic, with 27 males and 26 females. All subjects had spherical equivalent refractive errors between +3.00 D and -6.00 D (with cylinder ≤ ±3.00 D), best corrected visual acuities better than or equal to 20/25, clear ocular media, intraocular pressures (IOPs) < 21 mmHg with no history of elevated IOP (assessed via Goldmann Applanation Tonometry), no clinically abnormal disc or retinal nerve fiber layer appearance (assessed using color strereoscopic optic disk photographs), and reliable Humphrey visual fields (24–2 Swedish Interactive Threshold Algorithm standard program; False positive and False negative rates < 33%, Fixation losses < 20%) with no

visual field defects. One eye was selected from each young and older subject for the study and dilated for imaging using 1.0% tropicamide and 2.5% phenylephrine. Fellow eyes were dilated and imaged in 32 of the 53 enrolled subjects.

3.2.1 Spectral domain optical coherence tomography (SDOCT) imaging and analysis

Wide-field scanning laser ophthalmoscope (SLO) fundus images and cross-sectional images of the ONH were acquired in each eye using the Heidelberg Spectralis HRA+OCT (Heidelberg Engineering). The wide-field images (15° or 30° field sizes) are useful during adaptive optics scanning laser ophthalmoscope (AOSLO) imaging sessions for navigating throughout the retina and ONH as the AOSLO imaging field is small (approximately 1.5 degrees). Cross sectional radial scans (48 B-scans, 20° field size, ART averaging of 16 frames) centered on the ONH were acquired with Enhanced Depth Imaging in all eyes. The Inner Limiting Membrane (ILM) was automatically segmented in each B-scan using the SDOCT instrument's software and any inaccuracies were manually corrected. The raw '.vol' files of all radial scans were then exported from the SDOCT instrument and extracted and analyzed via a custom semi-automated MATLAB program. The termination points of the retinal pigment epithelium (RPE)/Bruch's membrane (BM) interface and anterior lamina cribrosa surface were manually marked in as many B-scans as possible (Figure 3-1), from which a 3-dimensional point cloud of marked and segmented points could be generated (Figure 3-1c).

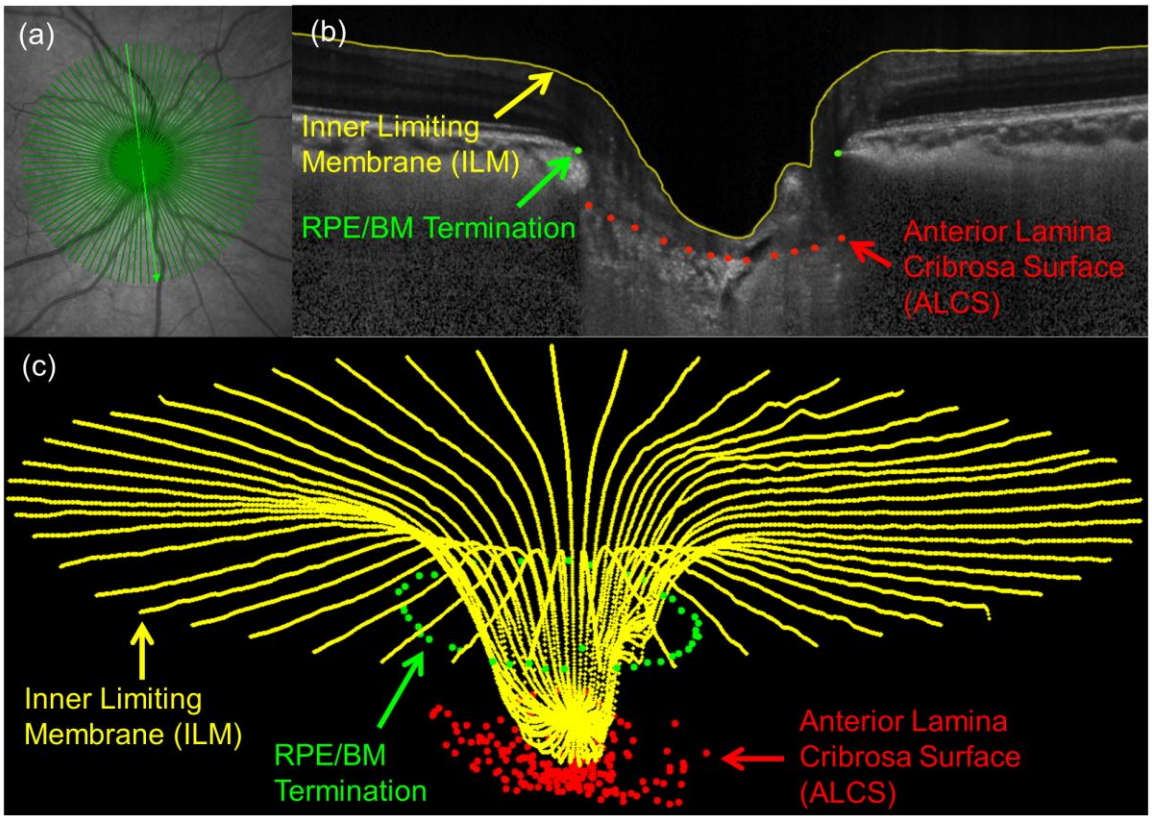

Figure 3-1. (a) Representative *en face* view of the ONH illustrating the locations of all 48 radial B-scans (green lines) acquired via SDOCT image using the EDI mode (16 frames averaged). (b) Single radial B-scan of the ONH corresponding to the scan location denoted by the bold green arrow in (a). Segmented and manually marked features included the ILM (yellow points), termination points of the RPE/Bruch's membrane complex (green points) and the anterior lamina cribrosa surface (red points). (c) 3-dimensional point cloud generated from landmarks delineated in each SDOCT radial B-scan from (a). (ILM in yellow, Bruch's Membrane Opening [BMO] in green, and anterior lamina cribrosa surface [ALCS] in red)

The delineated landmarks were used to quantify multiple ONH parameters. BMO area was first calculated as the area enclosed by an ellipse best-fit to the marked BMO points (Figure 3-2a). Mean anterior lamina cribrosa surface depth (ALCSD) was computed as the mean distance between a plane best-fit to the marked BMO points and a thin-plate spline surface that was fit to the marked ALCS points and used to model the ALCS in 3 dimensions (Figure 3-2b) (Sredar et al., 2013). Mean MRW, a potential surrogate marker of axonal density, was calculated as the mean of the minimum distances between the marked BMO points and the ILM surface across all B-scans (Figure 3-2c) (Strouthidis et al., 2011; Chauhan et al., 2013).

Additional ONH structural parameters were also quantified after fitting a 3-dimensional thin plate spline to the ILM point cloud. Prelaminar tissue volume (PTV) was computed as the volume between the ILM and anterior laminar surfaces that was contained within a hollow-cylinder extending from the edge of the BMO to the ALCS (Figure 3-3a) (Yang et al., 2007b; Strouthidis et al., 2011). Neuroretinal rim volume was calculated as the tissue volume anterior to BMO plane that was bounded by the ILM surface and a vertical perpendicular projection from the edge of the BMO (Figure 3-3a). (Yang et al., 2007b; Strouthidis et al., 2011)

Due to the fact that mean ALCSD does not provide information on the geometrical shape of the ALCS, we further characterized the ALCS by computing its mean radius of curvature (RoC) within the projection of the BMO ellipse (Figure 3-3b,c) (Sredar et al., 2013). Briefly, the RoC at a particular location on the ALCS is calculated as the ratio of the change in arc length to the change in the angle of the tangent between two given points juxtaposing the location being measured on the 3D ALCS. Mean RoC is the average of all the RoCs calculated at each point on the 3D interpolated ALCS.

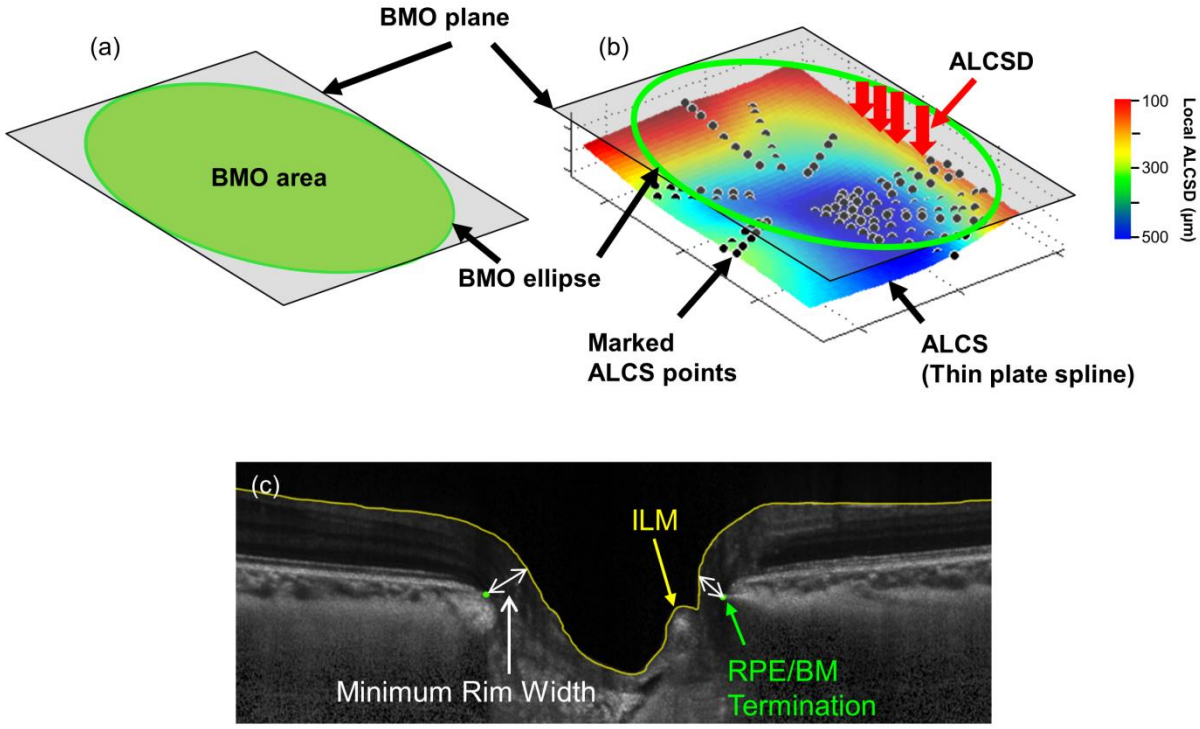

Figure 3-2. Method to calculate BMO Area, Mean ALCSD and mean minimum rim width (MRW). (a) An ellipse (bold, green line) was best-fit in 3-dimensions to the marked RPE/BM termination points and used to define a BMO plane. BMO area was calculated as the area enclosed by the BMO ellipse on the BMO plane. (b) After fitting a thin plate spline to the marked ALCS points (black dots, above and below the thin-plate spline), mean anterior lamina cribrosa surface depth (ALCSD) was calculated as the mean of the perpendicular distances from the BMO plane to the thin plate spline (red arrows) for points within the BMO ellipse. The color scale used in the thin-plate spline surface fit represents the local ALCSD at each point on the surface. Regions shaded in blue represent locations with increased values of mean ALCSD (i.e., more posteriorly located ALCS's within the ONH) while regions shaded in red represent locations with decreased values of mean ALCSD (i.e., more anteriorly located ALCS's). (c) Mean MRW was calculated by averaging the minimum distances measured between the delineated ILM surface (yellow line) and termination points of the BM/RPE interface (green dots) on each side of the neural canal opening (white arrows) across all marked B-scans.

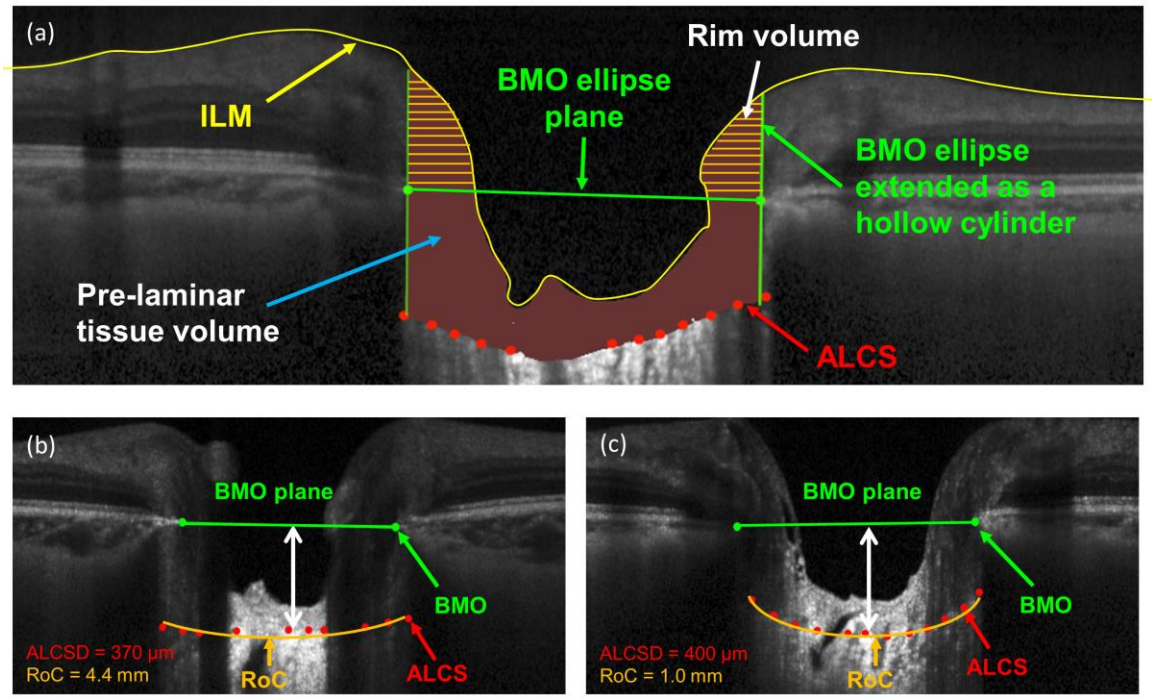

Figure 3-3. Illustration of Prelaminar Tissue Volume (PTV), Neuroretinal Rim Volume and ALCS RoC. (a) The ILM (yellow line), RPE/BM termination point (green dots) and ALCS (red dots) were segmented/marked in each radial B-scan. In a single B-scan, prelaminar tissue area (brown region) was computed as the area between the ILM and ALCS that was contained within a hollow-cylinder defined by the BMO ellipse. To compute prelaminar tissue volume, thin plate spline surfaces were fit to the 3-dimensional ILM and ALCS point clouds and used to calculate the volume between these surfaces that was confined within a hollow-cylinder extending from the BMO ellipse. Neuroretinal rim volume (hatched region) was calculated as the volume between the ILM surface and BMO plane that was contained within a vertical perpendicular projection from the BMO ellipse. (b,c) Eyes with similar values for mean ALCSD can have very different anterior lamina cribrosa surface shapes and curvatures. While mean ALCSD is similar in (b) (370 µm) and (c) (400 µm), the ALCS is flatter (i.e., larger RoC of 4.4 mm) in (b) and is steeper (i.e., smaller RoC of 1.0 mm) in (c). The orange arc represents the mean curvature of the ALCS.

3.2.2 Adaptive optics imaging of ALCS microarchitecture

Adaptive optics was used to correct each subject's optical aberrations over a dilated pupil (typically, ~8 mm) (Li et al., 2010). The ALCS microarchitecture was subsequently imaged in reflectance using an 840 nm wavelength superluminescent diode (S-Series Broadlighter, Superlum, Carringtwohill, Ireland) (Ivers et al., 2010; Ivers et al., 2011; Sredar et al., 2013) with a laser power of approximately 250 μW at the pupil plane (less than 10 times below the ANSI standards for safe light delivery to the eye) (ANSI, 2014). Videos were captured at 25 Hz over a 1.5° field. Through-focus images of the lamina were acquired at different depths to determine the plane of best-focus of the ALCS, or the location where ALCS pore boundaries first became sharpest and the image had optimal contrast. Videos of the ALCS microarchitecture were then acquired throughout as much of the ONH as possible. AOSLO videos were subsequently post-processed off-line using a custom program (MATLAB; The MathWorks, Inc., Natick, MA) to remove eye motion and create registered images that were then stitched together to create a montage of the anterior laminar surface (Adobe Photoshop; Adobe Systems, San Jose, CA) for each eye (Figure 3-4b). The image contrast of each AOSLO montage was improved using a contrast limiting adaptive histogram equalization (CLAHE) technique (ImageJ; developed by Wayne Rasband, National Institutes of Health, Bethesda, MD; available at http://rsb.info.nih.gov/ij/index.html).

Pores boundaries were manually marked (Adobe Photoshop) in as many locations as possible using previously described methods found to have excellent repeatability and reproducibility (Figure 3-4c) (Ivers et al. 2011). Because the *en face* AOSLO images represent a 2D projection of a 3D laminar surface, we transformed our 2D images into their approximate 3D morphology by registering and projecting the 2D AOSLO image onto the interpolated thin-plate spline surface that was best-fit to the ALCS points marked in the SDOCT B-scans (Figure 3-4d,e) (Sredar et al., 2013).

Following 3D transformation, we quantified the area, elongation (ratio of the major to minor axis of an ellipse best-fit to each pore boundary), and nearest neighbor distance (NND, nearest distance from the centroid of a given pore to that of its neighbors) of each marked pore using a custom MATLAB program (Ivers et al., 2011; Ivers et al., 2015). After computing all pore parameters in right and left eyes of each normal subject, we determined the mean, standard deviation and coefficient of variation for each parameter across all right eyes and across all left eyes.

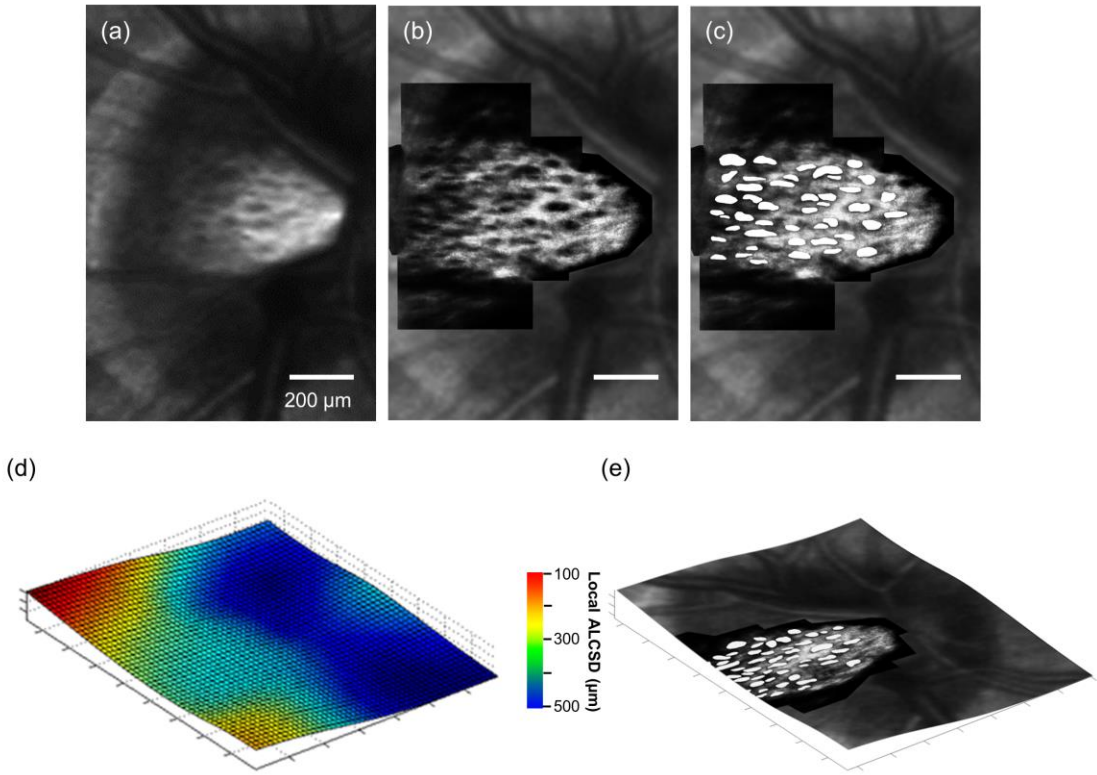

Figure 3-4. Adaptive optics imaging of the lamina cribrosa in a normal human eye. (a) Spectralis SLO image of the ONH when best focused on the anterior lamina cribrosa surface (ALCS). (b) A 2 dimensional AOSLO montage of the ALCS microarchitecture overlaid on the same Spectralis SLO image as in (a). The resolution and contrast of laminar beams and pores improved with adaptive optics correction. (c) Same image as in (b) in which laminar pores were manually marked (white) throughout as much of the imaged area as possible. Scale bar: 200 µm. (d) An interpolated thin plate spline surface was fit to the ALCS points manually marked in SDOCT radial B-scan images acquired in the same eye (see Figure 3-1b for an explanation of marking). The depth of the ALCS at each point on the thin-plate spline surface (local ALCSD) is color-coded using the scale on the right side of the image, with more posteriorly-located surface points represented in blue and more anteriorly-located surface points represented in red. (e) 3D AOSLO montage constructed by registering and projecting the 2D AOSLO image from (c) onto the thin plate spline surface from (d). All pore values were quantified from the 3D transformed images.

3.2.3 Biometric measurements and image scaling

Biometric measurements of axial length, anterior chamber depth and anterior corneal curvature were acquired using the IOL Master (Carl Zeiss Meditec) or LenStar LS 900 (Haag-Streit). These biometric parameters were used to laterally scale field sizes in AOSLO and SDOCT images from visual angle (in degrees) to physical retinal size (in micrometers). Conversions were performed by incorporating these biometry measurements into a 4-surface model eye (Li et al., 2010; Ivers et al., 2011).

3.2.4 Data and Statistical Analyses

All statistical tests were performed using commercially available software (SigmaPlot; Systat Software Inc., San Jose, CA). A non-parametric Mann-Whitney Rank sum test was used to assess whether statistically significant differences existed in mean ONH and ALCS pore parameters between fellow eyes (as all parameters were not normally distributed) and whether all ALCS pores quantified in an individual's left eye were statistically different from those quantified in the same individual's right eye. In addition, the Mann-Whitney test was used to determine whether significant differences existed in ONH and ALCS pore parameters between young and older normal subjects. Linear regression analyses were also performed between ONH and ALCS pore parameters to investigate potential relationships in right eyes, left eyes, young eyes and old eyes. *P* values < .05 were taken to represent a statistically significant difference for the parameters analyzed.

3.3 Results

3.3.1 Comparison of ONH structure and ALCS microarchitecture between fellow eyes

ONH structure and laminar microarchitecture were similar between fellow eyes of normal subjects. Figure 3-5 shows representative images of ALCS pore microarchitecture (with marked pores) and corresponding ONH structure from right and left eyes of the same individuals. No statistically significant differences were measured for any ONH or laminar pore parameters between right and left eyes across 32 subjects (mean age = 37.1 ± 15.9 years; range = 21 - 66 years) (P >.05) (Table 3-1). When examining ONH parameters, the mean percent difference between fellow eyes was highest for mean RoC (19.2 ± 20.2%), but was less than 10% for all other analyzed parameters. The coefficients of variation (CV) for all ONH parameters ranged between 11.16% and 26.13%, indicating a large variability in some parameters across this normal population.

Mean global pore parameters were also not statistically different between all right and left eyes of our study population (P >.05) (Table 3-1). The mean percent difference between right and left eyes was highest for mean pore area (24.6 ± 16.9%) and mean pore NND (24.8 ± 22.8%), and was lowest for mean pore elongation (15.6 ± 10.9%). Large variations in all 3 pore parameters were noted across eyes, as CVs ranged between 13.67% and 27.67%. The maximum variability was seen in mean pore area while the minimum variability was measured in mean pore elongation.

Table 3-1: Comparison of ONH and anterior lamina cribrosa pore parameters between right and left eyes of 32 normal subjects.

ONH Parameters	RIGHT EYES		LEFT EYES		Mean % Difference between fellow eyes	Mann Whitney test (*P-value*)
	Mean ± SD	Coefficient of Variation (%)	Mean ± SD	Coefficient of Variation (%)		
BMO area	1.906 ± 0.381	19.98	1.929 ± 0.431	22.33	8.0 ± 6.8	0.86
Mean ALCSD (µm)	355.1 ± 77.6	21.86	347.0 ± 78.2	22.53	8.0 ± 7.9	0.72
Mean RoC (mm)	3.74 ± 0.78	20.95	3.60 ± 0.94	26.13	19.2 ± 20.2	0.69
Prelaminar Tissue Volume (mm3)	0.991 ± 0.174	17.53	1.007 ± 0.201	19.95	6.0 ± 4.3	0.86
Rim Volume (mm^3)	0.402 ± 0.093	23.14	0.421 ± 0.110	26.11	8.7 ± 8.7	0.64
Mean MRW (µm)	307.5 ± 46.4	15.10	308.8 ± 42.3	13.69	4.9 ± 5.1	0.99
Mean RNFL Thickness (µm)	97.45 ± 10.88	11.16	97.52 ± 11.26	11.55	2.7 ± 3.1	0.90
Mean Pore Area ($µm^2$)	2259 ± 604	26.75	2222 ± 615	27.67	24.6 ± 16.9	0.98
Mean Pore Elongation	2.06 ± 0.28	13.67	2.08 ± 0.39	18.53	15.6 ± 10.9	0.86
Mean Pore NND (µm)	79.6 ± 20.6	20.83	73.9 ± 18.1	24.52	24.8 ± 22.8	0.33

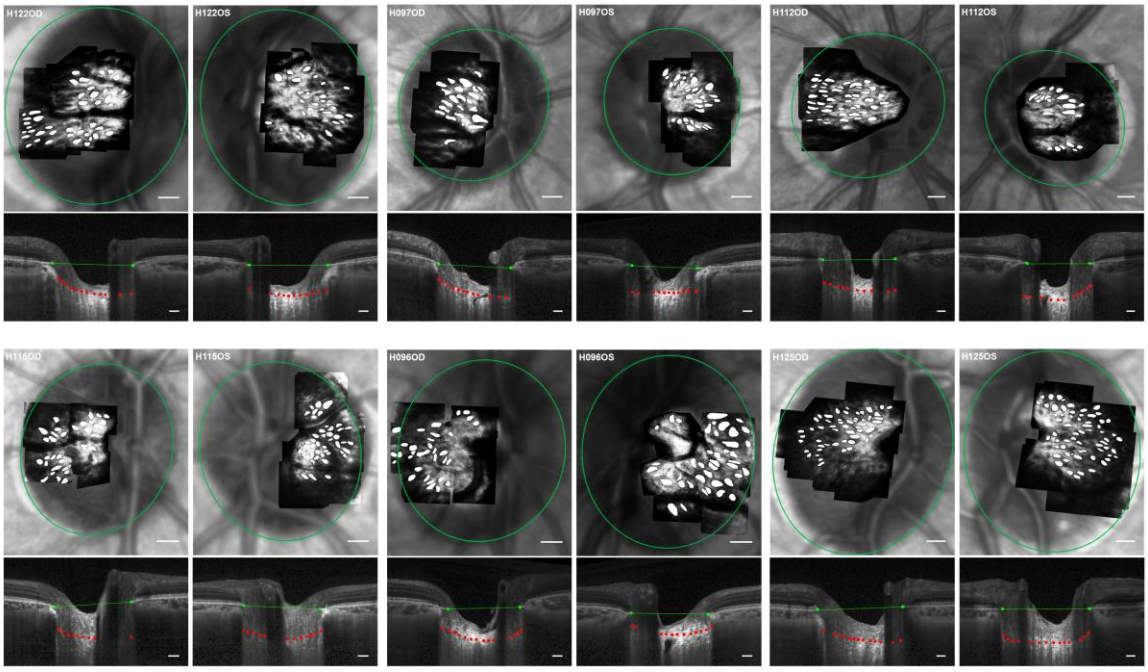

Figure 3-5. AOSLO montages of the ALCS microarchitecture overlaid on SLO images (rows 1 and 3) and corresponding SDOCT cross-sectional B-scans of the ONH (rows 2 and 4) acquired in right (OD) and left (OS) eyes of six representative normal subjects. Laminar pore boundaries are outlined in yellow and pores are filled in white. Manually marked termination points of the BM/RPE interface are noted in green and the anterior laminar surface points are noted in red in SDOCT images. The green ellipse overlaid on each SLO image represents the BMO ellipse.

While mean global ALCS pore parameters were not statistically different when comparing all 32 right eyes versus all 32 left eyes, statistically significant differences were noted in laminar pore parameters between fellow eyes of some individuals when examined on a subject by subject basis. A statistically significant difference in pore area was calculated in 9 of 32 subjects when comparing the areas of all pores marked in each subject's right eye versus those marked in the corresponding left eye. Significant differences in pore elongation and pore NND were found between fellow eyes in 7 of 32 and 11 of 32 subjects, respectively.

We also examined the degree of relationship between ONH parameters and between ONH parameters and axial length for all right and left eyes. BMO area was significantly larger ($P<.05$) in eyes with increased axial lengths (Figure 3-6a), indicating that longer eyes typically had larger BMO areas. Correspondingly, eyes with larger BMO areas also had increased prelaminar tissue volumes (Figure 3-6b) and neuroretinal rim volumes (Figure 3-6c). Mean RoC was not significantly correlated with mean ALCSD across eyes (Figure 3-6d), indicating that the curvature of the ALCS is not related to its position within the ONH. (In other words, more posteriorly-located ALCS's were not more "cupped" with increased curvature in normal eyes). In addition, mean MRW was significantly larger (thicker) in eyes with larger neuroretinal rim volumes (right eyes: $R^2 = 0.61$, $P < .001$; left eyes: $R^2 = 0.44$, $P < .001$). Neuroretinal rim volume was also significantly higher in eyes with larger prelaminar tissue volumes (right eyes: $R^2 = 0.40$, $P < .001$; left eyes: $R^2 = 0.36$, $P < .001$).

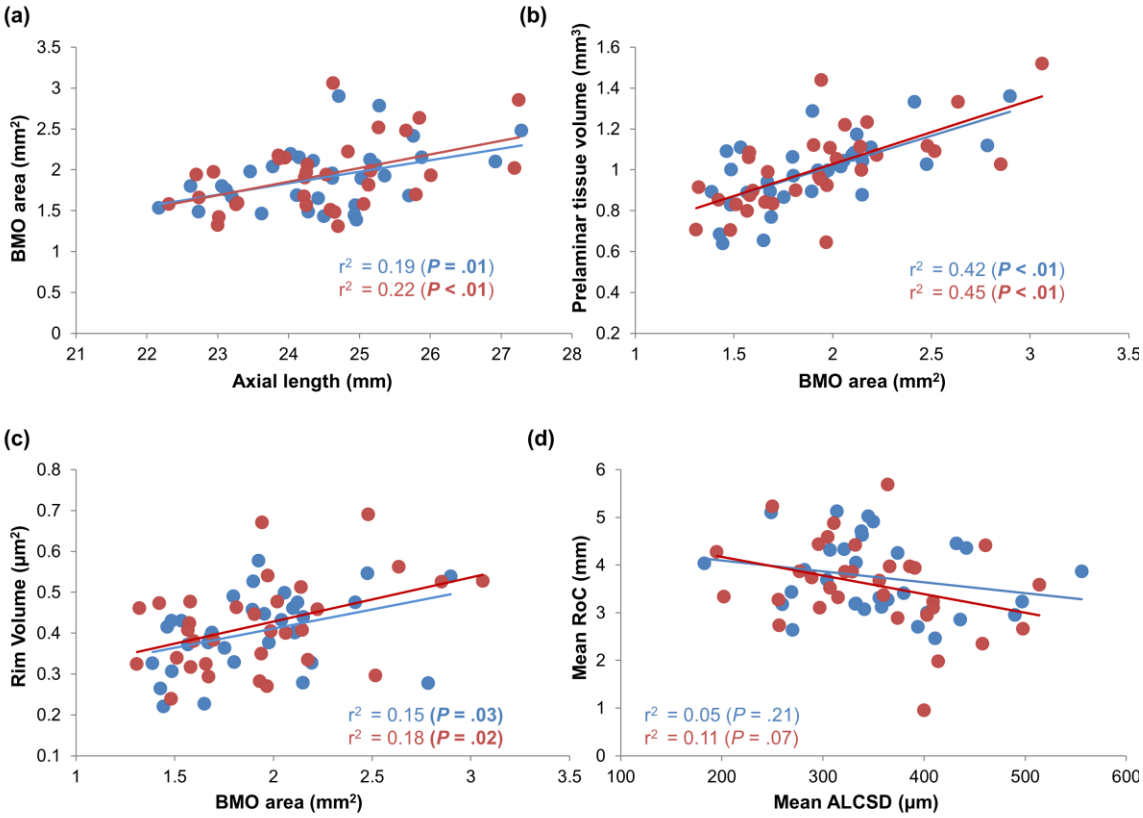

Figure 3-6. Comparison of ONH parameters with axial length and other ONH parameters for right and left eyes of 32 normal subjects. Blue circles represent right eyes and red circles represent left eyes. Solid lines indicate linear regressions fit to the corresponding data points. (a) BMO area was significanty larger in eyes with longer axial lengths. (b) Prelaminar tissue volume and (c) neuroretinal rim volume were significantly greater in eyes with larger BMO areas. (d) Mean RoC was not significantly correlated with the depth of the ALCS (or value of mean ALCSD) in right or left eyes, indicating that the curvature of the ALCS was independent of its position within the ONH.

When examining the degree of correlation between global ALCS pore microarchitecture, ONH parameters and axial length, we found no statistically significant relationship between mean ALCS pore area and axial length (Figure 3-7a). Mean ALCS pore elongation was significantly related to axial length in right eyes (Figure 3-7b), indicating that right eyes with longer axial lengths tended to have ALCS pores that were more elliptically shaped. A similar relationship was not measured, however, in the left eyes of the same subjects. As with pore elongation, mean ALCS pore area was significantly correlated with BMO area in right eyes only (Figure 3-7c). While right eyes with larger BMO areas tended to have larger mean ALCS pore areas, the same observation was not found in left eyes. In addition, mean pore area was not related to mean ALCSD (Figure 3-7d). In other words, pore areas did not tend to be systematically larger or smaller depending on whether the ALCS was positioned more anteriorly or posteriorly within the ONH. Also, mean ALCS pore NND was not significantly related to axial length, BMO area, mean ALCSD, mean RoC, mean MRW or RNFL ($P>.05$).

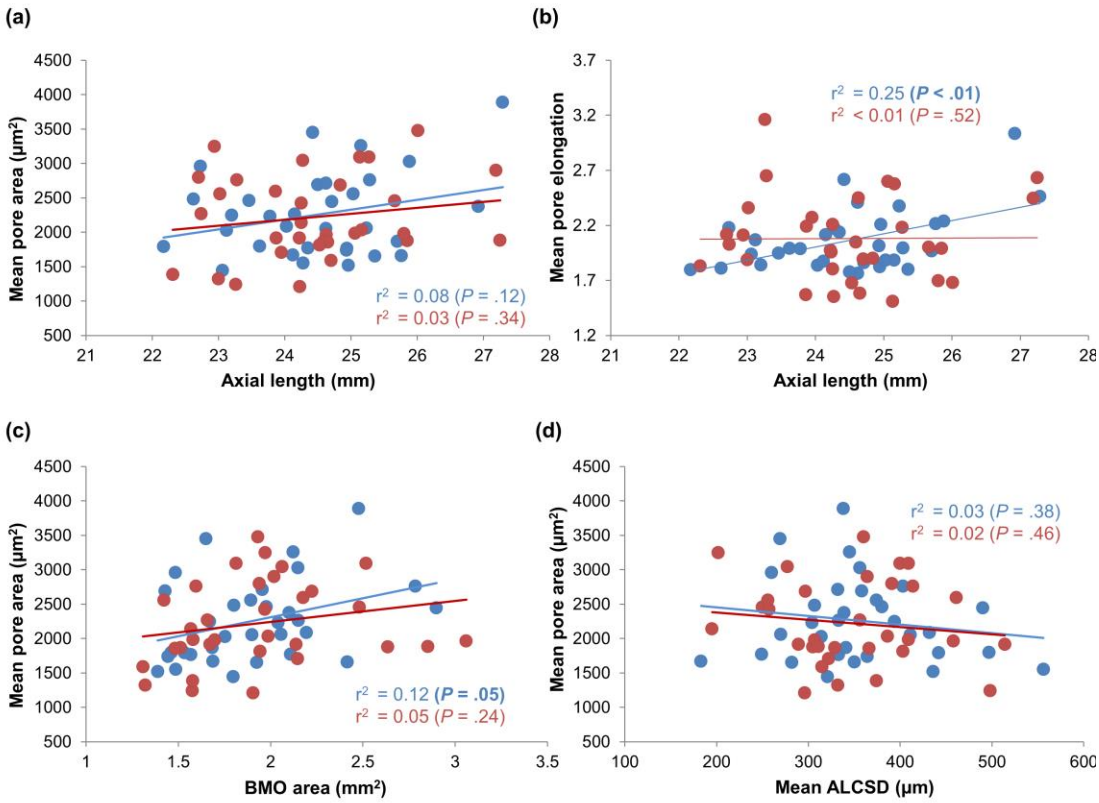

Figure 3-7. Comparison of global ALCS pore parameters with axial length and with ONH parameters for right and left eyes of 32 normal subjects. Blue circles represent right eyes and red circles represent left eyes. Solid lines indicate linear regressions fit to the corresponding data points. (a) No significant relationship was found when comparing global values of mean pore area with axial length. (b) Mean pore elongation significantly increased with increasing axial length in right eyes. However, the same relationship was not observed in left eyes. (c) Similarly, global mean ALCS pore area significantly, but weakly, increased with an increase in BMO area in right eyes, indicating that right eyes with larger BMO areas tended to have larger mean ALCS pore areas. However, no significant relationship was found between mean ALCS pore area and BMO area in left eyes. (d) Mean pore area was not significantly related to mean ALCSD in right or left eyes.

3.3.2 Comparison of ONH structure and ALCS pore microarchitecture between young and older normal eyes

The majority of ONH and global ALCS pore parameters were not significantly different between young and older normal eyes. Figure 3-8 shows representative images of ALCS pore microarchitecture (with marked pores) and corresponding ONH structure from young and older normal eyes. Out of all ONH parameters that were examined, mean MRW was the only one to be significantly different between young and older eyes. Young eyes had significantly larger values of mean MRW (317.6 ± 49.5 μm) compared to older eyes (287.1 ± 35.6 μm) (Table 3-2, Figure 3-9b). Values of mean ALCSD, a parameter shown to be significantly larger in glaucomatous eyes compared to normal eyes, were not statistically different between young and older eyes (Table 3-2, Figure 3-9a). Prelaminar tissue volume, neuroretinal rim volume and mean RNFL thickness were also not statistically different between the two groups (Table 3-2; Fig 3-9b,d). While mean ALCS pore area was larger in younger eyes compared to older eyes (1999 ± 577 μm^2 vs 1988 ± 559 μm^2, respectively), the difference between the groups was not statistically significant (P = 1; Figure 3-9c). Mean ALCS pore elongation and NND were also not statistically significantly different between young and older eyes (P >.05; Table 3-2).

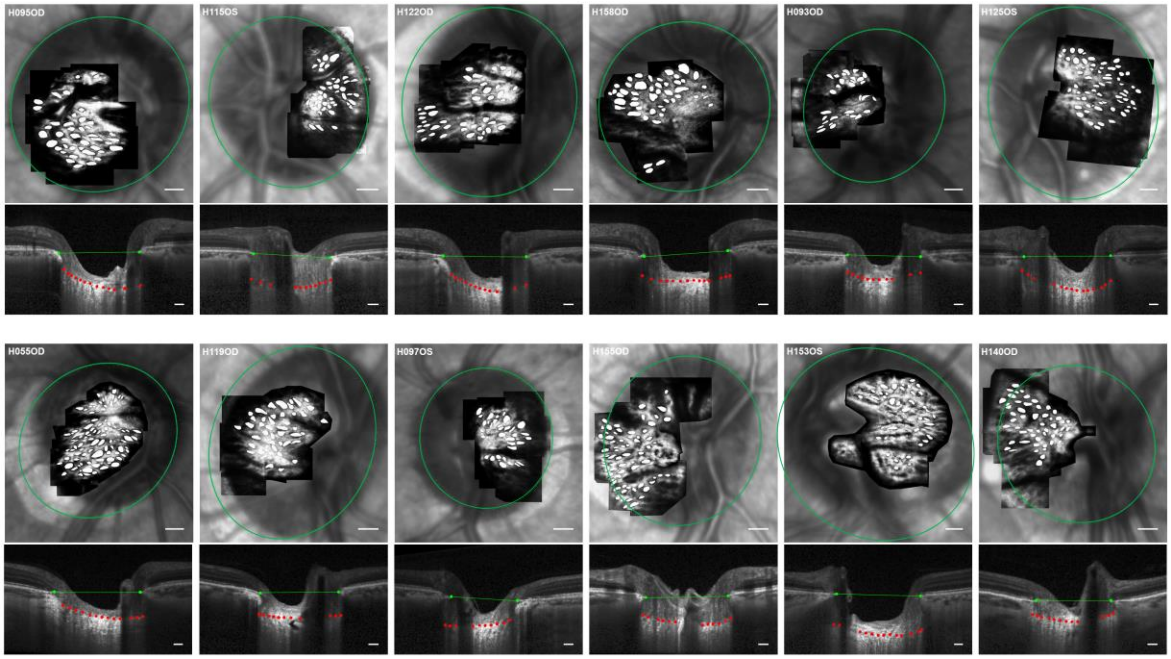

Figure 3-8. AOSLO montages of the ALCS microarchitecture overlaid on SLO images (rows 1, 3) and corresponding SDOCT cross-sectional B-scans of the ONH (rows 2, 4) from eyes of six representative normal young subjects(rows 1-2) and six representative normal older subjects (rows 3-4). Laminar pore pores are filled in white. Manually marked termination points of the BM/RPE interface are noted in green and the anterior laminar surface points are noted in red in SDOCT images. The green ellipse overlaid on each SLO image represents the BMO ellipse.

Table 3-2: Comparison of ONH and ALCS pore parameters between young and older normal eyes.

	Younger Eyes 28 eyes Mean age: 25.7 ± 2.2 years	Older Eyes 25 eyes Mean age: 57.5 ± 6.1 years	Mann-Whitney (*P-value*)
	Mean ± SD	**Mean ± SD**	
BMO Area (mm^2)	2.094 ± 0.480	2.084 ± 0.519	.91
Mean ALCSD (µm)	354.1 ± 83.73	342.2 ± 82.48	.70
Mean RoC (mm)	3.56 ± 0.76	3.96 ± 1.25	.39
Prelaminar Tissue Volume (mm^3)	1.094 ± 0.223	0.977 ± 0.184	.09
Rim Volume (mm^3)	0.462 ± 0.158	0.412 ± 0.120	.22
Mean MRW (µm)	317.6± 49.5	287.1 ± 35.6	.02*
Mean RNFL Thickness (µm)	100.31 ± 11.67	98.04 ± 7.0	.18
Mean Pore Area ($µm^2$)	1999 ± 577	1988 ± 559	1.0
Mean Pore Elongation	2.07 ± 0.30	2.03 ± 0.25	.56
Mean Pore NND (µm)	68.35 ± 12.5	76.04 ± 18.67	.19

***** Statistically significant difference between young and older eyes (*P*<.05)

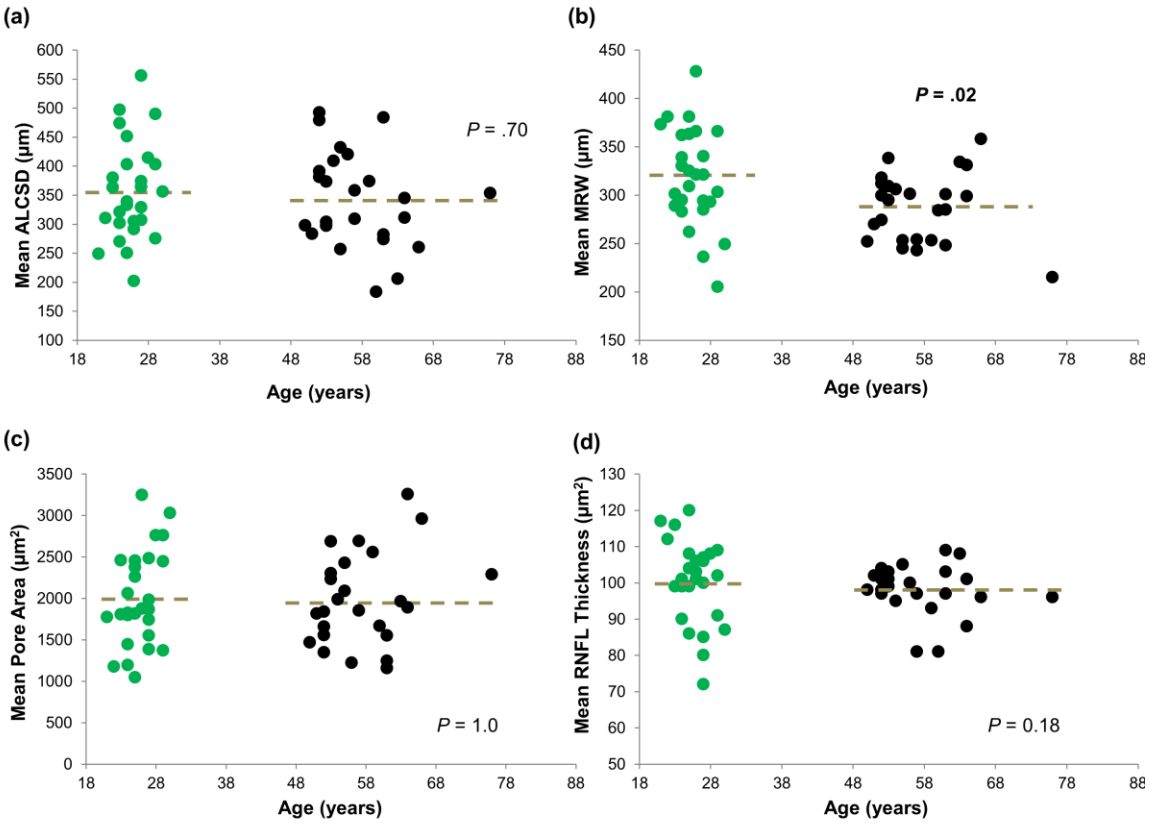

Figure 3-9. ONH and global ALCS pore parameters plotted as a function of age. Green circles represent young subjects and black circles represent older subjects. Gray dashed lines indicate the mean value for each age group. (a) No statistically significant difference in mean ALCSD was found between young and older eyes (*P*=.70). (b) Mean MRW was significantly reduced in older eyes compared to young eyes (*P*=.02), potentially indicating that older eyes had reduced numbers of retinal ganglion cell axons compared to young eyes. (c) No statistically significant difference in mean ALCS pore area was found between young and older eyes (*P*=.97). (d) Likewise, no statically significant difference in mean RNFL thickness was found between young and older eyes (*P* = .18).

We examined the relationships between ONH structure, global ALCS pore parameters and axial length within the young and older age groups. BMO area was significantly larger in eyes with increased axial lengths for both young (P=.02) and older (P<.01) subjects. However, no other ONH parameters (including mean ALCSD, mean RoC or mean MRW) were significantly related to axial length in young or older eyes (P>.05). Mean ALCSD significantly correlated with mean MRW in young eyes (R^2 = 0.19, P =.02), indicating that young eyes with more anteriorly-located ALCS's (smaller mean ALCSD's) tended to have thicker MRWs (Figure 3-10a). However, this relationship was not present in the older eyes. No statistically significant correlations were found between mean MRW and prelaminar tissue volume (Figure 3-10b), mean RoC (Figure 3-10c) and RNFL thickness (Figure 3-10e) for young or older eyes. In addition, there was no relationship between mean RoC and mean ALCSD for either group (Figure 3-10d), indicating that the anterior laminar surface was not necessarily more curved (or "cupped") in eyes with more posteriorly-located ALCS's (or larger mean ALCSD's) as might be expected in glaucomatous eyes. Finally, there were no statistically significant relationships between any ALCS pore and ONH parameters within young or older groups of eyes, including comparisons made between mean ALCS pore area and axial length, mean ALCSD and mean MRW (Figure 3-11).

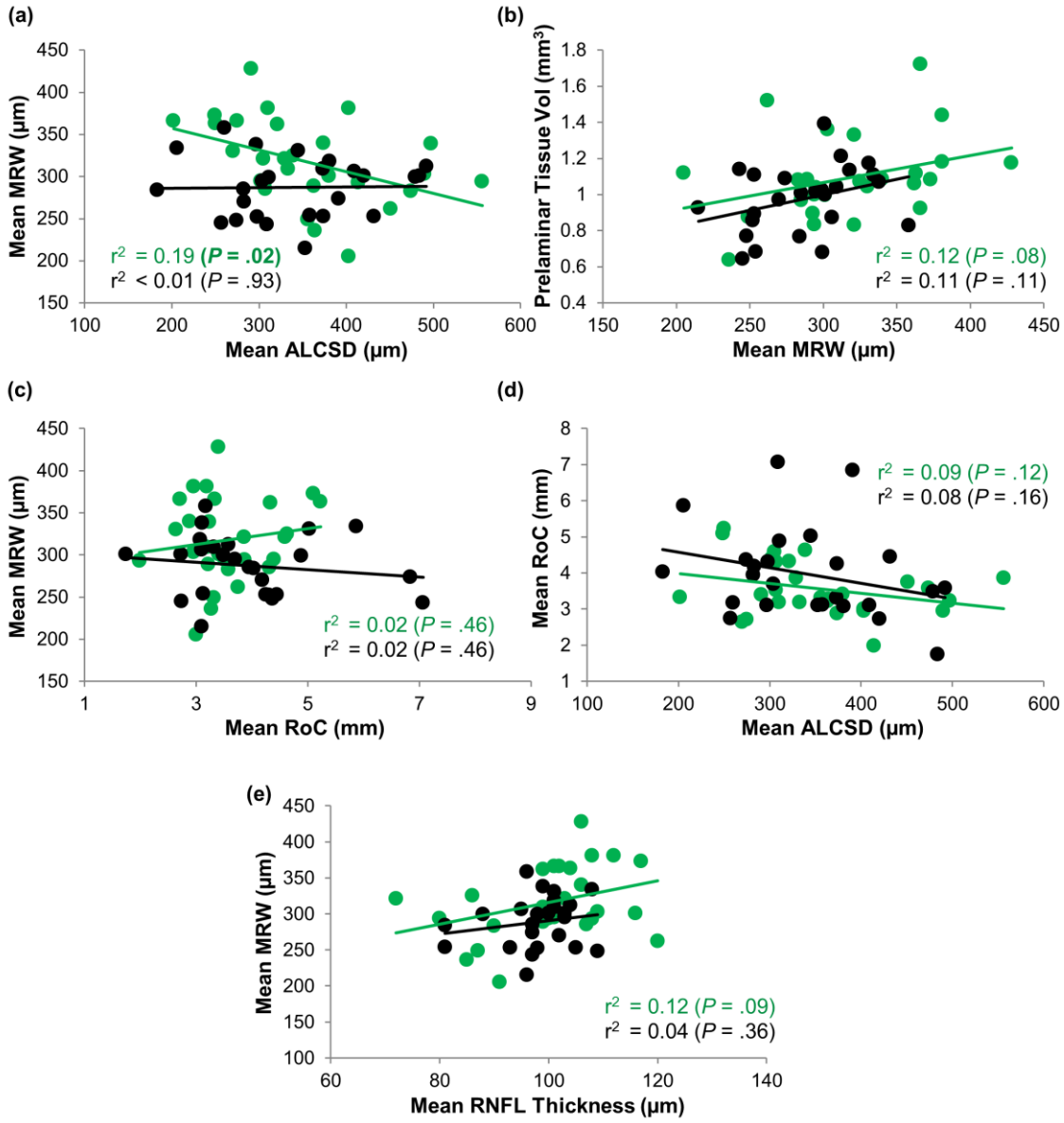

Figure 3-10. Comparison of ONH parameters for young, normal eyes (green circles) and older, normal eyes (black circles). Solid lines indicate linear regressions fit to the corresponding data points. (a) There was a statistically significant relationship between mean ALCSD and mean MRW in young eyes, as eyes with larger values of mean MRW tended to have smaller values of mean ALCSD. However, no relationship was observed in older eyes between these 2 parameters. (b) No significant correlation was measured between prelaminar tissue volume and mean MRW in young and older eyes. In addition, there was no significant correlation

between the mean RoC of the ALCS and (c) mean MRW or (d) mean ALCSD in young or older eyes. (e) No significant correlations were measured between mean MRW and mean RNFL thickness for young or older normal eyes.

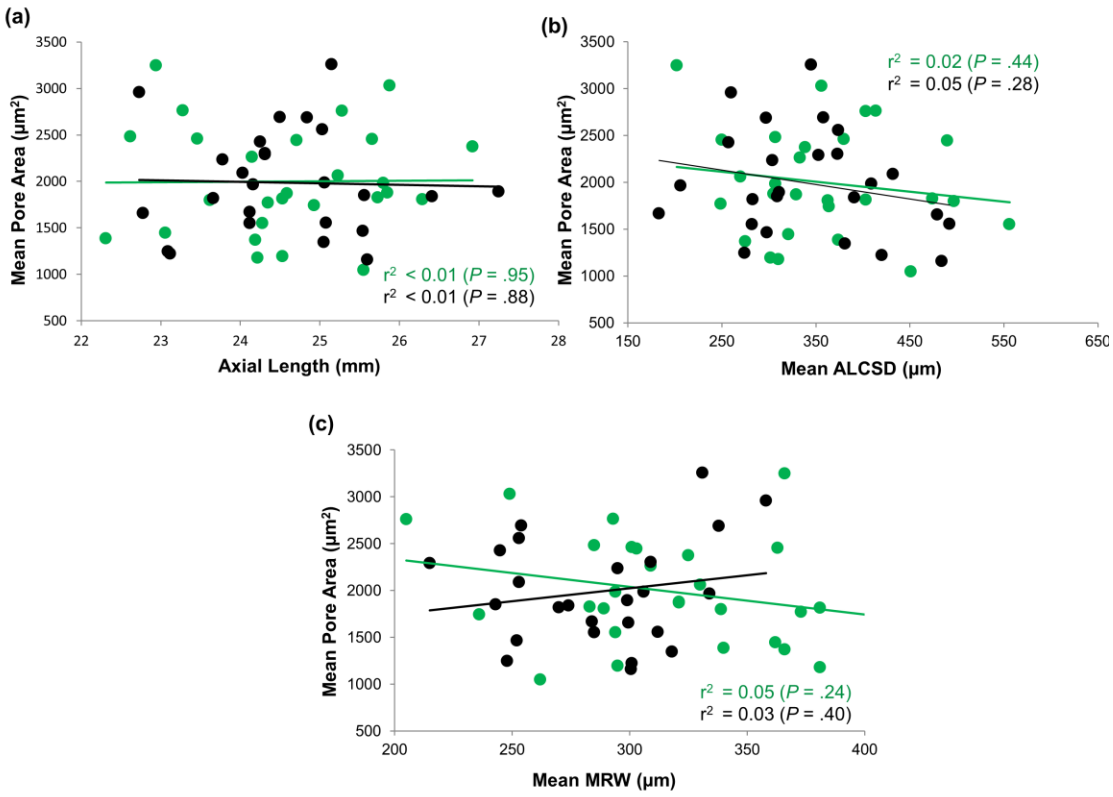

Figure 3-11. Comparison of mean ALCS pore area with axial length and ONH parameters for young, normal eyes (green circles) and older, normal eyes (black circles). Solid lines indicate linear regressions fit to the corresponding data points. For both young and older eyes, global mean ALCS pore area was not significantly related to (a) axial length, (b) mean ALCSD or (c) mean MRW.

3.4 Discussion

The purposes of this study were to (1) characterize anterior lamina cribrosa surface (ALCS) microarchitecture and ONH geometry between fellow eyes of normal subjects, and (2) determine whether differences existed in ALCS microarchitecture and ONH structure between young and older normal human eyes. *In vivo* AOSLO images of ALCS microarchitecture and SDOCT images of ONH structure were acquired to quantify ALCS pore parameters and ONH geometry in groups of young and older normal subjects. To our knowledge, this study provides the first *in vivo* comparison of ALCS microarchitecture and ONH geometry between fellow eyes of normal human subjects. It is also the first study to quantify and correlate ALCS microarchitecture and ONH geometry across normal eyes of different ages. While ALCS microarchitecture and ONH geometry were similar between fellow eyes and between younger and older eyes, we found that older eyes had significantly thinner MRWs compared to young eyes.

The mean values of the ONH parameters measured in this study (Table 3-1) were similar to those reported in previous studies. For example, the BMO areas measured across all right eyes and all left eyes of our normal subjects (1.906 ± 0.381 mm^2 and 1.929 ± 0.431 mm^2, respectively) are similar to the median BMO area reported by Chauhan et al. (1.7 mm^2) in 48 normal subjects (median age = 65 years) (Chauhan et al., 2013). Our measured values of mean ALCSD across all right eyes and all left eyes (355.1 ± 77.6 μm and 347.0 ± 78.2 μm, respectively) are also very similar to that reported by Furlanetto et al. (353 ± 70 μm) in 57 normal subjects (mean age = 56 ± 17 years) (Furlanetto et al., 2013). In addition, our mean values of MRW (a potential surrogate metric for the number of retinal ganglion cell axons that pass into the ONH) measured across all right eyes and all left eyes (307.5 ± 46.4 μm and 308.8 ± 42.3 μm, respectively) are comparable to the median MRW reported by Chauhan et al. in their healthy control eyes (316.5 μm) (Chauhan et al., 2013).

The mean values of ALCS pore parameters measured in this study (Table 3-1) were also similar to previously reported data. Our measured values of mean pore elongation in all right eyes and all left eyes (2.06 ± 0.28 and 2.08 ± 0.39, respectively) were comparable to values reported by Akagi et al. (2.13 ± 0.47) in 20 normal eyes and Wang et al. (2.06 ± 0.14) in 19 normal eyes (Akagi et al., 2012; Wang et al., 2013). Mean values of ALCS pore area measured across all right eyes and all left eyes in our normal subjects (2,259 ± 604 μm^2 and 2,222 ± 615 μm^2, respectively) were in between mean values measured using swept source OCT (1,970 ± 310 μm^2) by Wang et al. (Wang et al., 2013) and using AOSLO imaging (2,507.7 ± 825.5 μm^2) by Akagi et al. (Akagi et al., 2012). The values of pore parameters measured by Akagi et al. are likely to be more directly comparable to those measured in our experiment as both studies used an AOSLO to directly image and quantify pore areas on the ALCS. The study by Wang et al. used swept source OCT to visualize laminar pores throughout the thickness of the lamina. Therefore, the values reported in their study reflect the mean area of pores located at all depths in the lamina (as opposed to just the anterior surface, as reported in this study).

There were no statistical differences between the mean values of any examined ONH parameters between right and left eyes of our normal subjects. The three global ALCS pore parameters measured in this study (mean pore area, elongation and NND) were not statistically different between right and left eyes when comparing mean values in all right eyes versus mean values in all left eyes. However, when ALCS pore parameters were compared between right and left eyes of each individual subject (i.e., the areas of all pores marked in the right eye were compared with the areas of all pores marked in the fellow eye of the same subject), statistically significant differences were observed in some parameters within some individuals on a global scale. One potential reason that could account for these differences is that ALCS pores were sometimes

imaged and quantified in different regions between fellow eyes (for example, see subject H112 in Figure 3-5). Typically, it is not possible to image the entire anterior lamina cribrosa surface (ALCS) due to facts that the neuroretinal rim and overlying vessels can cast shadows onto the ALCS and different eyes have different prelaminar tissue thicknesses, making it challenging to visualize all of the ALCS microarchitecture. Therefore, we attempted to image as much of the ALCS microarchitecture as possible in each eye, leading to the possibility that slightly different regions were imaged in different eyes (and even between fellow eyes of the same subject). Performing a local analysis of pore parameters (e.g., comparisons only within the same region or sector) would shed more light on whether the statistical differences found in some pore parameters between fellow eyes of some subjects were potentially due to the quantification of pores in different regions and could be the topic of a future study.

We examined relationships between ONH structure and ALCS pore microarchitecture with axial length across eyes of different ages, within young eyes and within older eyes. Eyes that were axially longer tended to have larger BMO areas (Figure 3-6a). However, there was no relationship between the length of an eye and the position of its anterior laminar surface (or mean ALCSD). In addition, while there was a statistically significant relationship between mean ALCS pore elongation and axial length across right eyes of our normal subjects (Figure 3-7b), we found no significant relationship between mean global ALCS pore area and axial length across all eyes (Figure 3-7a) or across all young eyes and across all older eyes (Figure 3-11a). This latter finding (i.e., mean pore area vs. axial length) is in opposition to a previous result by Akagi et al. who reported a significant increase in mean pore area with increasing axial length (P=.008) in 20 normal eyes (Akagi et al., 2012). The reasons for this discrepancy are unknown, but could potentially be due to differences in the racial make-up of the 2 study populations. The subjects reported by Akagi et al. were of Japanese ethnicity,

while our study subjects were predominantly White, Asian (Indians and Chinese) and African-American. Multiple studies have shown that ONH structure can vary considerably across races and ethnic groups (Dandona et al., 1990; Girkin et al., 2004; Girkin et al., 2011; Knight et al., 2012; Rhodes et al., 2014). In addition, the Akagi et al. study reported pore areas quantified in 2D while our study reports 3D transformed pore areas. Previous work in normal non-human primate eyes has shown a modest average change in pore area (5.1 ± 2.0%) after transforming pores from 2D to 3D, largely due to the fact that the ALCS is relatively flat in normal non-human primate eyes (Sredar et al., 2013). While similar data has not been reported in human eyes, we believe that 3D pore transformation provides a more accurate quantification of pore parameters as it takes into consideration the anatomical contour of the 3D ALCS.

We also sought to better understand the relationships between ALCS position (mean ALCSD), shape (mean RoC) and pore microarchitecture in normal eyes. None of these parameters were significantly correlated with each other across individuals. There was no statistically significant relationship between mean ALCSD and mean RoC (Figure 3-6d), indicating that more posteriorly-located ALCSs did not necessarily possess more curved surfaces. Likewise, the lack of a significant relationship between mean ALCSD and mean global ALCS pore area (Figure 3-7c, Figure 3-11b) indicates that the mean area of ALCS pores are independent of the depth of the ALCS within the ONH (or eyes with deeper ALCSs do not necessarily possess larger ALCS pores).

With the exception of mean MRW, there were no statistically significant differences in any ONH parameter between our young and older normal populations. The values of mean MRW measured in our older eyes (287.1 ± 35.6 µm) were significantly lower than those measured in young eyes (317.6 ± 49.5 µm) (Table 3-2). This finding is in agreement with a previous study by Patel et al. that reported a decrease in mean MRW with increasing age (Patel et al., 2014a) and with clinical

observations that the optic nerve rim thins with normal aging (Dr. George Spaeth, personal communication). However, despite these differences in mean MRW between age groups, RNFL thickness measurements were not significantly different between young and older eyes in our study (*P* =.18). The reasons for why there was a significant difference between young and older eyes for mean MRW, but not for RNFL thickness (which has also been shown to thin with increasing age (Patel et al., 2014a), are not clear. Changes in mean MRW have been shown to occur earlier than changes in RNFL thickness in non-human primate models of experimental glaucoma (Fortune et al., 2013; He et al., 2014b; Patel et al., 2014b; Ivers et al., 2015). If mean MRW is a more sensitive metric reflecting axon content, it could be possible that mean MRW would become thinner in older eyes before a decrease is observed in RNFL thickness. Interestingly, mean MRW was significantly correlated with mean ALCSD in our young eyes, but not in older eyes (i.e., young eyes with more posteriorly-located ALCSs, or larger mean ALCSDs, also had thinner mean MRWs;Figure 3-10a). Given this result, it could also be possible that changes in prelaminar tissue during normal aging could result in a thinning of axonal and prelaminar tissue contributions to the MRW near the rim, but not in the peripapillary retina (located further from the rim) where RNFL thickness is measured.

If the process of normal aging increases the susceptibility of the ONH to glaucomatous damage, one might expect to see structural changes in the ONH and laminar microarchitecture in older eyes (relative to young eyes) that mimic changes seen in early glaucoma, but potentially to a lesser extent. Some of the structural changes that have been found to occur in early experimental glaucoma include an increase in mean ALCSD (i.e., posterior movement of the ALCS) (Strouthidis et al., 2011; Ivers et al., 2015), an increase in laminar thickness (Yang et al., 2007b; Roberts et al., 2009b; Yang et al., 2015), a decrease in mean MRW (He et al., 2014b; Gardiner et al., 2015; Ivers et al., 2015) and an increase in ALCS pore area (Yang et al., 2007b; Strouthidis et al.,

2011; Ivers et al., 2015). If ONH and laminar structure in the older eye mimic that found in the early glaucomatous eye (but to a lesser degree), one might expect older eyes to have slightly decreased mean MRWs and slightly increased laminar thicknesses, mean ALCSDs and ALCS pore areas compared to young eyes. As previously discussed, mean MRW was significantly thinner in our older normal eyes compared to young normal eyes (*P*=.02; Table 3-2). And, while it was not possible to measure lamina cribrosa thickness *in vivo* in this study, a previous study performed *ex vivo* in donor eyes has reported laminar thickness to be greater in normal, older eyes (Kotecha et al., 2006). However, mean ALCSD was found to not be significantly different in our older eyes (342.2 ± 82.48 µm) compared to young eyes (354.1 ± 83.73 µm; *P* = .70). Likewise, mean values of global ALCS pore area measured in our older eyes (1988 ± 559 μm^2) were not significantly different from mean values measured in young eyes (1999 ± 577 μm^2) (Table 3-2). These findings, coupled with those from other studies, show that some of the ONH and laminar structural parameters measured in older normal eyes have values that lie between those measured in young, normal eyes and in early glaucomatous eyes, potentially lending partial support to the idea that glaucoma contains an accelerated aging component.

In conclusion, ONH and mean global laminar pore parameters were similar between fellow eyes of normal subjects. Most parameters were also similar between young and older normal eyes. Consistent with previous studies, mean MRW was significantly thinner in older eyes than in young eyes, suggesting an age-related thinning in MRW. While the findings of this study can serve as normative data for prospective studies examining ONH structure and ALCS pore microarchitecture in patients with different forms of glaucoma, future work is needed to better understand the impact of normal aging and other risk factors for disease (such as race).

3.5 Acknowledgements

This work was supported by National Institutes of Health (NIH) Grants R01 EY021783 and P30 EY07551, and the University of Houston, College of Optometry. The authors thank Mindy Fox for help with data collection and Crawford Downs, Ronald Harwerth, Nimesh Patel and Michael Twa for helpful discussions. Danica Marrelli has served as a consultant with Alcon, Allergan, Merck, and Carl Zeiss Meditec.

CHAPTER 4

In vivo examination of lamina cribrosa microarchitecture and optic nerve head morphology between normal and glaucomatous eyes

Contributing authors:

Nripun Sredar, Danica J Marrelli, OD, Hope M. Queener and Jason Porter, PhD

Abstract

Purpose: Previous *in vivo* studies have separately compared lamina cribrosa microarchitecture or optic nerve head (ONH) geometry in normal and glaucomatous eyes. The main purpose of this study is to jointly examine ONH geometry and anterior lamina cribrosa surface (ALCS) microarchitecture between normal subjects, glaucoma suspects and patients with primary open-angle glaucoma (POAG).

Methods: Spectral domain optical coherence tomography (SDOCT) images of the ONH and adaptive optics scanning laser ophthalmoscope (AOSLO) images of ALCS microarchitecture were acquired in one eye of 28 subjects diagnosed as glaucoma suspects or with POAG (mean age = 66.1 ± 11.1 years) and 25 older normal human subjects (mean age = 57.5 ± 6.1 years). ONH parameters were calculated from manually marked SDOCT radial B-scans. Anterior laminar pores were manually marked in AOSLO images and 3D transformed to calculate mean global, central, peripheral and sectoral pore areas, elongation and nearest neighbor distance (NND). A Mann-Whitney rank sum test was used to assess statistical differences when comparing all parameters.

Results: Most ONH parameters (including mean ALCS curvature, prelaminar tissue volume, mean minimum rim width, rim volume and mean RNFL thickness) were significantly lower in suspect/POAG eyes compared to normal. Mean ALCS depth (ALCSD) was significantly larger (i.e., deeper) in suspect/POAG patients than in normals. Among ALCS pore parameters, only mean NND was shorter in suspect/POAG patients compared to normal. Sectoral pore analyses revealed significantly smaller pores in superior-temporal sectors of suspect/POAG eyes compared to normal eyes (P =.01). ALCS pore parameters were not correlated with ONH parameters for both suspect/POAG and older normal eyes.

Conclusions: Despite having statistically different ONH geometries, suspect/POAG and age-matched normal subjects had similar global ALCS pore microarchitecture. However,

when quantified on a local scale, significant differences in ALCS pore parameters were found between groups, stressing the importance for local analyses when examining and quantifying laminar microarchitecture.

4.1 Introduction

Glaucoma is a multifactorial disease that impacts multiple parts of the visual system, including retinal ganglion cells (Weber et al., 1998; Kerrigan-Baumrind et al., 2000), photoreceptors (Panda and Jonas, 1992; Choi et al., 2011), the lateral geniculate nucleus (Yucel et al., 2000; Gupta et al., 2009; Wang et al., 2016) and the visual cortex (Duncan et al., 2007; Borges et al., 2015). However, strong evidence suggests that damage to retinal ganglion cell axons at the level of lamina cribrosa within the optic nerve head (ONH) is central to glaucomatous pathophysiology (Quigley and Anderson, 1976b; Minckler et al., 1977; Quigley and Anderson, 1977). Studies involving animal models of experimental glaucoma, including monkeys (Burgoyne et al., 2004; Downs et al., 2007; Yang et al., 2010), rats (Johnson et al., 1996) and mice (Howell et al., 2007), have demonstrated that retinal ganglion cell axons and ONH structure undergo profound changes at early stages of the disease.

Several *ex vivo* studies have compared the structure of the lamina cribrosa and ONH between normal and glaucomatous eyes in human patients and between control and experimental glaucoma eyes in non-human primates. Previous work performed histologically in glaucomatous human eyes have revealed that multiple changes occur to the lamina cribrosa during disease (including a posterior deformation and eventual thinning of the entire laminar structure), as well as molecular changes in overlying astrocytes (Quigley and Green, 1979; Quigley et al., 1982; Hernandez, 2000; Jones et al., 2003). In addition, recent studies examining laminar microstructure have found differences in the preferred orientation of lamina cribrosa and peripapillary sclera collagen fibers between glaucoma and normal eyes (Jones et al., 2015). The collagen fibers of lamina cribrosa is substantially crimped and increased IOP could induce stretching and reduction of crimp (Sigal et al., 2013). Many of the aforementioned differences in ONH and laminar structure reported in human donor eyes have also been

observed in animal models of experimental glaucoma. For example, histological analyses performed in a non-human primate model of experimental glaucoma have similarly found that the laminar surface undergoes a posterior deformation (i.e., increase in mean anterior lamina cribrosa surface depth [ALCSD]) in early stages of glaucoma (Yang et al., 2007b). Additional changes include an overall thickening of the prelaminar tissue and lamina cribrosa (Yang et al., 2007b), an expansion of the scleral canal, a posterior "migration" of the entire lamina cribrosa (Yang et al., 2015) and an increase in connective tissue volume fraction relative to control eyes (Roberts et al., 2009b).

In vivo studies between normal and glaucomatous human eyes and between control and experimental glaucoma eyes have resulted in the development of optical coherence tomography (OCT)-derived ONH structural parameters to characterize changes associated with early glaucoma in humans. RNFL thickness has become a standard clinical metric used to aid in the diagnosis and assessment of progression of glaucoma (Bowd et al., 2001). More recently introduced parameters that have been shown to precede changes in RNFL thickness *in vivo* in longitudinal studies of non-human primate eyes with early experimental glaucoma include mean ALCSD and mean minimum rim width (MRW) (Strouthidis et al., 2011; Park et al., 2012a; He et al., 2014b; Ivers et al., 2015). In addition to these macroscopic changes in neuronal and laminar geometry, differences in lamina cribrosa microarchitecture have also been quantified *in vivo* between experimental glaucoma and fellow control eyes of non-human primates and between normal and glaucomatous human eyes. Ivers et al. examined changes in ALCS microarchitecture and ONH structural parameters in a non-human primate model of experimental glaucoma and found that ALCS pore areas tended to increase in eyes with early experimental glaucoma. A small number of published studies have also examined lamina cribrosa pore shape in living human eyes with glaucoma using swept-source OCT and adaptive optics (AO) systems (Akagi et al., 2012; Wang et al., 2013;

Zwillinger et al., 2016). However, despite all of these important studies, there is a lack of *in vivo* data that quantitatively describes laminar surface microarchitecture and its relationship with ONH geometry and retinal ganglion cell (RGC) axon density in human eyes with glaucoma.

The main purposes of this study were to (1) examine anterior lamina cribrosa surface (ALCS) microarchitecture and ONH geometry between glaucoma suspect/primary open angle glaucoma (POAG) patients and age-matched normal subjects and (2) determine whether relationships exist between ALCS pore and ONH parameters in suspect/POAG eyes. We cross-sectionally examined ALCS pore microarchitecture quantified from adaptive optics scanning laser ophthalmoscope (AOSLO) images and ONH geometry from spectral domain optical coherence tomography (SDOCT) images across suspect/POAG patients and older normal subjects. Statistical tests were performed to determine differences in ALCS pores and ONH parameters between suspect/POAG and normal eyes and investigate relationships between ONH and ALCS pore parameters. This study will provide a better understanding of whether differences exist in ALCS microarchitecture and ONH parameters between suspect/POAG eyes and older normal eyes and the degree to which these parameters interact with each other in normal and diseased eyes.

4.2 Methods

All human subjects research adhered to the tenets of the Declaration of Helsinki. The study protocol was approved by the University of Houston's Committee for the Protection of Human Subjects. Informed consent was obtained from each subject prior to the experiment. Twenty-eight patients who were glaucoma suspects or had early/moderate POAG (mean age = 66.1 ± 11.1 years; range = 41 - 85 years) and 25 older normal subjects (mean age = 57.5 ± 6.1 years; range = 50 - 76 years) were enrolled. 19 of our

subjects were White (non-Hispanic), 5 were Asian, 19 were African-American and 11 were Hispanic, with 29 males and 24 females. All subjects had spherical equivalent refractive errors between +3.00 D and -6.00 D (with cylinder ≤ ±3.00 D), best corrected visual acuities better than or equal to 20/40 and clear ocular media. Each subject underwent a comprehensive ophthalmic examination that included evaluation of the anterior segment and anterior segment angle (Von Herick test) using slit lamp biomicroscopy, measurement of intraocular pressure (IOP) (via Goldman Applanation Tonometry), dilated color stereoscopic optic disk photographs (Nidek AFC-230 Fundus Camera), reliable Humphrey visual fields (24–2 Swedish Interactive Threshold Algorithm standard program; False positive and False negative rates < 33%, Fixation losses < 20%) and measurement of central corneal thickness viaultrasound pachymetry (AccuPach, Accutome). One eye was selected and dilated for imaging using 1.0% tropicamide and 2.5% phenylephrine for each suspect/POAG patient and age-matched older subject in the study.

Subjects included in the suspect/POAG group included patients diagnosed with early or moderate stages of POAG and POAG suspects. All patients diagnosed with POAG had open anterior chamber angles, characteristic glaucomatous ONH and/or RNFL changes with corresponding visual field defects, no signs of secondary glaucoma and no additional pathology affecting ocular health. POAG suspects had suspicious ONH or RNFL appearance, or possessed known risk factors for glaucoma (e.g., elevated IOP, family history, age, race), but had received no clinical diagnosis of glaucoma. These suspects were also free from any other ocular pathologies. The suspect/POAG group has Humphrey visual field mean deviation (MD) average of -2.6 dB (range: 1.8dB to -10.8dB). The older normal group of subjects had no history of elevated IOP, no clinically abnormal disc or nerve fiber layer appearance, no visual field defect and were free from ocular pathologies.

4.2.1 *Spectral domain optical coherence tomography (SDOCT) imaging and analysis*

Wide-field scanning laser ophthalmoscope (SLO) fundus images and cross-sectional images of the ONH were acquired in each eye using the Heidelberg Spectralis HRA+OCT (Heidelberg Engineering). Cross sectional radial scans (48 B-scans, 20° field size, ART averaging of 16 frames) centered on the ONH were acquired with Enhanced Depth Imaging in all eyes (Figure 4-1a). The Inner Limiting Membrane (ILM) was automatically segmented in each B-scan using the SDOCT instrument's software and any inaccuracies were manually corrected. The raw '.vol' files of all radial scans were then exported from the SDOCT instrument and analyzed via a custom semi-automated program (MATLAB; The MathWorks, Inc., Natick, MA). The termination points of the retinal pigment epithelium (RPE)/Bruch's membrane (BM) interface and anterior lamina cribrosa surface were manually marked in as many B-scans as possible (Figure 4-1b). A 3-dimensional point cloud of marked and segmented points was subsequently generated (Figure 4-1c).

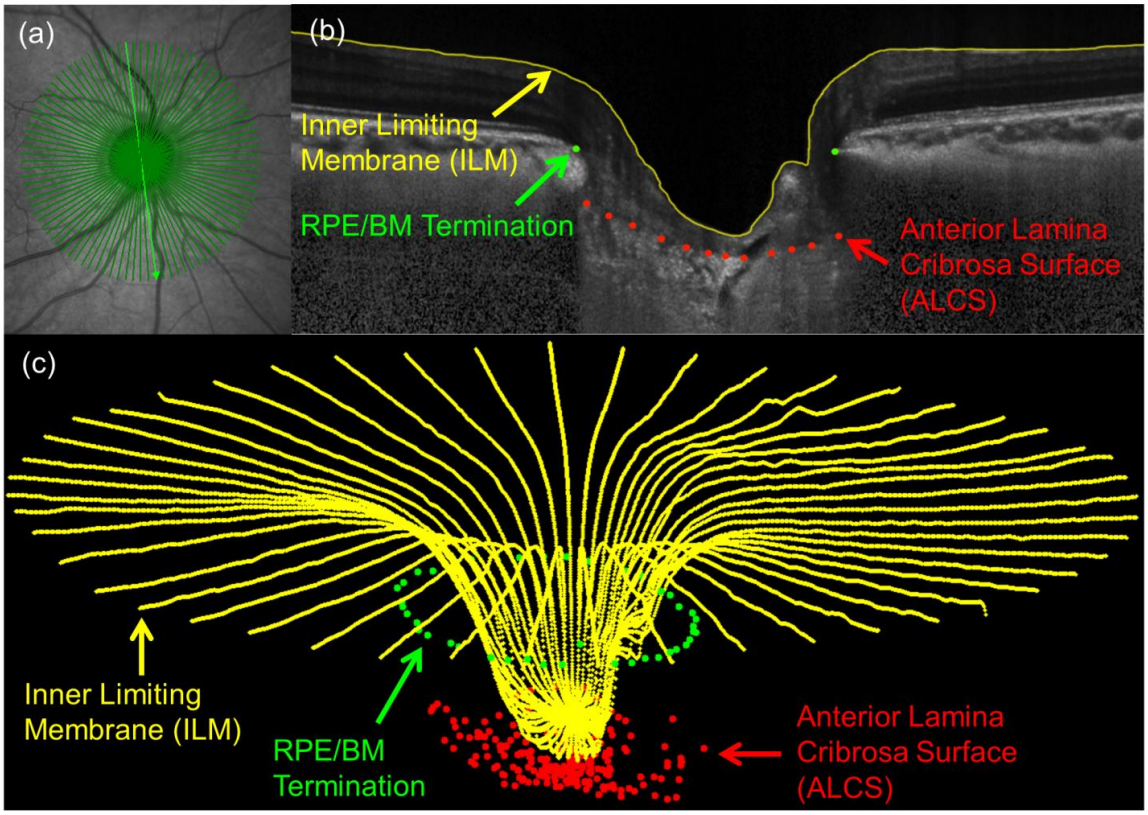

Figure 4-1. (a) Representative *en face* view of the ONH illustrating the locations of all 48 radial B-scans (green lines) acquired via SDOCT image using the EDI mode (16 frames averaged). (b) Single radial B-scan of the ONH corresponding to the scan location denoted by the bold green arrow in (a). Segmented and manually marked features included the ILM (yellow points), termination points of the RPE/Bruch's membrane (BM) complex (green points) and the anterior lamina cribrosa surface (red points). (c) 3-dimensional point cloud generated from landmarks delineated in each SDOCT radial B-scan from (a). (ILM in yellow, RPE/BM termination points representing Bruch's Membrane Opening [BMO] in green, and anterior lamina cribrosa surface [ALCS] in red).

The delineated landmarks were used to calculate several ONH parameters. In brief, BMO area was calculated as the area enclosed by an ellipse best-fit to the marked BMO points (Figure 4-2a). Mean anterior lamina cribrosa surface depth (ALCSD) was calculated as the mean distance between a plane best-fit to the marked BMO points and a thin-plate spline surface that was fit to the marked ALCS points to model the ALCS in 3 dimensions (Figure 4-2b) (Sredar et al., 2013). Because mean ALCSD only provides information on the mean position (depth) of the ALCS within the disc, we further characterized the ALCS by computing its mean radius of curvature (RoC) within the projection of the BMO ellipse (Figure 4-2c,d) (Sredar et al., 2013). The RoC at a particular location on the ALCS was calculated as the ratio of the change in arc length to the change in the angle of the tangent between two points immediately juxtaposing the location being examined on the 3D ALCS. Mean RoC was then computed as the average of all RoC values calculated at each point on the 3D interpolated ALCS.

Additional ONH structural parameters were also quantified after fitting a 3-dimensional thin plate spline to the ILM point cloud. Prelaminar tissue volume (PTV) was calculated as the volume between the ILM and anterior laminar surface that was contained within a hollow-cylinder extending from the edge of the BMO to the ALCS (Figure 4-3a) (Yang et al., 2007b; Strouthidis et al., 2011). Neuroretinal rim volume was calculated as the tissue volume anterior to the BMO plane that was bounded by the ILM surface and a vertical perpendicular projection from the edge of the BMO (Figure 4-3a) (Yang et al., 2007b; Strouthidis et al., 2011). Mean MRW, a potential surrogate marker of axonal density, was calculated as the mean of the minimum distances between the marked BMO points and the ILM surface across all radial B-scans (Figure 4-3b) (Strouthidis et al., 2011; Chauhan et al., 2013).

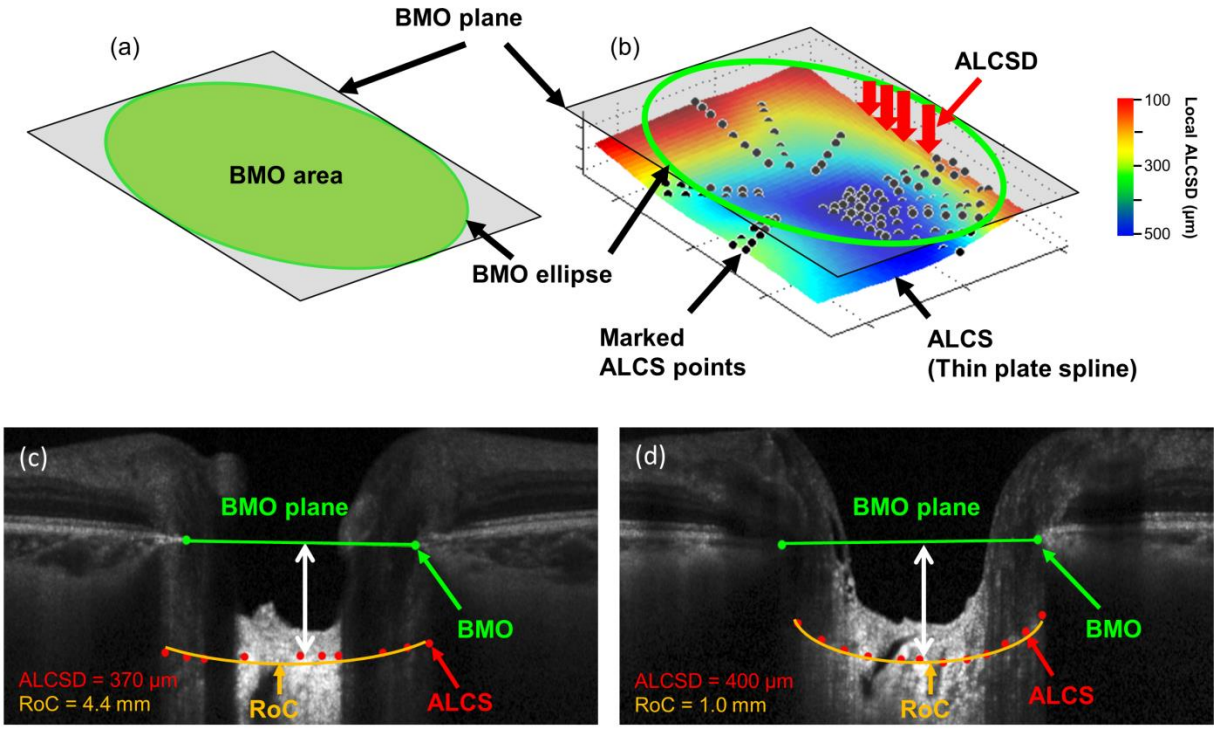

Figure 4-2. Calculation of BMO Area, Mean ALCSD and mean radius of curvature (RoC) of the ALCS. (a) An ellipse (bold, green line) was best-fit in 3-dimensions to the marked RPE/BM termination points and used to define a BMO plane. BMO area was calculated as the area enclosed by the BMO ellipse on the BMO plane (gray). (b) After fitting a thin plate spline to the marked ALCS points (black dots, above and below the fitted surface), mean anterior lamina cribrosa surface depth (ALCSD) was calculated as the mean of the perpendicular distances from the BMO plane to the thin plate spline (red arrows) for points within the BMO ellipse. The color scale used in illustrating the thin-plate spline surface represents the range of ALCSDs calculated across the laminar surface. Regions shaded in blue represent locations with increased mean ALCSD values (i.e., more posteriorly-located ALCS's within the ONH) while regions shaded in red represent locations with decreased mean ALCSD values (i.e., more anteriorly-located ALCS's). (c,d) The mean RoC of the ALCS (orange curve) was calculated by averaging the RoCs computed at every point on the ALCS and attempts to quantify the mean curvature of the ALCS. The shape of the ALCS can vary dramatically, even between eyes with similar values of mean ALCSD. For example, while the mean position of the ALCS from the BMO plane was similar values between 2 eyes (mean ALCSD = 370 µm in (c) and 400 µm in (d)), the ALCS was flatter (i.e., larger RoC, 4.4 mm) in (c) and steeper (i.e., smaller RoC, 1.0 mm) in (d).

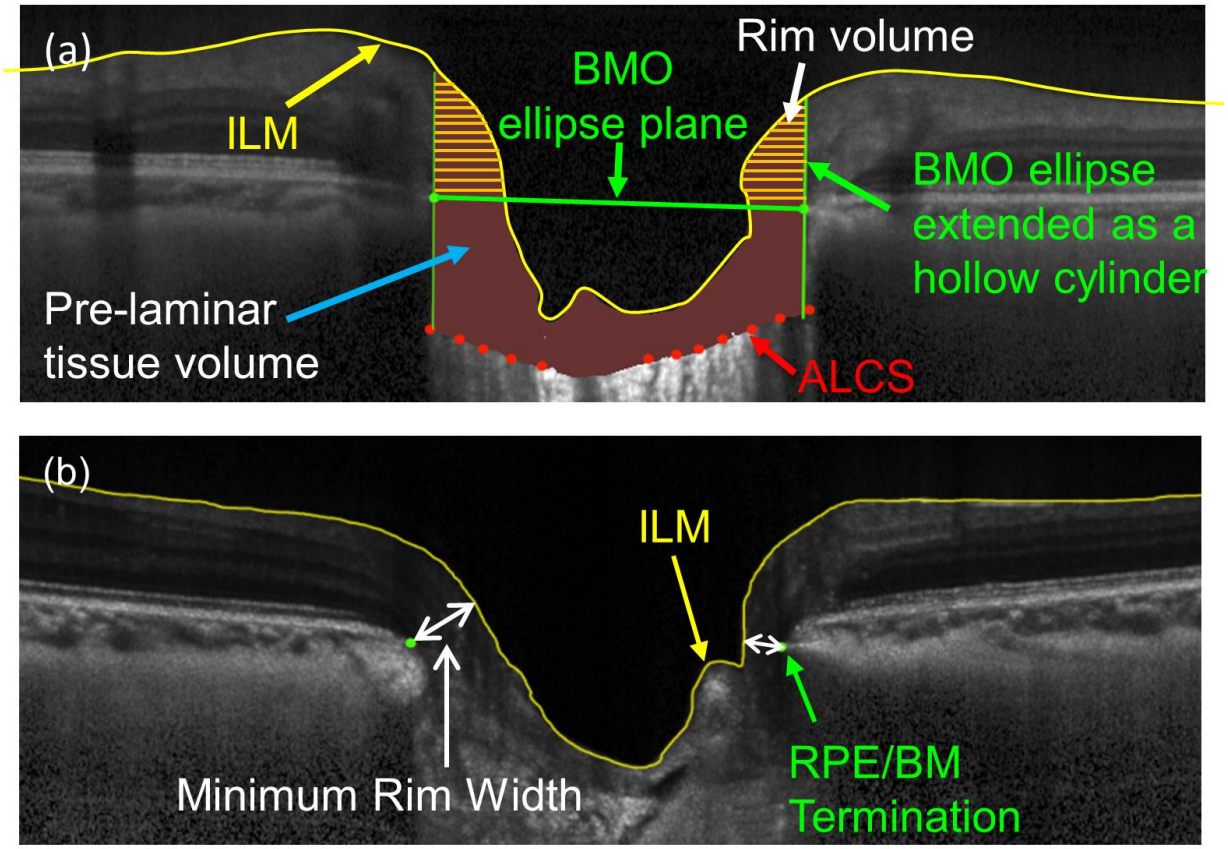

Figure 4-3. Illustration of prelaminar tissue volume (PTV), neuroretinal rim volume and mean minimum rim width (MRW). (a) The ILM (yellow line), RPE/BM termination point (green dots) and ALCS (red dots) were segmented/marked in each radial b-scan. In a single B-scan, prelaminar tissue area (brown region) was computed as the area between the ILM and ALCS that was contained within a hollow-cylinder defined by the BMO ellipse. To compute prelaminar tissue volume, thin plate spline surfaces were fit to the 3-dimensional ILM and ALCS point clouds and used to calculate the volume between these surfaces that was confined within a hollow-cylinder extending from the BMO ellipse. Neuroretinal rim volume (hatched region) was calculated as the volume between the ILM surface and BMO plane that was contained within a vertical perpendicular projection from the BMO ellipse. (b) Mean MRW was calculated by averaging the minimum distances measured between the ILM surface (yellow line) and termination points of the BM/RPE interface (green dots) on each side of the neural canal opening (white arrows) across all marked B-scans.

Additionally, a 10° x 30° volume scan (49 B-scans, ART averaging of 16 frames) was acquired over an area encompassing both the ONH and fovea and used to calculate the Fovea-BMO (FoBMO) axis, or axis that connected the center of the foveal pit with the center of the BMO, in order to divide the ONH into sectors in each eye (Figure 4-4) (He et al., 2014a). A custom MATLAB program was used to determine the location of the foveal pit center from the acquired volume scan. After inspection and correction of any inaccuracies in segmentation of each B-scan in the volume, the ILM and RPE segmentation were imported from Heidelberg Spectralis HRA+OCT and used to calculate a total retinal thickness profile for each B-scan (Figure 4-4a) (McAllister et al., 2010). A 3D retinal thickness map was then generated form the retinal thickness profiles of all B-scans throughout the macular region. Five ellipses where each individually fit to points within the foveal pit that contained equal retinal thickness values that ranged between 5% to 50% of the maximum foveal pit depth (Figure 4-4b). The center of the foveal pit was calculated as the average location of all centroid positions from each fitted ellipse. The retinal thickness map and the location of the foveal pit center were then registered and overlaid on the SLO image obtained during the acquisition of the SDOCT volume scan (Figure 4-4c). This SLO image was then registered with the SLO image obtained during the acquisition of the aforementioned radial scans of the ONH (which contained the BMO ellipse) using a Dual Bootstrap algorithm (Yang et al., 2007a) and a custom MATLAB program to generate a single, combined SLO image that contained the location of the foveal pit center and the BMO ellipse (Figure 4-4c). The FoBMO axis was constructed as a line connecting the foveal pit center and the center of the BMO ellipse, and used as a reference to divide the ONH into sectors. The ONH was divided in half by constructing a line that was perpendicular to the FoBMO axis and passed through the center of the BMO ellipse. The temporal half of the ONH was then divided into three equal sectors (of 60°) in the namely superior-

temporal, temporal and inferior-temporal regions. Furthermore, the BMO was divided into central and peripheral zones of equal areas. Both sectors and zones were used to quantify ALCS pore microarchitecture on a local scale.

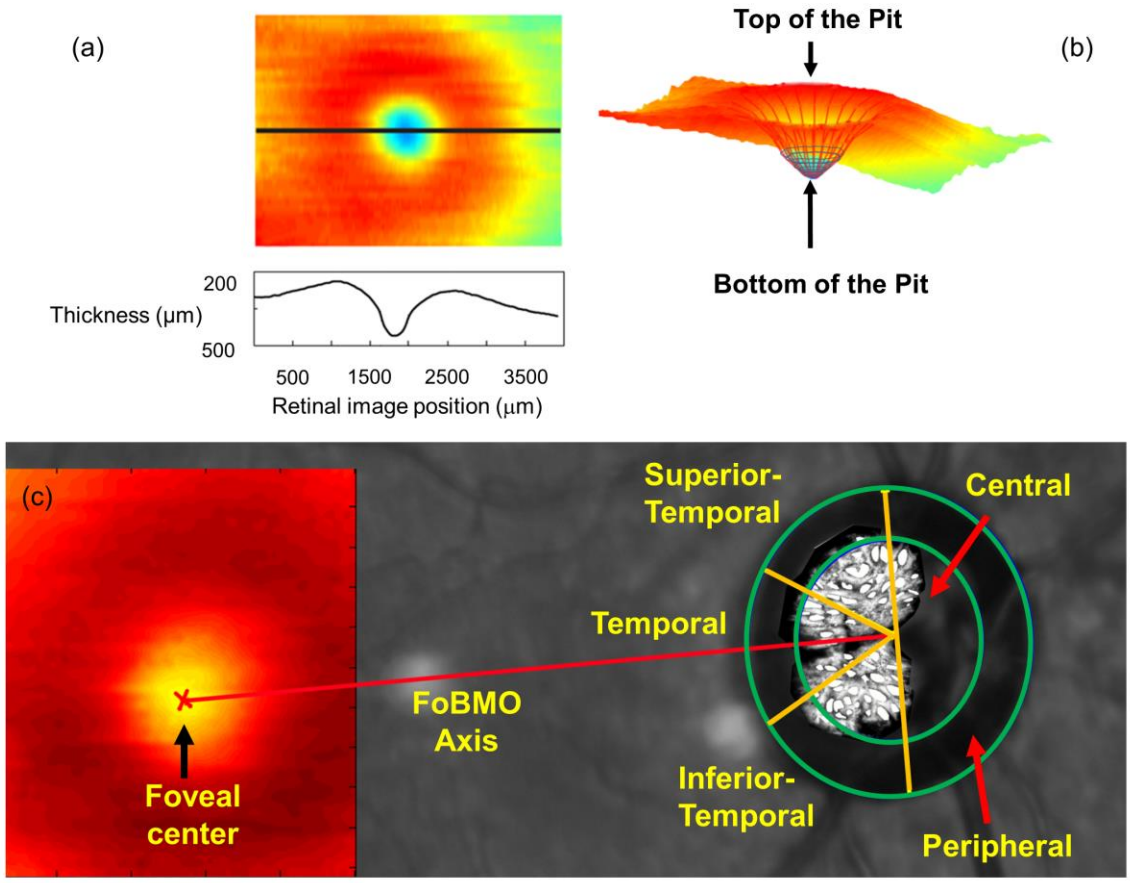

Figure 4-4. Description of the method used to calculate the FoBMO axis, or axis connecting the foveal center to the center of the BMO, for dividing the ONH into sectors and regions. (a) *En face* view of a macular retinal thickness map (i.e., thickness between the ILM and RPE) interpolated from B-scans acquired throughout the foveal region. Retinal locations that are thicker are denoted in red and locations that are thinner are denoted in blue. The cross-sectional retinal thickness profile along the black scan line illustrated in the *en face* map (top) is plotted immediately below as a function of retinal position. (b) A 3D representation of the retinal thickness map in (a) in which ellipses (blue) were best-fit to points of equal retinal thickness. The center of the foveal pit was calculated as the location corresponding to the average of all centroid positions from each fitted ellipse. (c) A retinal thickness map covering the foveal region (lower left) and an adaptive optics image of the ALCS microarchitecture inside the ONH (in which pores are marked in white) were registered and overlaid on a Spectralis SLO image of the foveal and ONH regions (background). The red line connecting the foveal center (red cross) to the center of the BMO ellipse (outermost green ellipse sorrounding the ONH) is

the FoBMO axis and is used to divide the ONH into 60° sectors (denoted by orange lines). A line that passes though the center of the BMO and is perpendicular to the FoBMO axis (long orange line oriented in the superior/inferior direction) divides the BMO into temporal and nasal halves. The temporal half of the BMO is then divided in 60° sectors in the superior-temporal, temporal, and inferior-temporal directions. The BMO was also divided into central and peripheral regions of equal area (shown by the second green ellipse).

4.2.2 Adaptive optics imaging of ALCS microarchitecture

Adaptive optics was used to correct each subject's optical aberrations over a dilated pupil (~8 mm) (Li et al., 2010). The ALCS microarchitecture was subsequently imaged in reflectance using an 840 nm wavelength superluminescent diode (S-Series Broadlighter, Superlum, Carringtwohill, Ireland) (Ivers et al., 2010; Ivers et al., 2011; Sredar et al., 2013) with a laser power of approximately 250 μW at the pupil plane (less than ~10 times below the ANSI standards for safe light delivery to the eye) (ANSI, 2014). Videos were captured at 25 Hz over a 1.5° field. Through-focus images of the lamina were acquired at different depths to determine the plane of best-focus of the ALCS microarchitecture, or the location where ALCS pore boundaries first became sharpest and the image had optimal contrast. Videos of the ALCS microarchitecture were then acquired throughout as much of the ONH as possible. AOSLO videos were subsequently post-processed off-line using a custom program (MATLAB; The MathWorks, Inc., Natick, MA) to remove eye motion and create registered images that were then stitched together to create a montage of the anterior laminar surface beams and pores (Adobe Photoshop; Adobe Systems, San Jose, CA) for each eye (Figure 4-5b). The image contrast of each AOSLO montage was improved using a contrast limiting adaptive histogram equalization (CLAHE) technique (ImageJ; developed by Wayne Rasband, National Institutes of Health, Bethesda, MD; available at http://rsb.info.nih.gov/ij/index.html).

Pore boundaries were manually marked (Adobe Photoshop) in as many locations as possible using previously described methods found to have excellent repeatability and reproducibility (Figure 4-5c) (Sredar et al., 2013; Ivers et al., 2015). Because the *en face* AOSLO images represent a 2-D projection of a 3D laminar surface, we transformed our 2D images into their approximate 3D morphology by registering and projecting the 2D AOSLO image onto the interpolated thin-plate spline surface that was best-fit to the

ALCS points marked in the SDOCT radial B-scans (Figure 4-5d,e) (Sredar et al., 2013). Following 3D transformation, we quantified the area, elongation (ratio of the major to minor axis of an ellipse best-fit to each pore boundary), and nearest neighbor distance (NND, nearest distance from the centroid of a given pore to those of its neighbors) of each marked pore using a custom MATLAB program (Ivers et al., 2011; Ivers et al., 2015). All marked and quantified pores were then analyzed globally, regionally (centrally vs. peripherally) and in 60° sectors on the temporal half of the disc for each suspect/POAG eye and normal eye. Pore parameters were then compared on global and local spatial scales between suspect/POAG and normal eyes.

4.2.3 Biometric measurements and image scaling

Biometric measurements of axial length, anterior chamber depth and anterior corneal curvature were acquired using the IOL Master (Carl Zeiss Meditec) or LenStar LS 900 (Haag-Streit). These biometric parameters were used to laterally scale field sizes in AOSLO and SDOCT images from visual angle (in degrees) to physical retinal size (in micrometers). Conversions were performed by incorporating these biometry measurement data into a 4-surface model eye (Li et al., 2010; Ivers et al., 2011).

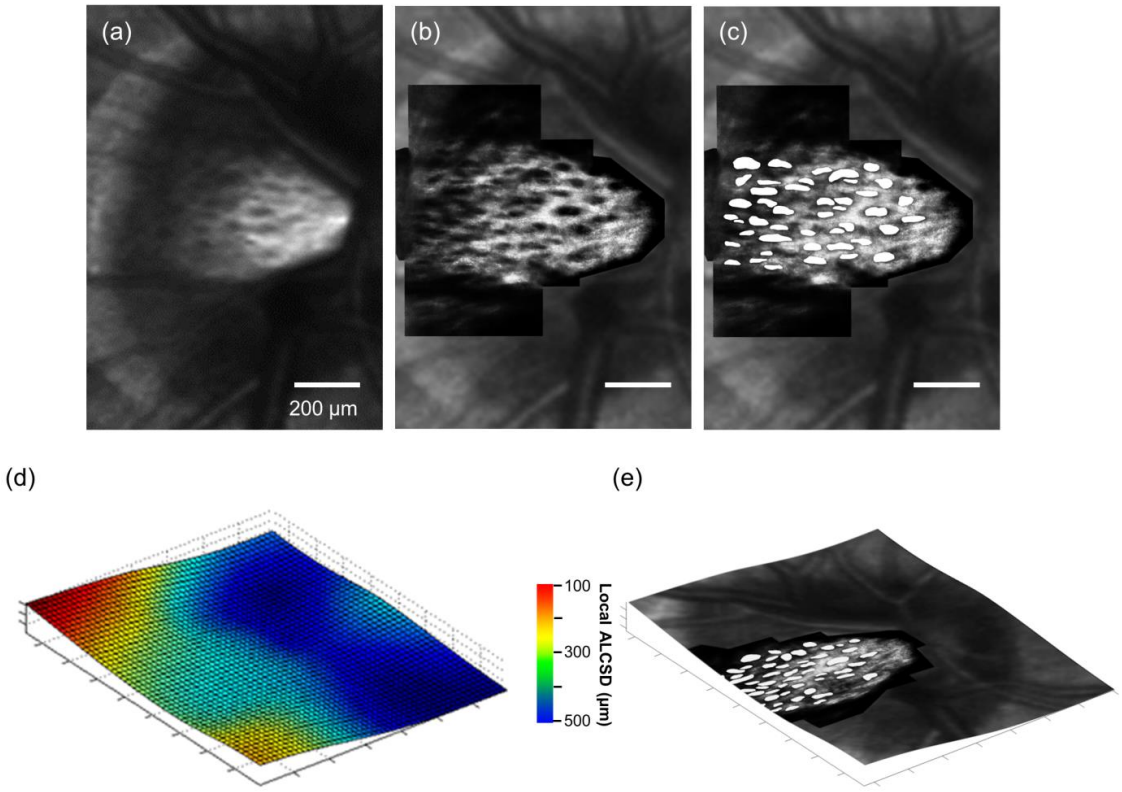

Figure 4-5. Adaptive optics imaging of the lamina cribrosa in a normal human eye. (a) Spectralis SLO image of the ONH when best focused on the anterior lamina cribrosa surface (ALCS). (b) A 2 dimensional AOSLO montage of the ALCS microarchitecture overlaid on the same Spectralis SLO image as in (a). The resolution and contrast of laminar beams and pores improved with adaptive optics correction. Scale bar: 200 µm. (c) Same image as in (b) in which laminar pores were manually marked (white) throughout as much of the imaged area as possible. Scale bar: 200 µm. (d) An interpolated thin plate spline surface was fit to the ALCS points manually marked in SDOCT radial B-scan images acquired in the same eye (see Figure 4-1b for an explanation of marking). The depth of the ALCS at each point on the thin-plate spline surface (local ALCSD) is color-coded using the scale on the right side of the image, with more posteriorly-located surface points represented in blue and more anteriorly-located surface points represented in red. (e) 3D AOSLO montage constructed by registering and projecting the 2D AOSLO image from (c) onto the thin plate spline surface from (d). All pore values were quantified from the 3D transformed images.

4.2.4 Visual Field and Structure-Function Analyses

We examined whether differences existed between superior and inferior visual field sensitivities across eyes (e.g., within or between normal and suspect/POAG groups) and within individual eyes. A mean sensitivity value from all tested points in the superior half of the visual field and a mean sensitivity value from all tested points in the inferior visual field of each subject was first calculated. The mean superior visual field sensitivities were then compared to the mean inferior visual field sensitivities across all older eyes and across all suspect/POAG eyes. Mean superior and inferior visual field sensitivities were also compared between older normal eyes and suspect/POAG eyes, as well as within individual suspect/POAG eyes. In addition, the possible existence of gross structure-function relationships was investigated to determine whether any measured local differences in ALCS pores (e.g., superior-temporal sector vs inferior-temporal sector) corresponded to any measured differences in mean visual field sensitivity (e.g., superior vs. inferior halves of the visual field) between older normal eyes and suspect/POAG eyes, as well as within and across suspect/POAG eyes.

4.2.5 Data and Statistical Analyses

All statistical tests were performed using commercially available software (SigmaPlot; Systat Software Inc., San Jose, CA). A non-parametric Mann-Whitney Rank sum test was used to assess whether statistically significant differences existed in mean ONH and global ALCS pore parameters between (1) all suspect/POAG eyes and all age-matched normal subjects, (2) suspect/early POAG eyes with MDs < -3 dB and all normal eyes and (3) suspect/early POAG eyes with MDs < -3 dB and POAG eyes with MDs > -3 dB. A Mann-Whitney test was also used to (1) compare mean pore areas across sectors and within central and peripheral zones between suspect/POAG and normal eyes and (2) determine whether pore areas were statistically different between sectors within older

normal eyes, or within suspect/POAG eyes. Linear regression analyses were performed between ONH and global ALCS pore parameters to determine whether relationships existed between suspect/POAG eyes and age matched normal eyes. Statistically significant differences between superior and inferior field sensitivities within older normal eyes or within suspect/POAG eyes were assess using a paired t-test, while differences in mean superior (or inferior) visual field sensitivities between normal and suspect/POAG eyes were assessed using a Mann-Whitney test. A paired t-test was used to determine whether there was a statistically significant difference between field points measured in the superior visual field of a single subject compared to the sensitivities measured at all field points with corresponding eccentricity in the inferior visual field within each individual subject. (For example, [3° superior, 3° temporal] was paired with [3° inferior, 3° temporal]; [3° superior, 9° temporal] was paired with [3° inferior, 9° temporal]; etc.) *P* values < .05 were taken to represent a statistically significant difference for the parameters analyzed.

4.3 Results

4.3.1 Comparison of ONH structure and ALCS microarchitecture between suspect/POAG and normal subjects

The majority of ONH and ALCS pore parameters were significantly different between suspect/POAG eyes and age-matched normal subjects (Table 4-1). Figure 4-6 shows representative images of ALCS pore microarchitecture (with marked pores) and corresponding ONH structure from older, normal eyes and suspect/POAG eyes. The only examined ONH parameter that was not significantly different between normal and suspect/POAG eyes was BMO area (older normal eyes = 2.084 ± 0.52 vs. suspect/POAG eyes = 2.208 ± 0.54; *P*=.44) (Table 4-1). Compared to older normal eyes, suspect/POAG eyes had more posteriorly located ALCSs (larger mean ALCSDs) that

were more steeply curved (smaller mean RoCs). Suspect/POAG eyes also had less prelaminar tissue (smaller prelaminar tissue volumes), smaller neuroretinal rim volumes and less axonal content (smaller values of mean MRW and RNFL thickness).

When examining ALCS pore geometry on a global scale (Table 4-1), more pores were consistently imaged and marked in suspect/POAG eyes (56.2 ± 23.0) compared to older normal eyes (32.2 ± 19.3, P<.01). While mean global ALCS pore area was lower in suspect/POAG eyes than in age-matched normal eyes (1704 ± 429 μm^2 vs 1988 ± 559 μm^2, respectively), there was no statistically significant difference in this parameter between groups (P=.07). Mean global ALCS pore elongation was similar (P = .13) between suspect/POAG and normal eyes, whereas mean global ALCS pore NND was significantly smaller (P <.01) in suspect/POAG eyes than in normal eyes.

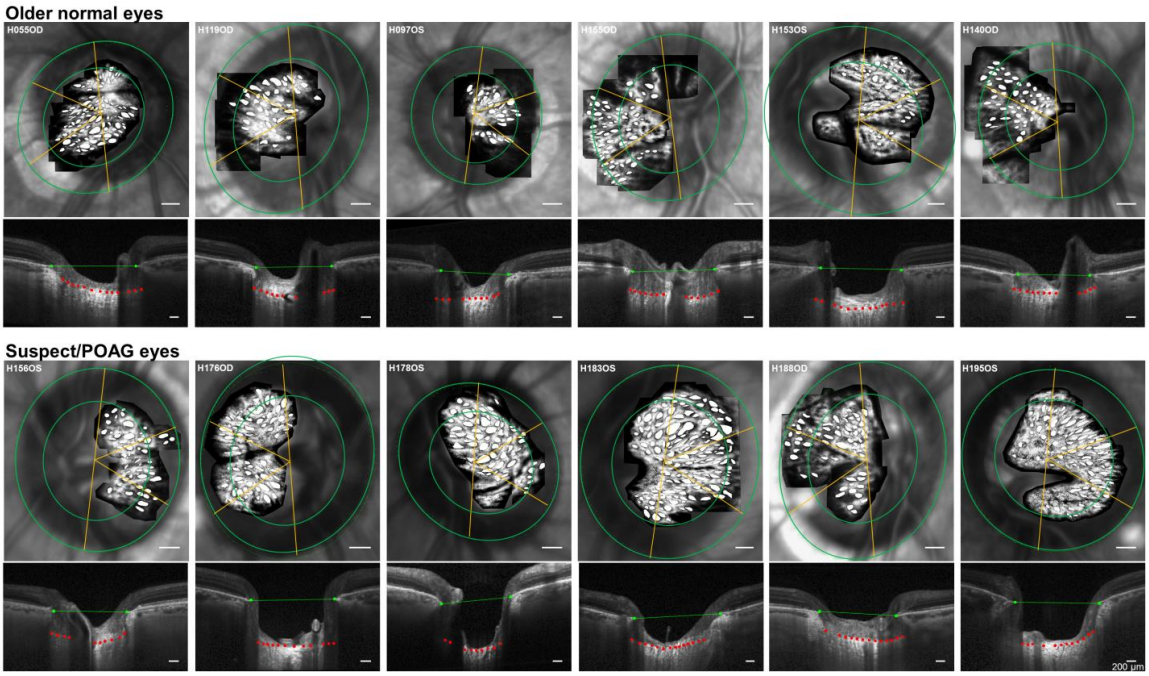

Figure 4-6. AOSLO montages of the ALCS microarchitecture overlaid on SLO images (rows 1 and 3) and corresponding SDOCT cross-sectional B-scans of the ONH (rows 2 and 4) acquired in six representative normal older eyes (rows 1 and 2) and six representative suspect/POAG eyes (rows 3 and 4). (Subjects H156, H176, H188, H195 were glaucoma suspects while subjects H178, H183were diagnosed with POAG.) In AOSLO images, laminar pores are filled in white. The outermost green ellipse on each SLO image represents the BMO ellipse, while the innermost ellipse in each image separates the central and peripheral zones of equal area. Yellow lines show the 3 sectors made on the temporal half of the ONH, namely the superior-temporal, tempopral, inferior-temporal sectors.The termination points of the BM/RPE interface (green dots) and the anterior laminar surface points (red dots) are marked on each SDOCT image. Scale bar (all images): 200 µm.

Table 4-1: Comparison of ONH and ALCS pore parameters between normal eyes and suspects/POAG eyes.

	Older Normal Eyes 25 eyes Mean age: 57.5 ± 6.1 years **Mean ± SD**	Suspect/POAG Eyes 28 eyes Mean age: 66.1 ± 11.1 years **Mean ± SD**	Mann-Whitney (*P-value*)
BMO Area (mm^2)	2.084 ± 0.519	2.208 ± 0.537	.44
Mean ALCSD (µm)	342.2 ± 82.5	439.2 ± 114.6	<.01*
Mean RoC (mm)	3.96 ± 1.25	2.78 ± 0.75	<.01*
Prelaminar tissue volume (mm^3)	0.977 ± 0.184	0.868 ± 0.187	.03*
Rim volume (mm^3)	0.412 ± 0.119	0.229 ± 0.092	<.01*
Mean MRW (µm)	287.1 ± 35.7	203.0 ± 41.8	<.01*
Mean RNFL Thickness (µm)	98.28 ± 6.00	80.14 ± 12.6	<.01*
Mean global pore area (μm^2)	1988 ± 559	1704 ± 429	.07
Mean global pore elongation	2.03 ± 0.24	2.10 ± 0.23	.13
Mean global pore NND (µm)	74.9 ± 18.2	64.2 ± 7.1	<.01*
Number of marked pores	32.2 ± 19.3	56.2 ± 23.0	<.01*

***** Statistically significant difference between older normal and suspect/POAG eyes (*P*<.05)

Analyses of ONH geometry and ALCS mircoarchitecture were also carried out between normal eyes and sub-groups of our suspect/POAG eyes. Table 4-2 shows a comparison of ONH and ALCS pore parameters between age-matched normal eyes and only those suspect/POAG eyes that had mean deviations (MDs) upon Humphrey visual field (HVF) examination of <-3.00 dB (18 of 28 suspect/POAG eyes). The majority of ONH parameters were statistically different between normal eyes and suspect/POAG eyes with MDs < -3 dB. Similar to the aforementioned results that included all suspect/POAG eyes, BMO area was similar between groups while suspect/POAG eyes with MDs < -3 dB also possessed more posteriorly-located ALCSs (larger mean ALCSDs) that were more steeply curved (smaller RoCs). Despite the fact that prelaminar tissue volume was similar between groups, suspect/POAG eyes with MDs < -3 dB still had smaller rim volumes and thinner MRWs and RNFLs compared to normal eyes. In addition, more pores were typically marked in suspect/POAG eyes with MDs < -3 dB than in normal eyes. The mean spacing between ALCS pores (mean global ALCS pore NND) was smaller in suspect/POAG eyes with MDs < -3 dB than in control eyes (P=.03). While there was a trend for suspect/POAG eyes with MDs < -3 dB to have smaller pores (smaller pore areas) that were more elliptical shaped (larger pore elongations) compared to normal eyes, the differences in mean global pore area (P=.08) and elongation (P=.06) were not significantly different between groups.

Table 4-3 compares ONH structural and ALCS microarchitecture parameters between 18 suspect/POAG eyes with MDs < -3 dB and 10 POAG eyes with MDs > -3 dB (or MDs worse than -3 dB). With the exception of prelaminar tissue volume, all ONH and mean global ALCS pore parameters were not statistically different between groups. POAG eyes with MDs > -3 dB had less prelaminar tissue (or smaller prelaminar tissue volumes) than suspect/POAG eyes with MDs < -3 dB (P=.04).

Table 4-2: Comparison of ONH and ALCS pore parameters between normal eyes and suspect/ POAG eyes who had mean deviations < -3 dB from Humphrey visual fields (HVF).

	Older Normal Eyes 25 eyes Mean age: 57.5 ± 6.1 years	Suspect/POAG Eyes (HVF MD <-3 dB) 18 eyes Mean age: 64.3 ± 8.8 years	Mann-Whitney (*P-value*)
	Mean ± SD	**Mean ± SD**	
BMO Area (mm^2)	2.084 ± 0.519	2.269 ± 0.530	.31
Mean ALCSD (µm)	342.2 ± 82.5	449.1 ± 107.8	<.01*
Mean RoC (mm)	3.96 ± 1.25	2.82 ± 0.79	<.01*
Prelaminar tissue volume (mm^3)	0.977 ± 0.184	0.922 ± 0.177	.27
Rim Volume (mm^3)	0.412 ± 0.119	0.239 ± 0.101	<.01*
Mean MRW (µm)	287.1 ± 35.6	209.1 ± 48.1	<.01*
Mean RNFL Thickness (µm)	98.3 ± 6.0	82.5 ± 12.9	<.01*
Mean global pore area (μm^2)	1988 ± 559	1677 ± 391	.08
Mean global pore elongation	2.03 ± 0.24	2.14 ± 0.23	.06
Mean global pore NND (µm)	74.9 ± 18.2	64.9 ± 7.9	.03*
Number of marked pores	32.2 ± 19.3	54.3 ± 19.1	<.01*

***** Statistically significant difference between older normal and suspect/early POAG eyes (*P*<.05)

Table 4-3: Comparison of ONH and ALCS pore parameters between suspect/ POAG eyes with MDs < -3 dB and POAG eyes with MDs > -3 dB (worse than -3 dB).

	Suspect/POAG Eyes (HVF MD <-3 dB) 18 eyes Mean age: 64.3 ± 8.8 years	POAG Eyes (HVF MD >-3 dB) 10 eyes Mean age: 69.4 ± 14.4 years	Mann-Whitney (*P-value*)
	Mean ± SD	**Mean ± SD**	
BMO Area (mm^2)	2.269 ± 0.530	2.097 ± 0.559	.30
Mean ALCSD (µm)	449.1 ± 107.8	421.3 ± 130.1	.52
Mean RoC (mm)	2.82 ± 0.79	2.70 ± 0.70	.87
Prelaminar tissue volume (mm^3)	0.922 ± 0.177	0.769 ± 0.170	.04*
Rim Volume (mm^3)	0.239 ± 0.101	0.212 ± 0.076	.43
Mean MRW (µm)	209.1 ± 48.1	192.1 ± 25.9	.35
Mean RNFL Thickness (µm)	82.5 ± 12.9	75.9 ± 11.2	.15
Mean global pore area (μm^2)	1677 ± 391	1752 ± 509	.91
Mean global pore elongation	2.14 ± 0.23	2.05 ± 0.22	.24
Mean global pore NND (µm)	64.9 ± 7.9	62.8 ± 5.3	.55
Number of marked pores	54.3 ± 19.1	59.6 ± 29.5	1.0

***** Statistically significant difference between suspect/early POAG and moderate POAG eyes (*P*<.05)

ALCS pore parameters were also quantified on a local level. A comparison of ALCS pore areas between age-matched normal eyes and suspect/POAG eyes within sectors and central/peripheral zones is show in Table 4-4. No significant differences were found in mean pore area between any sectors or between central and peripheral zones within normal eyes (P>.05) or within suspect/POAG eyes (P>.05). Across groups, mean ALCS pore area was significantly smaller in suspect/POAG eyes (1691± 623 μm^2) compared to normal eyes (2177 ± 651 μm^2) in the superior-temporal sector (*P*=.01). However, there were no statistical differences in mean ALCS pore area between older normal eyes and suspect/POAG eyes for the temporal and inferior-temporal sectors, as well as for central and peripheral zones.

Table 4-4: Comparison of ALCS pore area between normal eyes and suspect/POAG eyes by sector and central and peripheral zones. (n = number of eyes)

Mean ALCS pore area (μm^2)	Older Normal Eyes	Suspect/POAG Eyes	Mann-Whitney (*P* values)
Superior-Temporal	2177 ± 651 (n = 22)	1691 ± 623 (n = 26)	.01*
Temporal	1868 ± 623 (n = 23)	1708 ± 470 (n = 26)	.48
Inferior-Temporal	1913 ± 588 (n = 14)	1789 ± 581 (n = 26)	.47
Central zone	1966 ± 623 (n = 24)	1707 ± 454 (n = 26)	.17
Peripheral zone	2121 ± 611 (n = 13)	1727 ± 580 (n = 17)	.10

***** Statistically significant difference between older normal and suspect/POAG eyes (*P*<.05)

4.3.2 Examining relationships between ONH structure and ALCS microarchitecture

We investigated the degree of correlation between all examined ONH parameters for our older normal eyes and our suspect/POAG eyes. No significant relationships were calculated between the majority of ONH parameters. Figure 4-7 illustrates some of the comparisons that were examined between ONH parameters. We found no significant relationships between mean MRW and mean ALCSD (Figure 4-7a) or between mean RoC and mean ALCSD (Figure 4-7b) in normal or suspect/POAG eyes. Mean MRW was significantly correlated with mean RNFL thickness for the suspect/POAG eyes (Figure 4-7c), indicating that suspect/POAG eyes with thinner mean MRWs also tended to have thinner RNFLs. However, the same relationship was not observed in our older normal eyes. Mean MRW was also not related to mean RoC for either older normal eyes or suspect/POAG eyes (Figure 4-7d).

The degree of correlation between all global ALCS pore parameters was also examined for older normal eyes and suspect/POAG eyes. There was a significant increase in mean global ALCS pore NND with increasing mean global ALCS pore area in both groups of eyes (Figure 4-8a), indicating that eyes with larger pore areas also contained pores that were further separated from each other. However, mean global ALCS pore elongation was found to be independent of mean global ALCS pore area (Figure 4-8b), suggesting that the overall shape of the pores in a given eye was not related to their overall size.

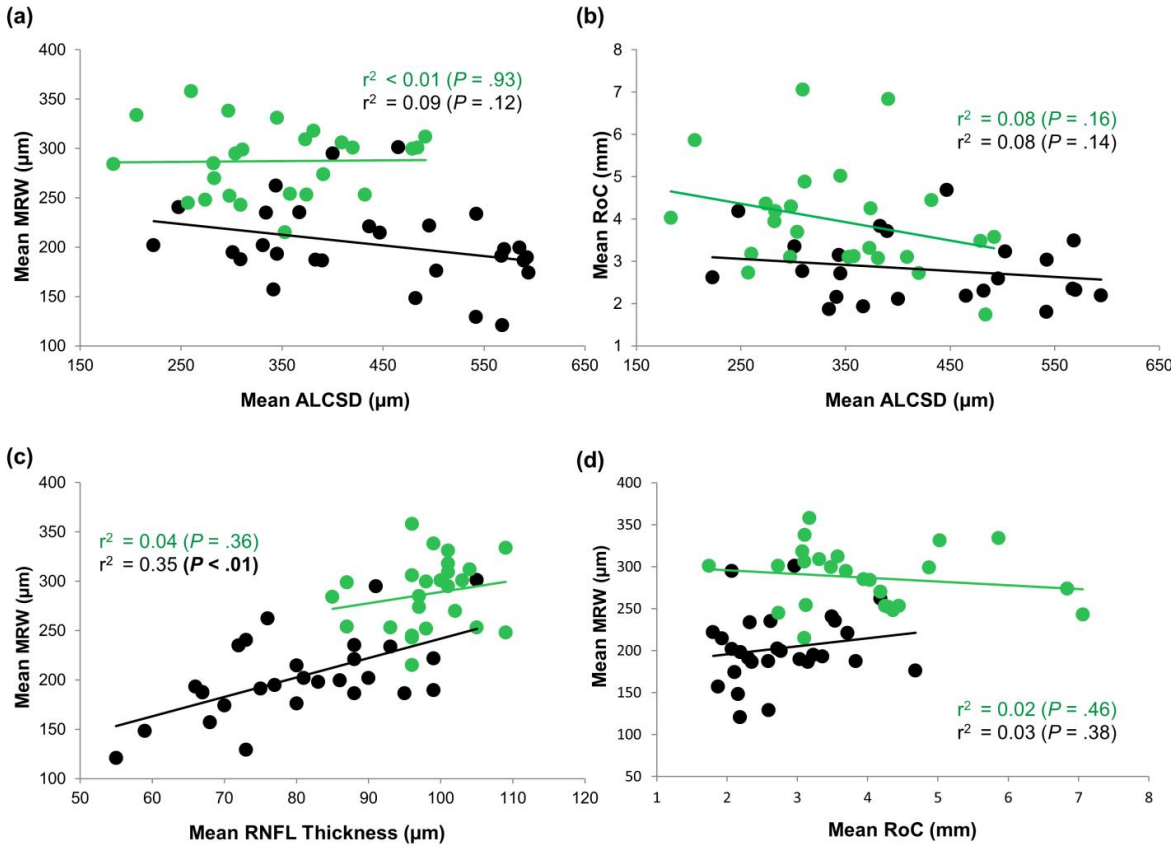

Figure 4-7. Comparison of ONH parameters for older, normal eyes (green filled circles) and suspect/POAG eyes (black filled circles). Solid lines indicate linear regressions fit to the corresponding data points. No statistically significant relationships were found between (a) mean MRW and mean ALCSD or between (b) mean RoC and mean ALCSD within our older, normal eyes or suspect/POAG eyes. (c) There was a statistically significant relationship between mean MRW and RNFL thickness in suspect/POAG eyes, as eyes with larger values of mean MRW tended to also have larger values of RNFL thickness. However, no relationship was observed between these parameters in older, normal eyes. (d) No significant correlation was measured between mean MRW and mean RoC for either group.

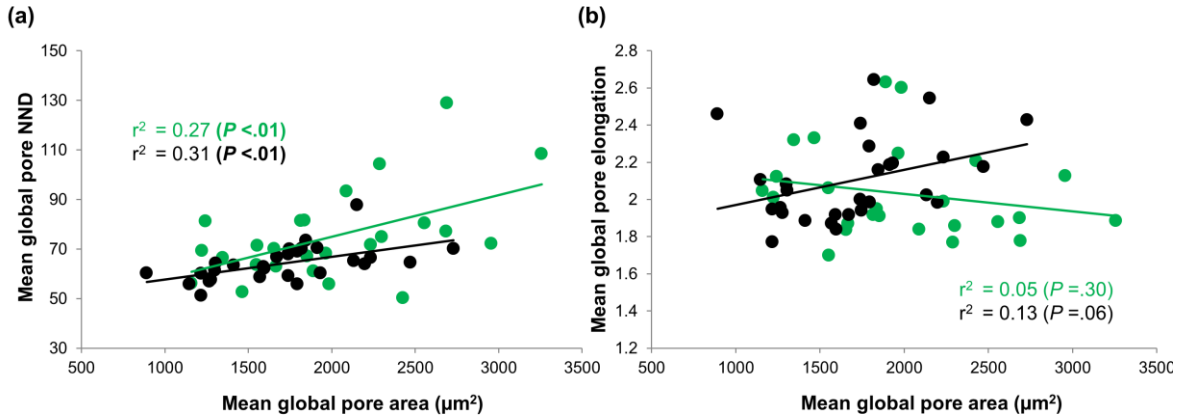

Figure 4-8. Comparison of global ALCS pore parameters for older, normal eyes (green filled circles) and suspect/POAG eyes (black filled circles). Solid lines indicate linear regressions fit to the corresponding data points. (a) There was a signficant relationship between mean global pore NND and more global pore area for both groups, as eyes with increased pore areas also tended to have increased NND spacing. (b) However, mean global pore elongation was not significantly correlated with mean global pore area for older, normal eyes or suspect/POAG eyes.

We also investigated the degrees of relationships between ONH and ALCS pore parameters for older normal eyes and suspect/POAG eyes, some of which are illustrated in Figure 4-9. No significant correlations were found between global or local measures of mean ALCS pore area and mean ALCSD (Figure 4-9a,b) within normal or suspect/POAG eyes, indicating that the area of ALCS pores was independent of the depth of the ALCS regardless of whether pores were considered globally, by sector or by central/peripheral zones. The mean shape of the ALCS pores (mean global pore elongation) was also not significantly correlated with the average position of the ACLS within the ONH (mean ALCSD) for both groups (Figure 4-9c). In addition, mean global pore area does was not significantly related with mean MRW for older normal and suspect/POAG eyes (Figure 4-9d).

We were also interested to examine whether any overall trends existed between ALCS pore and ONH parameters when considering all young normal eyes (reported in Chapter 3), all older normal eyes and all suspect/POAG eyes in aggregate. No significant relationships were found between mean global ALCS pore area and mean MRW or between mean global ALCS pore area and mean ALCSD (Figure 4-10a,b) after combining all eyes together. However, mean MRW significantly correlated with mean ALCSD across all eyes (Figure 4-10c), indicating that eyes with more posteriorly-located ALCSs (larger mean ALCSDs) tended to have thinner MRWs (smaller mean MRWs). Finally, we found a significant relationship between mean RNFL thickness and mean MRW (Fig. 4-10d) across all eyes when using an exponential rise to maximum model (Patel et al., 2014b) to describe the data. In general, eyes with reduced RNFL thicknesses tended to have smaller (thinner) mean MRWs (P<.01).

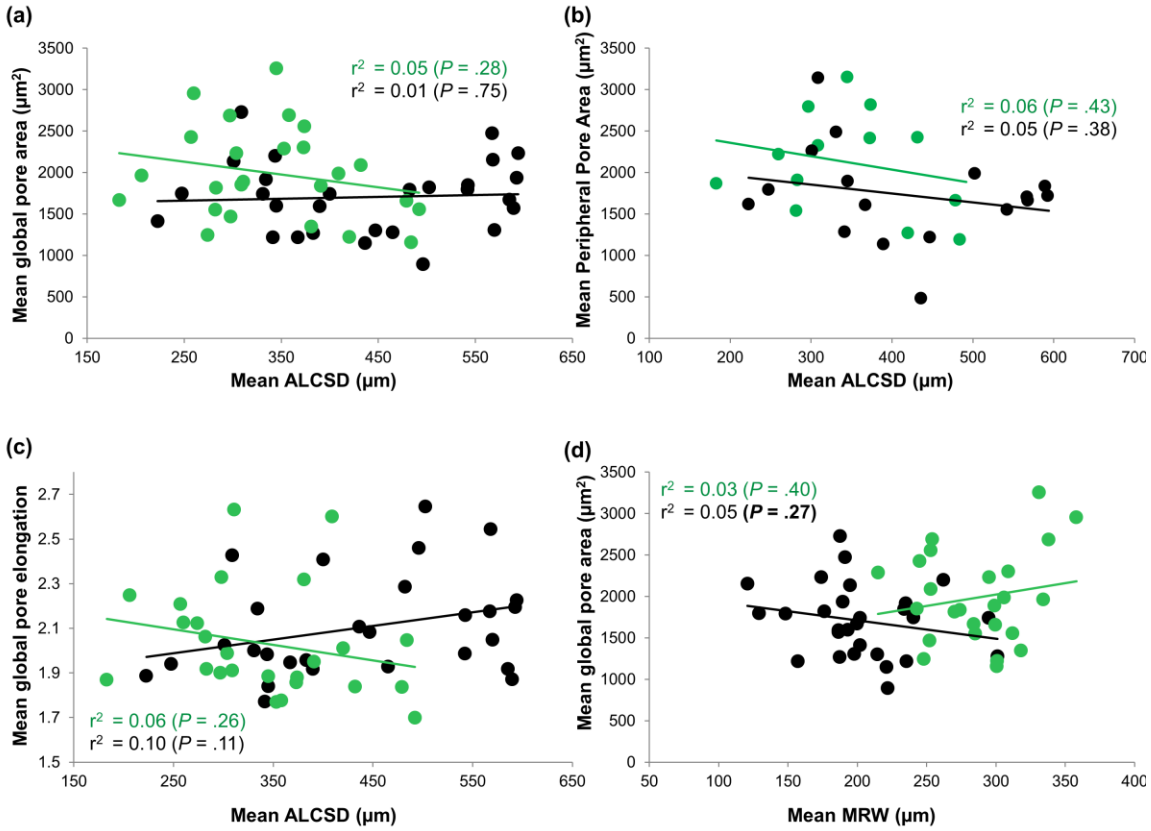

Figure 4-9. Comparison of ALCS pore and ONH parameters for older, normal eyes (green filled circles) and suspect/POAG eyes (black filled circles). Solid lines indicate linear regressions fit to the corresponding data points. No statistically significant relationships were found between (a) mean global pore area and mean ALCsD, (b) mean peripheral pore area and mean ALCSD, (c) mean global pore elongation and mean ALCSD, (d) mean global pore area and mean MRW within both older, normal eyes and suspect/POAG eyes.

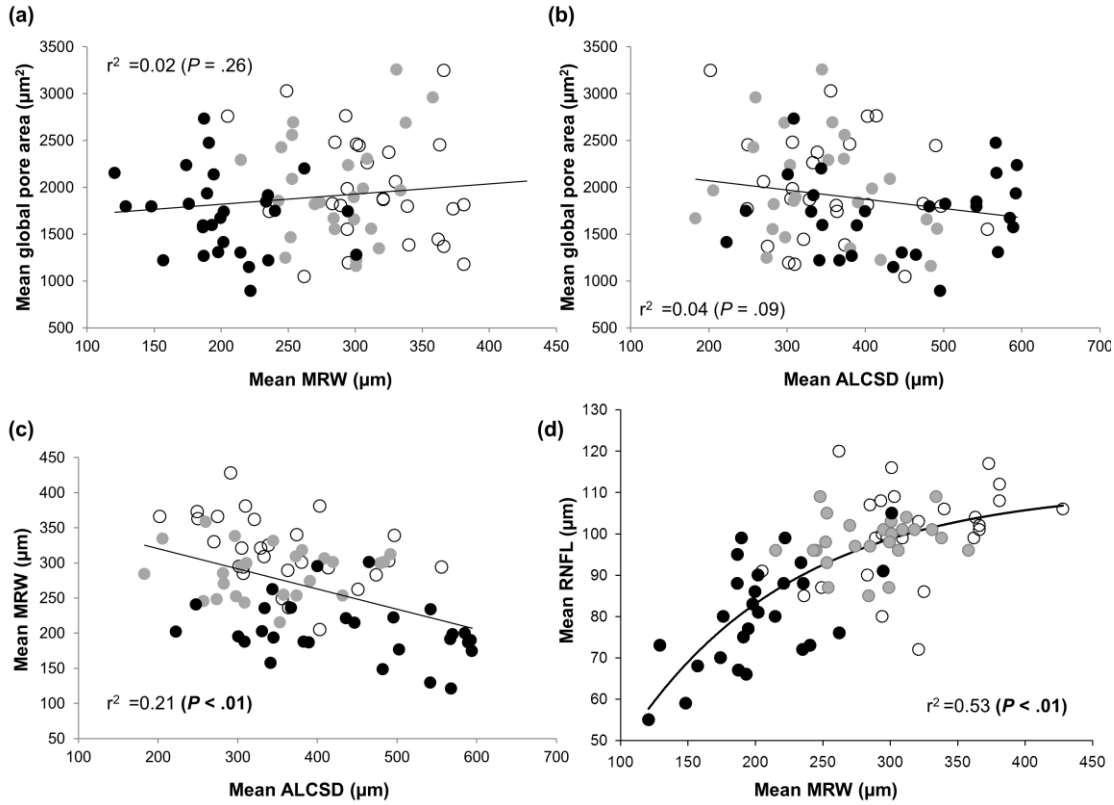

Figure 4-10. Comparison of global ALCS pore and ONH parameters for all young, normal eyes from Chapter 3 (open circles), older, normal eyes (gray filled circles) and suspect/POAG eyes (black filled circles). Solid lines indicate linear regressions fit to all data points within each plot. No statistically significant relationships were found between (a) mean global pore area and mean MRW or between (b) mean global pore area and mean ALCSD across all eyes. (c) However, mean MRW was significantly correlated with mean ALCSD across all eyes, as eyes with larger values of mean ALCSD tended to have smaller values of mean MRW. (d) Mean RNFL thickness was significantly thinner in eyes with thinner mean MRWs. This relationship was best-fit using an exponential rise to maximum model (Patel et al., 2014b) and described as RNFL = -31.73 + 142.99*(1-$e^{(-0.008*MRW)}$).

4.3.3 Examining visual fields and possible structure-function relationships

Given that a difference in mean ALCS pore area existed between normal older and suspect/POAG eyes in the superior-temporal sector (Table 4-4), we also sought to better understand whether corresponding differences in visual field sensitivity existed between these two groups. Sensitivity values measured at all tested locations in the superior and inferior visual fields were averaged to yield mean superior and mean inferior visual field sensitivities for each subject. These mean sensitivities were then averaged across all older normal eyes and across all suspect/POAG eyes (Table 4-5). There was a statistically significant difference in mean visual field sensitivity between the superior and inferior visual fields of ~1 dB across all older normal eyes (P=.03). However, despite a mean difference of 1.51 dB in the suspect/POAG eyes, there was no significant difference between the mean superior and inferior visual field sensitivities (P=.16), likely due to the large variability (standard deviations) of the measurements.

Table 4-5: Comparison of mean superior and mean inferior visual field sensitivities within older, normal eyes and within suspect/POAG eyes.

	Mean Superior Visual Field Sensitivity	Mean Inferior Visual Field Sensitivity	Mann-Whitney (*P* values)
Older Normal Eyes (n = 24 eyes)	29.76 ± 1.58	30.73 ± 1.30	.03*
Suspect/POAG Eyes (n = 28 eyes)	26.13 ± 4.71	27.64 ± 3.33	.16

***** Statistically significant difference between mean superior and inferior sensitivities within older, normal eyes (*P*<.05)

When comparing sensitivities between older normal and suspect/POAG eyes (Table 4-6), the mean superior and inferior visual field sensitivities measured in normal eyes were significantly different from those values measured in suspect/POAG eyes ($P<.01$). We compared these differences in visual field data with aforementioned differences in local ALCS pore area between the 2 groups. Relative to older normal eyes, suspect/POAG eyes had significantly smaller ALCS pores in the superior-temporal sector relative to older normal eyes (Table 4-4, $P=.01$) with correspondingly decreased mean sensitivities in the inferior visual field (Table 4-6; $P<.01$). However, despite having significantly decreased mean sensitivities in the superior visual field, suspect/POAG eyes did not show any corresponding differences in ALCS pore area in the inferior-temporal sector relative to normal eyes (Table 4-4, $P=.47$).

Table 4-6: Comparison of mean superior and mean inferior visual field sensitivities between older, normal eyes and suspect/POAG eyes.

	Older Normal Eyes (n = 24)	Suspect/POAG Eyes (n = 28)	Mann-Whitney (*P* values)
Mean Superior Visual Field Sensitivity	29.76 ± 1.58	26.13 ± 4.71	<.01*
Mean Inferior Visual Field Sensitivity	30.73 ± 1.30	27.64 ± 3.33	<.01*

***** Statistically significant difference between mean visual field sensitivities between older normal and suspect/POAG eyes

In addition to examining differences in ALCS pore structure and visual function between normal and suspect/POAG eyes, we also investigated whether basic structure-function relationships existed within the 26 suspect/POAG eyes who had ALCS pores quantified in both the superior-temporal and inferior-temporal sectors of the lamina. The sensitivities measured at all points in the superior visual field were first compared with the sensitivities measured at all points in the inferior visual field for each suspect/POAG eye. A statistically significant difference between the superior and inferior visual field sensitivities was calculated for 14 of 26 suspect/POAG eyes ($P<.05$). However, only 6 of 26 suspect/POAG eyes possessed ALCS pore areas that were significantly different between the superior-temporal and inferior-temporal sectors ($P<.05$). In 5 of these 6 suspect/POAG eyes, there was correspondence between the sector that contained the largest pore areas and the half of the visual field with decreased sensitivity (e.g., superior-temporal sector of the ALCS and the inferior visual field).

Finally, we plotted the ratio of the mean superior to inferior visual field sensitivities versus the ratio of the mean ALCS pore areas in the superior-temporal to inferior temporal sectors for all 26 suspect/POAG eyes (Fig. 4-11). While the regression line fit to the data points was not statistically significant ($P=.10$), there was a general tendency for suspect/POAG eyes with lower sensitivities in one half of the visual field (e.g., superior) to have larger pore areas in a corresponding sector (e.g., inferior-temporal) from a structure-function standpoint. For example, based on the linear regression, eyes with decreased superior field sensitivity relative to inferior field sensitivity (field ratios < 1) also tended to have larger pores in the inferior-temporal sector of the lamina (pore ratios < 1), corresponding to data points in the bottom left quadrant of Fig. 4-11. Likewise, eyes with decreased inferior field sensitivity relative to superior field sensitivity (field ratios > 1) also tended to have larger pores in in the superior-temporal sector of the lamina (pore ratios > 1), corresponding to data points in the top right quadrant of Fig. 4-11. These

aforementioned relationships were noted for 15 of 26 suspect/POAG eyes. The remaining 11 suspect/POAG eyes did not obey these relationships and fell into the top left or bottom right quadrants of Fig. 4-11.

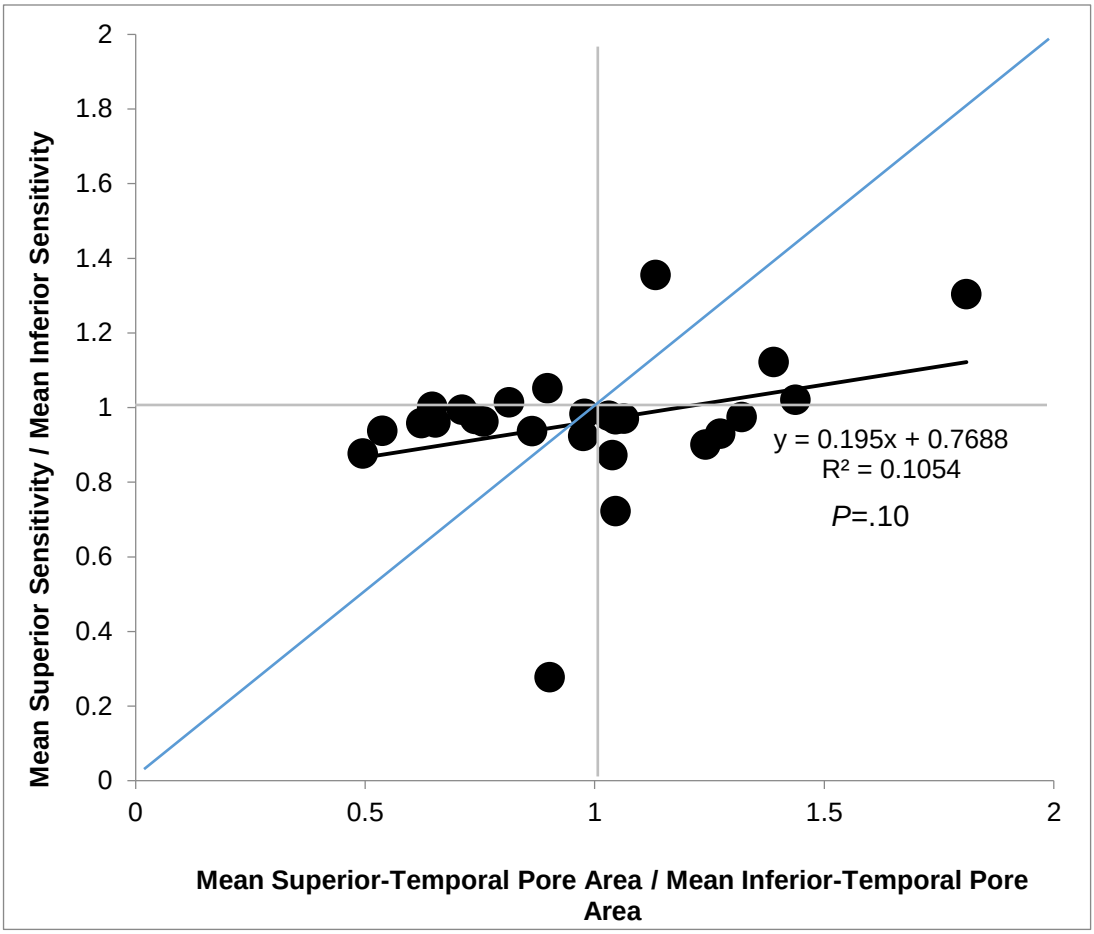

Figure 4-11. Comparison of the ratio of mean superior to mean inferior visual field sensitivities as a function of the ration of mean ALCS pore area in the superior-temporal to that in the inferior-temporal sector for 26 suspect/POAG eyes (black filled circles). The mean superior field sensitivity is greater than, equal to or less than the mean inferior field sensitivity for ratios greater than 1, equal to 1 (horizontal gray line) or less than 1, respectively. Mean ALCS pore area in the superior-temporal sector is greater than, equal to or less than the mean ALCS pore area in the inferior-temporal sector for ratios greater than 1, equal to 1 (vertical gray line) or less than 1, respectively. The solid black line represents a linear regression fit to all data points while the solid blue lines represents the 1:1 line. No statistically significant relationships was found between the ratio of visual fields and the ratio of local ALCS pore areas (*P*=.10).

4.4 Discussion

The purposes of this study were to (1) examine anterior lamina cribrosa surface (ALCS) microarchitecture and ONH geometry between suspect/POAG and age-matched normal eyes and (2) investigate whether relationships existed between ALCS pore and ONH parameters in suspect/POAG eyes and normal eyes. To our knowledge, this is the first study to examine both ALCS microarchitecture and ONH geometry in the same eyes of suspect/POAG patients and correlate ALCS pore microarchitecture and ONH structure across suspect/POAG eyes and age-matched normal eyes. While the majority of ONH parameters were significantly different between suspect/POAG and normal eyes, most ALCS pore parameters were similar. Significant relationships between ONH and ALCS pore parameters were sparse across suspect/POAG eyes and across normal eyes.

The ONH parameters measured in our subjects were similar to previously reported measurements. For example, our calculated values of mean ALCSD across older normal and suspect/POAG eyes (342.2 ± 82.5 μm and 439.2 ± 114.6 μm, respectively) are very similar to those reported by Furlanetto et al. (normal = 353 ± 70 μm; glaucoma = 438 ± 102 μm) from 57 normal subjects (mean age = 56 ± 17 years) and 47 glaucoma patients (mean age = 56 ± 16 years) (Furlanetto et al., 2013). The mean MRW measured across our normal eyes (287.1 ± 35.6 μm) is slightly lower than the median value of mean MRW reported by Chauhan et al. for their normal subjects (316.5 μm), despite both studies having comparably aged subjects (mean age = 57.5 ± 6.1 years in our study vs. median age = 65 years in Chauhan et al.) (Chauhan et al., 2013). Conversely, the mean MRW measured across our suspect/POAG eyes (203.0 ± 41.8 μm) is slightly larger than the median value of mean MRW reported by Chauhan et al. for their glaucoma patients (median: 182.7 μm) (Chauhan et al., 2013). However, mean RNFL thickness values measured in our normal and suspect/POAG eyes (normal = 98.2 μm; suspect/POAG = 80.1 μm) are very similar to the median

values measured by Chauhan et al. (normal = 95.9 µm; glaucoma = 70.0 µm) (Chauhan et al., 2013).

The ALCS pore parameters measured in our study were also consistent with pore measurements in other *in vivo* reports. Similar numbers of pores were quantified in our normal and suspect/POAG eyes (32 ± 19 and 56 ± 23, respectively) as in a study by Wang et al. (37 ± 19 and 57 ± 25, respectively) that used swept source OCT to image the laminar microarchitecture (Wang et al., 2013). Mean values of global ALCS pore area and elongation measured in our normal eyes (1988 ± 559 μm^2 and 2.03 ± 0.24, respectively) were smaller than ALCS pore values measured in 20 normal eyes using an AOSLO by Akagi et al. (2507 ± 826 μm^2 and 2.13 ± 0.47, respectively), but comparable to normal pore values measured by Wang et al. (1970 ± 310 μm^2 and 2.06 ± 0.14, respectively) (Akagi et al., 2012; Wang et al., 2013). Similarly, mean values of global ALCS pore area and elongation measured in our suspect/POAG eyes (1704 ± 429 μm^2 and 2.10 ± 0.22, respectively) were smaller than ALCS pore values measured in 20 glaucomatous eyes by Akagi et al. (3103 ± 857 μm^2 and 2.38 ± 0.79, respectively), but comparable to pore values measured in glaucomatous eyes by Wang et al. (1800 ± 330 μm^2 and 2.04 ± 0.11, respectively) (Akagi et al., 2012; Wang et al., 2013).

Significant differences were measured in many ONH and ALCS pore parameters between our older normal and suspect/POAG eyes. Many of these differences are consistent with reports in human and experimental glaucoma eyes, as well as with clinical observations. The ALCS was more steeply curved (or “cupped”, with a smaller mean RoC) and located deeper within the optic nerve head (larger mean ALCSD) in suspect/POAG eyes. These results are similar to those reported in histomorphometric studies in non-human primates that have demonstrated a posterior deformation (or bowing) and migration of the ALCS in early experimental glaucoma (Yang et al., 2007b; Yang et al., 2015). *In vivo* measurements have also shown that glaucomatous eyes have

increased values of mean ALCSD compared to normal eyes (Furlanetto et al., 2013; Park et al., 2015). We also found that our suspect/POAG eyes had a reduced amount neuronal tissue that entered and was contained within the ONH (i.e., reduced mean MRWs, prelaminar tissue volumes and rim volumes), as well as reduced amounts in the peripapillary region (reduced RNFL thickness), compared to age-matched normal subjects. These results are in agreement with *in vivo* studies showing reduced mean MRWs (Chauhan et al., 2013), prelaminar tissue volumes (Kim et al., 2016) and neuroretinal rim volumes (Patel et al., 2014b) in glaucomatous eyes. The loss of prelaminar tissue, coupled with a posterior bowing of the ALCS, likely results in the increased cup-to-disc ratio classically observed by clinicians in glaucoma (Burgoyne and Downs, 2008). In addition, mean global ALCS pore area in our suspect/POAG eyes was not statistically different (P = .07) from our older normal eyes, a result that is similar those of Wang et al. (Wang et al., 2013). We also found a smaller separation between pores (lower mean global ALCS pore NND) in suspect/POAG eyes compared to normals.

Given that increased age is a risk factor for the onset of glaucoma (Friedman et al., 2004; Tham et al., 2014), a continuum of change in ONH structure and lamina cribrosa microarchitecture could occur as the older, normal eye progresses to an early altered state (as a glaucoma suspect or early POAG eye) and then further evolves into an eye with moderate to severe glaucoma. To better understand whether structural differences existed in some of the earliest states of disease, we compared ONH and ALCS pore parameters between normal, older eyes and glaucoma suspect/POAG eyes with very mild field loss (Humphrey visual field mean deviations (MDs) < -3 dB) (Table 4-2). Nearly all ONH parameters were significantly different in this subgroup of suspect/POAG eyes (compared to normals), despite the fact that these suspect/POAG eyes had only minimal losses in visual field sensitivity. Suspect/POAG eyes with MDs < -

3 dB tended to have ALCSs that were more deeply located in the ONH (larger mean ALCSD) and more steeply curved (smaller mean RoCs), and had less neuronal tissue (given by lower values of neuroretinal rim volume, mean MRW and mean RNFL Thickness). When examining global ALCS pore parameters, only mean global ALCS pore NND was significantly different between the groups, as suspect/POAG eyes with MDs < -3 dB tended to have more closely spaced pores (lower values of mean pore NND) compared to normal eyes.

Dramatically different results were seen when comparing ONH and ALCS pore parameters between suspect/POAG eyes with mild field losses (MDs < -3 dB) and those with more moderate field losses (MDs > -3 dB) (Table 4-3). Prelaminar tissue volume was the only ONH or global ALCS pore parameter to be significantly different between these 2 groups. Suspect/POAG eyes with mild field loss (MDs < -3 dB) tended to have thicker prelaminar tissue volumes compared to suspect/POAG eyes with more moderate field losses (MDs > -3 dB). However, all other ONH and ALCS pore parameters (including mean ALCSD, mean MRW and mean RNFL thickness) were not different between the two groups. These results, when coupled with the multiple aforementioned differences noted between normal older eyes and the suspect/POAG eyes with MDs < -3 dB, could suggest that most ONH parameters (e.g., mean ALCSD, mean MRW, rim volume) tend to change very early in the disease process before more moderate abnormalities in visual fields occur. Such a notion may be supported by the time course of change measured in these parameters in longitudinal studies of experimental glaucoma. Multiple reports have found that mean ALCSD and mean MRW are often the first ONH parameters to significantly change in a non-human primate model of experimental glaucoma and that these changes occur earlier than the first measured changes in RNFL thickness (He et al., 2014b; Ivers et al., 2015; Rajagopalan; et al., 2015). The significant differences measured in these parameters between older normal

human eyes and suspect/POAG eyes with MDs < -3 dB (or those with very early signs of disease), but not between suspect/POAG eyes with MDs < -3 dB and those with MDs > -3 dB (or more moderate signs of disease), support the observations reported in experimental glaucoma, namely that dramatic changes in some ONH parameters can occur at very early states of disease. However, further investigation of this idea is warranted, particularly given the limited number of subjects that were included in this study for suspect/POAG eyes with MDs < -3 dB and those with MDs > -3 dB.

In addition to global pore analyses, we examined and compared ALCS pore parameters on local spatial scales within normal and suspect/POAG eyes. The mean values of ALCS pore area measured within sectors and zones in our normal eyes (superior-temporal: 2177 ± 651 μm^2; temporal: 1868 ± 623 μm^2; inferior-temporal 2260 ± 1457 μm^2; central: 1966 ± 623 μm^2; peripheral: 2121 ± 610 μm^2) are larger than those reported from histological and *in vivo* studies performed in normal human eyes. Dandona et al. quantified median pore areas within central and peripheral regions of each major meridian (supero-central: 1691 ± 134 μm^2; supero- peripheral: 1648 ± 81 μm^2; temporo-central: 1260 ± 100 μm^2; tempo-peripheral: 1311 ± 94 μm^2; infero-central: 1366 ± 93 μm^2; and infero-peripheral: 1797 ± 111 μm^2) (Dandona et al., 1990) in 7 black (mean age: 67.3 ± 3.1 years) and 9 white (mean age: 67.2 ± 3.8 years) normal human donor eyes. Overall median pore area in blacks and whites were 1474 ± 100 μm^2 and 1456 ± 102 μm^2 respectively. Nadler et al. quantified local pore areas based on *in vivo* images acquired in 18 healthy normal eyes (mean age: 32.9 ± 12.9 years) (superior: 1346 ± 163 μm^2, temporal: 1286 ± 316 μm^2, inferior: 1319 ± 129 μm^2, central: 1340 ± 207 μm^2 and peripheral: 1205 ± 144 μm^2 (overall mean pore area: 1302 ± 173 μm^2) (Nadler et al., 2014). While the *in vivo* pore areas presented by Nadler at el. are similar to the *ex vivo* pore areas presented by Dandona et al., the pore areas in both of these studies are smaller than *in vivo* measurements reported in this study and those by Wang

et al. and Akagi et al. (Akagi et al., 2012; Wang et al., 2013). The reasons for these differences are not clear and should be the subject of future investigation.

When analyzing ALCS pore parameters on a local level, we found no significant differences in mean ALCS pore area between older normal eyes and suspect/POAG eyes in the temporal, inferior-temporal and central zones. While there was a tendency for ALCS pores to be smaller in suspect/POAG eyes in the peripheral zone, the difference was not statistically significant (*P*=.10). However, ALCS pore areas were significantly smaller in suspect/POAG eyes in the superior-temporal sector. These results seem to be in opposition to findings reported by Ivers et al. in a longitudinal study of non-human primates induced with experimental glaucoma in which mean ACLS pore area significantly increased in the temporal sector and central and peripheral zones at the first time-point of change in pore geometry (Ivers et al., 2015). Nevertheless, our results are more consistent with data published by Wang et al. (Wang et al., 2013) that reported no significant differences in pore area between normal human and glaucomatous eye, and a tendency for laminar beam thickness to increase and pore area to decrease with worsening MDs in glaucomatous eyes. We do not have a clear explanation for why *in vivo* studies have observed no change or a decrease in laminar pore area in human glaucomatous eyes. Further work is necessary to understand potential differences between the results measured *in vivo* versus those found in postmortem tissue.

One of the primary goals of this study was to investigate whether relationships existed between ALCS pore microarchitecture and ONH structural parameters within groups. Mean MRW and mean RNFL thickness were positively correlated in suspect/POAG eyes (Figure 4-9c), as were mean global ACLS pore area and NND (i.e., pores that were larger also tended to be further separated) (Figure 4-10a). The size and shape of ALCS pores (pore area and elongation) measured globally, by sector, or by

central/peripheral region were not related to the depth of the ALCS (mean ALCSD) in normal eyes or in suspect/POAG eyes (Figure 4-9). Similarly, although mean MRW and mean global ALCS pore area were smaller in suspect/POAG eyes than in older normal eyes, no correlation was measured between mean global ALCS pore area and mean MRW within normal or suspect/POAG eyes (Figure 4-9d). However, when examining parameters across all young, normal eyes (from Chapter 3), older, normal eyes and suspect/POAG eyes, we found a statistically significant decrease in mean MRW with increasing values of mean ALCSD (Figure 4-10c). In other words, eyes with more posteriorly-located ALCSs tended to have thinner MRWs. It is unclear if the reduction is mean MRW with increasing depth of the ALCS is due to a normal aging process and/or represents a disease associated change. Future studies that longitudinally track changes in mean MRW and ALCSD within the same normal and early glaucomatous eyes are required to provide deeper insights into the meaning of this relationship.

Our study was limited in a few aspects. While AOSLOs provide high-resolution, high contrast images of the lamina cribrosa microarchitecture, it remains challenging to image laminar beams and pores throughout the entire depth of this structure. Therefore, we limited our quantification to anterior laminar surface pores that could be most reliably imaged and detected. It will be important to build on this work by examining differences in pore and beam properties through the entire extent of the lamina to better relate full thickness laminar microarchitecture parameters with ONH parameter and visual field data. Additional, our study included a limited number of subjects, particularly for comparisons of ONH and ALCS pore parameters made between suspect/POAG eyes with MDs <3 dB and those with MDs > 3dB (Table 4-3). While our current number of subjects was adequate to provide sufficient statistical power for nearly all of our comparisons, future studies could examine these structural parameters using an

increased number of patients and determine whether the relationships found in this study have the potential to become more robust.

In conclusion, this report provides new detailed measurements of structural differences in lamina cribrosa pore, laminar surface and ONH geometries in normal eyes and in suspect/POAG eyes with different levels of visual field damage. ONH parameters were drastically different between older normal subjects and suspect/POAG patients. Global ALCS pore microarchitecture was largely similar between normal and suspect/POAG eyes, while local analyses revealed that suspect/POAG eyes tended to have smaller pore areas in the superior-temporal sector (compared to normal eyes). Moreover, the present study did not find a large number of significant relationships between ONH parameters and global ALCS pore microarchitecture. The findings of this study can serve as a baseline for future studies that seek to characterize relationships between ONH parameters and lamina cribrosa pore microarchitecture throughout the entire depth of the lamina cribrosa to better understand changes in ONH structure and visual function in early glaucoma.

4.5 Acknowledgements

This work was supported by National Institutes of Health (NIH) Grants R01 EY021783 and P30 EY07551, and the University of Houston, College of Optometry. The authors thank Mindy Fox for help with data collection and Crawford Downs and Ronald Harwerth for helpful discussions. We also thank Dr. Nimesh Patel for providing the MATLAB program used to calculate the center of the foveal pit in each subject. Danica Marrelli has served as a consultant with Alcon, Allergan, Merck, and Carl Zeiss Meditec.

CHAPTER 5

General conclusions

5.1 General conclusion

The ONH and lamina cribrosa provide structural and functional support to retinal ganglion cell axons that exit the retina and travel to the LGN. A comprehensive body of literature suggests that the initial damage to retinal ganglion cell axons occurs at the level of the lamina cribrosa in glaucoma (Quigley and Anderson, 1976a; Minckler et al., 1977; Bellezza et al., 2003; Burgoyne et al., 2004). Simultaneous examination of the neural and non-neural supportive tissues in the ONH is necessary to understand the pathophysiology of the disease. Identifying glaucoma-related structural changes requires (1) understanding the intra-subject and population variation of the structural parameters under consideration in normal eyes, (2) accounting for changes in these parameters due to normal aging and other risk factors (such as axial length), (3) understanding how these structural parameters differ in glaucomatous eyes (compared to normal age-matched subjects) and (4) understanding the relationships and interactions between ONH structural and lamina cribrosa microarchitecture parameters. The experiments carried out in this body of work were designed to provide a more detailed understanding of the structural properties of the physiologically normal ONH in young and older human eyes (Chapters 2 and 3), and how these structural properties differ between normal eyes and eyes of glaucoma suspects and those with early to moderate stages of glaucoma (Chapter 4).

5.1.1 Experiment 1 (Chapter 2): Characterize ONH and lamina cribrosa geometry and their relationship with axial length in young, normal eyes

Newly developed ONH structural parameters, such as mean anterior lamina cribrosa surface depth (ALCSD) and mean minimum rim width (MRW), are being examined in human glaucoma patients and animal models of experimental glaucoma as possible biomarkers of earlier disease onset (compared with other structural measures, such as

RNFL thickness). This study examined whether relationships existed between normal ONH and lamina cribrosa geometry, as well as their variation with axial length in eyes of 97 normal young subjects (mean age = 26.4 ± 3.8 years). Mean MRW and mean sMRW were significantly thinner in eyes with more posteriorly located ALCS's (R^2=0.16, *P*<.01; R^2=0.23, *P*<.01), potentially indicating that axons are pulled toward the BMO in the eyes with a deeper lamina. While mean MRW was thinner in eyes with larger BMO areas (R^2=0.18; *P*<.01), there was no relationship between mean sMRW and BMO area (*P*=.20). The fact that mean sMRW was invariant with BMO area could imply that the total number of axons in normal eyes is constant regardless of the size of the BMO. In addition, eyes with longer axial lengths had larger BMO areas (R^2=0.19; *P*<.01) and tended to have shallower mean ALCSDs (*P*=.07). The larger BMO areas found in axially longer eyes could potentially result from retinal and scleral stretching that occurs as the eye undergoes axial elongation during development. The results of this study not only better defined relationships between ONH parameters in eyes of different axial lengths, but also serve as normative data for similar measurements acquired in older eyes and eyes with different severities and forms of glaucoma.

5.1.2 Experiment 2 (Chapter 3): Determine the variability in lamina cribrosa microarchitecture and ONH geometry between fellow eyes of normal subjects and as a function of aging

Several studies suggest that normal aging could increase the susceptibility of the ONH to glaucomatous damage. We sought to measure and examine whether structural differences exist in ALCS pore and ONH geometries in normal human eyes of different ages. Prior to examining ONH structure in normal eyes with age, we first assessed differences in ALCS pore and ONH geometry between fellow eyes of 32 normal subjects (mean age = 37.1 ± 15.9 years; range = 21 - 66 years) *in vivo* using AOSLO and

SDOCT imaging, respectively. This analysis was performed to better understand the variability inherent in these parameters between fellow eyes of normal subjects, as well as to best ensure that any potential structural differences measured in normal eyes as a function of age are due to the aging process itself and not to the normal variability inherent in these examined parameters between fellow eyes.

No statistically significant differences were measured between right and left eyes for any examined ONH or mean global ALCS pore parameters. The coefficients of variation for all ONH parameters ranged between 11.16% and 26.13%, and between 13.67% and 27.67% for all mean global ALCS pore parameters. However, when global ALCS pore parameters were compared between right and left eyes of each individual subject, statistically significant differences were observed in some parameters within some individuals. These differences could have been due to the possibility that the area over which ALCS pores were imaged and quantified in one eye was not the mirror image of the region that was imaged and examined in the fellow eye of the same subject.

Our analyses of ONH structure and ALCS pore microarchitecture between 28 young (20-30 years) and 25 older (>50 years) eyes revealed that most ONH and global ALCS pore parameters were similar between young and older eyes. Mean MRW, a potential surrogate metric for the number of retinal ganglion cell axons passing into the ONH, was lower (or thinner) in older eyes compared to young eyes. This reduction in mean MRW in older eyes could reflect an age-related loss of retinal ganglion cell axons (Patel et al., 2014a). In addition, all global ALCS pore parameters were similar between the young and older groups of subjects. Our findings, coupled with those from other studies, show that some of the ONH and laminar structural parameters measured in older normal eyes have values that lie between those measured in young, normal eyes and those measured in early glaucomatous eyes, potentially lending partial support to the idea that glaucoma contains an accelerated aging component. The data from these

normal subjects will serve as control data for future studies of patients with different forms of glaucoma and better enable us to distinguish between the effects of aging and the effects of aging plus glaucoma on laminar and ONH geometries.

5.1.3 Experiment 3 (Chapter 4): Determine whether differences exist in vivo in lamina cribrosa microarchitecture and ONH geometry between normal and glaucomatous eyes

Previous *in vivo* studies have separately compared lamina cribrosa microarchitecture or optic nerve head (ONH) geometry between normal and glaucomatous eyes. The purposes of this study were to jointly examine ONH geometry and anterior lamina cribrosa surface (ALCS) microarchitecture within the same normal older eyes and suspect/POAG eyes, and compare parameters between groups. Consistent with previous studies, we found most ONH parameters to be significantly different between suspect/POAG eyes and normal older eyes. Suspect/POAG eyes tended to have significantly reduced neuronal parameters (e.g., prelaminar tissue volume, rim volume, mean MRW and mean RNFL thickness) with anterior lamina cribrosa surfaces that were located more deeply (larger mean ALCSD) and were more significantly curved (smaller mean RoC) than our age-matched normal eyes. While mean global ALCS pore area and elongation were similar between suspect/POAG and older normal eyes, ALCS pores tended to be more closely spaced in suspect/POAG eyes. However, local pore analyses found that ALCS pore area was significantly smaller in suspect/POAG eyes (relative to normal eyes) in the superior-temporal sector of the ONH, a region that is known to be vulnerable and prone to the development of retinal nerve fiber layer defects in glaucoma (Hood et al., 2013). Additionally, we subdivided our suspect/POAG eyes to compare ONH and laminar pore parameters between older normal eyes, suspect/POAG eyes with mild visual field mean deviations (MDs) < -3 dB and POAG eyes with more moderate

visual field MDs > -3 dB. Significant differences were found in the vast majority of ONH and global ALCS pore parameters between older normal eyes and the suspect/POAG eyes with MDs < -3 dB, but not between suspect/POAG eyes with MDs < -3 dB and POAG eyes with more moderate MDs (> -3 dB). This result suggests that the most substantial structural changes in the ONH occur very early in the disease process when patients have very mild visual field loss.

Significant relationships were found between ONH and ALCS pore parameters within groups. For example, mean MRW and mean RNFL thickness were positively correlated in suspect/POAG eyes, as were mean global ACLS pore area and NND (i.e., pores that were larger also tended to be further separated). There was also a tendency for ALCS pores to be more elliptically shaped (increased pore elongation) in suspect/POAG eyes that had larger pore areas and more posteriorly located ALCSs, but the relationships were not statistically significant (*P*=.06 and .11, respectively). Outside of these aforementioned results, we found no statistically significant relationships between ALCS pore and ONH parameters within older normal or suspect/POAG eyes. In conclusion, this study is significant in that it provides new detailed measurements of structural differences in lamina cribrosa pore, laminar surface and ONH geometries in normal eyes and in suspect/POAG eyes with different levels of visual field damage.

5.2 Summary and future directions

High resolution *in vivo* imaging provides the opportunity to better understand the physiological variability in ONH morphology and lamina cribrosa mircoarchitecture in living normal eyes, as well as the impact of normal aging and glaucoma on these structures. While these experiments have focused on ONH structure and pore microarchitecture *on the anterior laminar surface*, it will be important to extend these analyses to better understand lamina cribrosa microarchitecture throughout its entire

extent across the spectrum of normal young eyes, to normal older eyes, to suspect/early POAG eyes and to more moderate and severe forms of glaucoma. It is also important to understand not just how laminar pores changes, but also how laminar beams change with aging and glaucoma. Automated algorithms recently developed in our lab to quantify ALCS beams and pores in images from non-human primates are now being tested on human lamina cribrosa images to provide objective and faster quantification of lamina microarchitecture. These algorithms can not only be used to automatically calculate ALCS pore parameters, but will also provide more detailed information on the surrounding laminar beams, including change in their thickness and orientation, with disease. Additionally, the forms of structural imaging and analysis discussed in this dissertation ultimately need to be combined with other types of structural imaging (such as capillary perfusion maps) and refined methods of functional imaging (including the electroretinogram to measure the photopic negative response) to better understand how different mechanisms might work in concert, particularly in glaucoma suspects and patients in early stages of human glaucoma. Such efforts to better characterize the earliest time points and markers of structural and/or functional losses could better facilitate earlier diagnosis and enable more informed clinical decision making regarding treatment options.

REFERENCES

Akagi, T., Hangai, M., Takayama, K., Nonaka, A., Ooto, S., Yoshimura, N., 2012. In vivo imaging of lamina cribrosa pores by adaptive optics scanning laser ophthalmoscopy. Invest Ophthalmol Vis Sci 53, 4111-4119.

Albon, J., Karwatowski, W.S., Avery, N., Easty, D.L., Duance, V.C., 1995. Changes in the collagenous matrix of the aging human lamina cribrosa. The British journal of ophthalmology 79, 368-375.

Albon, J., Karwatowski, W.S., Easty, D.L., Sims, T.J., Duance, V.C., 2000a. Age related changes in the non-collagenous components of the extracellular matrix of the human lamina cribrosa. The British journal of ophthalmology 84, 311-317.

Albon, J., Purslow, P.P., Karwatowski, W.S., Easty, D.L., 2000b. Age related compliance of the lamina cribrosa in human eyes. The British journal of ophthalmology 84, 318-323.

Anderson, D.R., 1969. Ultrastructure of Human and Monkey Lamina Cribrosa and Optic Nerve Head. Archives of ophthalmology 82, 800-&.

Anderson, D.R., Hendrickson, A., 1974. Effect of intraocular pressure on rapid axoplasmic transport in monkey optic nerve. Investigative ophthalmology 13, 771-783.

ANSI, 2014. American National Standard for safe use of laser (ANSI 136.1 - 2014). The Laser Institute of America.

Bellezza, A.J., Hart R.T., Burgoyne C.F., 2000. The optic nerve head as a biomechanical structure: initial finite element modeling. Investigative Ophthalmology & Visual Science 2000, 2991-3000.

Bellezza, A.J., Rintalan, C.J., Thompson, H.W., Downs, J.C., Hart, R.T., Burgoyne, C.F., 2003. Deformation of the lamina cribrosa and anterior scleral canal wall in early experimental glaucoma. Investigative Ophthalmology & Visual Science 44, 623-637.

Bhandari, A., Fontana, L., Fitzke, F.W., Hitchings, R.A., 1997. Quantitative analysis of the lamina cribrosa in vivo using a scanning laser opthalmoscope. Curr Eye Res 16, 1-8.

Borges, V.M., Danesh-Meyer, H.V., Black, J.M., Thompson, B., 2015. Functional effects of unilateral open-angle glaucoma on the primary and extrastriate visual cortex. Journal of vision 15, 9.

Bowd, C., Zangwill, L.M., Berry, C.C., Blumenthal, E.Z., Vasile, C., Sanchez-Galeana, C., Bosworth, C.F., Sample, P.A., Weinreb, R.N., 2001. Detecting early glaucoma by assessment of retinal nerve fiber layer thickness and visual function. Invest Ophthalmol Vis Sci 42, 1993-2003.

Burgoyne, C.F., 2011. A biomechanical paradigm for axonal insult within the optic nerve head in aging and glaucoma. Experimental eye research 93, 120-132.

Burgoyne, C.F., Downs, J.C., 2008. Premise and prediction-how optic nerve head biomechanics underlies the susceptibility and clinical behavior of the aged optic nerve head. Journal of glaucoma 17, 318-328.

Burgoyne, C.F., Downs, J.C., Bellezza, A.J., Hart, R.T., 2004. Three-dimensional reconstruction of normal and early glaucoma monkey optic nerve head connective tissues. Invest Ophthalmol Vis Sci 45, 4388-4399.

Burgoyne, C.F., Downs, J.C., Bellezza, A.J., Suh, J.K., Hart, R.T., 2005. The optic nerve head as a biomechanical structure: a new paradigm for understanding the role of IOP-related stress and strain in the pathophysiology of glaucomatous optic nerve head damage. Progress in retinal and eye research 24, 39-73.

Chauhan, B.C., O'Leary, N., Almobarak, F.A., Reis, A.S., Yang, H., Sharpe, G.P., Hutchison, D.M., Nicolela, M.T., Burgoyne, C.F., 2013. Enhanced detection of open-angle glaucoma with an anatomically accurate optical coherence tomography-derived neuroretinal rim parameter. Ophthalmology 120, 535-543.

Choi, S.S., Zawadzki, R.J., Lim, M.C., Brandt, J.D., Keltner, J.L., Doble, N., Werner, J.S., 2011. Evidence of outer retinal changes in glaucoma patients as revealed by ultrahigh-resolution in vivo retinal imaging. The British journal of ophthalmology 95, 131-141.

Cullum, N.A., Mahon, J., Stringer, K., McLean, W.G., 1991. Glycation of rat sciatic nerve tubulin in experimental diabetes mellitus. Diabetologia 34, 387-389.

Curcio, C.A., Allen, K.A., 1990. Topography of ganglion cells in human retina. The Journal of comparative neurology 300, 5-25.

Dandona, L., Quigley, H.A., Brown, A.E., Enger, C., 1990. Quantitative regional structure of the normal human lamina cribrosa. A racial comparison. Archives of ophthalmology 108, 393-398.

Danias, J., Shen, F., Goldblum, D., Chen, B., Ramos-Esteban, J., Podos, S.M., Mittag, T., 2002. Cytoarchitecture of the retinal ganglion cells in the rat. Invest Ophthalmol Vis Sci 43, 587-594.

Downs, J.C., Roberts, M.D., Burgoyne, C.F., 2008. Mechanical environment of the optic nerve head in glaucoma. Optometry and vision science : official publication of the American Academy of Optometry 85, 425-435.

Downs, J.C., Yang, H., Girkin, C., Sakata, L., Bellezza, A., Thompson, H., Burgoyne, C.F., 2007. Three-dimensional histomorphometry of the normal and early glaucomatous monkey optic nerve head: neural canal and subarachnoid space architecture. Invest Ophthalmol Vis Sci 48, 3195-3208.

Duncan, R.O., Sample, P.A., Weinreb, R.N., Bowd, C., Zangwill, L.M., 2007. Retinotopic organization of primary visual cortex in glaucoma: Comparing fMRI measurements of cortical function with visual field loss. Progress in retinal and eye research 26, 38-56.

Fechtner, R.D., Weinreb, R.N., 1994. Mechanisms of optic nerve damage in primary open angle glaucoma. Survey of ophthalmology 39, 23-42.

Fischer, Q.S., Kirby, M.A., 1991. Number and distribution of retinal ganglion cells in anubis baboons (Papio anubis). Brain, behavior and evolution 37, 189-203.

Fortune, B., Burgoyne, C.F., Cull, G., Reynaud, J., Wang, L., 2013. Onset and progression of peripapillary retinal nerve fiber layer (RNFL) retardance changes occur earlier than RNFL thickness changes in experimental glaucoma. Invest Ophthalmol Vis Sci 54, 5653-5661.

Foster, P.J., Johnson, G.J., 2001. Glaucoma in China: how big is the problem? The British journal of ophthalmology 85, 1277-1282.

Friedman, D.S., Wolfs, R.C., O'Colmain, B.J., Klein, B.E., Taylor, H.R., West, S., Leske, M.C., Mitchell, P., Congdon, N., Kempen, J., 2004. Prevalence of open-angle glaucoma among adults in the United States. Archives of ophthalmology 122, 532-538.

Furlanetto, R.L., Park, S.C., Damle, U.J., Sieminski, S.F., Kung, Y., Siegal, N., Liebmann, J.M., Ritch, R., 2013. Posterior displacement of the lamina cribrosa in glaucoma: in vivo interindividual and intereye comparisons. Invest Ophthalmol Vis Sci 54, 4836-4842.

Gardiner, S.K., Boey, P.Y., Yang, H., Fortune, B., Burgoyne, C.F., Demirel, S., 2015. Structural Measurements for Monitoring Change in Glaucoma: Comparing Retinal Nerve Fiber Layer Thickness With Minimum Rim Width and Area. Invest Ophthalmol Vis Sci 56, 6886-6891.

Girkin, C.A., McGwin, G., Jr., Long, C., DeLeon-Ortega, J., Graf, C.M., Everett, A.W., 2004. Subjective and objective optic nerve assessment in African Americans and whites. Invest Ophthalmol Vis Sci 45, 2272-2278.

Girkin, C.A., McGwin, G., Jr., Sinai, M.J., Sekhar, G.C., Fingeret, M., Wollstein, G., Varma, R., Greenfield, D., Liebmann, J., Araie, M., Tomita, G., Maeda, N., Garway-Heath, D.F., 2011. Variation in optic nerve and macular structure with age and race with spectral-domain optical coherence tomography. Ophthalmology 118, 2403-2408.

Gordon, M.O., Beiser, J.A., Brandt, J.D., Heuer, D.K., Higginbotham, E.J., Johnson, C.A., Keltner, J.L., Miller, J.P., Parrish, R.K., 2nd, Wilson, M.R., Kass, M.A., 2002. The Ocular Hypertension Treatment Study: baseline factors that predict the onset of primary open-angle glaucoma. Archives of ophthalmology 120, 714-720; discussion 829-730.

Grieshaber, M.C., Mozaffarieh, M., Flammer, J., 2007. What is the link between vascular dysregulation and glaucoma? Survey of ophthalmology 52 Suppl 2, S144-154.

Gupta, N., Greenberg, G., de Tilly, L.N., Gray, B., Polemidiotis, M., Yucel, Y.H., 2009. Atrophy of the lateral geniculate nucleus in human glaucoma detected by magnetic resonance imaging. The British journal of ophthalmology 93, 56-60.

Harwerth, R.S., Wheat, J.L., 2008. Modeling the effects of aging on retinal ganglion cell density and nerve fiber layer thickness. Graefe's archive for clinical and experimental ophthalmology = Albrecht von Graefes Archiv fur klinische und experimentelle Ophthalmologie 246, 305-314.

Hayreh, S.S., 2011. Ischemic Optic Neuropathies. Springer-Verlag, Berlin Heidelberg.

Hayreh, S.S., Vrabec, F., 1966. The structure of the head of the optic nerve in rhesus monkey. American journal of ophthalmology 61, 136-150.

He, L., Ren, R., Yang, H., Hardin, C., Reyes, L., Reynaud, J., Gardiner, S.K., Fortune, B., Demirel, S., Burgoyne, C.F., 2014a. Anatomic vs. acquired image frame discordance in spectral domain optical coherence tomography minimum rim measurements. PloS one 9, e92225.

He, L., Yang, H., Gardiner, S.K., Williams, G., Hardin, C., Strouthidis, N.G., Fortune, B., Burgoyne, C.F., 2014b. Longitudinal detection of optic nerve head changes by spectral domain optical coherence tomography in early experimental glaucoma. Invest Ophthalmol Vis Sci 55, 574-586.

Herbin, M., Boire, D., Ptito, M., 1997. Size and distribution of retinal ganglion cells in the St. Kitts green monkey (Cercopithecus aethiops sabeus). The Journal of comparative neurology 383, 459-472.

Hernandez, M.R., 2000. The optic nerve head in glaucoma: Role of astrocytes in tissue remodeling. Progress in retinal and eye research 19, 297-321.

Hernandez, M.R., Andrzejewska, W.M., Neufeld, A.H., 1990. Changes in the Extracellular-Matrix of the Human Optic-Nerve Head in Primary Open-Angle Glaucoma. American journal of ophthalmology 109, 180-188.

Hernandez, M.R., Luo, X.X., Andrzejewska, W., Neufeld, A.H., 1989. Age-related changes in the extracellular matrix of the human optic nerve head. American journal of ophthalmology 107, 476-484.

Hood, D.C., Raza, A.S., de Moraes, C.G., Liebmann, J.M., Ritch, R., 2013. Glaucomatous damage of the macula. Progress in retinal and eye research 32, 1-21.

Howell, G.R., Libby, R.T., Jakobs, T.C., Smith, R.S., Phalan, F.C., Barter, J.W., Barbay, J.M., Marchant, J.K., Mahesh, N., Porciatti, V., Whitmore, A.V., Masland, R.H., John, S.W., 2007. Axons of retinal ganglion cells are insulted in the optic nerve early in DBA/2J glaucoma. The Journal of cell biology 179, 1523-1537.

Ivers, K.M., Li, C., Luo, X., Patel, N., Sredar, N., Queener, H., Harwerth, R.S., Porter, J., 2010. Tracking Lamina Cribrosa Pore Geometry in Normal Human and Non-Human Primates Using In Vivo Adaptive Optics Imaging. Invest Ophthalmol Vis Sci 51: E-Abstract 1199.

Ivers, K.M., Li, C., Patel, N., Sredar, N., Luo, X., Queener, H., Harwerth, R.S., Porter, J., 2011. Reproducibility of measuring lamina cribrosa pore geometry in human and nonhuman primates with in vivo adaptive optics imaging. Invest Ophthalmol Vis Sci 52, 5473-5480.

Ivers, K.M., Sredar, N., Patel, N.B., Rajagopalan, L., Queener, H.M., Twa, M.D., Harwerth, R.S., Porter, J., 2015. In Vivo Changes in Lamina Cribrosa Microarchitecture and Optic Nerve Head Structure in Early Experimental Glaucoma. PloS one 10, e0134223.

Jiang, R., Xu, L., Liu, X., Chen, J.D., Jonas, J.B., Wang, Y.X., 2015. Optic nerve head changes after short-term intraocular pressure elevation in acute primary angle-closure suspects. Ophthalmology 122, 730-737.

Joao, S.R., Afonso, M.R., Martins Junior, L., Almeida Junior, B.N., Simoes, R.P., Franca, H.H., 1989. [Jaccoud's syndrome. A case report]. Arquivos brasileiros de cardiologia 53, 221-223.

Johnson, E.C., Morrison, J.C., Farrell, S., Deppmeier, L., Moore, C.G., McGinty, M.R., 1996. The effect of chronically elevated intraocular pressure on the rat optic nerve head extracellular matrix. Experimental eye research 62, 663-674.

Jonas, J.B., Berenshtein, E., Holbach, L., 2003. Anatomic relationship between lamina cribrosa, intraocular space, and cerebrospinal fluid space. Invest Ophthalmol Vis Sci 44, 5189-5195.

Jonas, J.B., Dichtl, A., 1997. Optic disc morphology in myopic primary open-angle glaucoma. Graefe's archive for clinical and experimental ophthalmology = Albrecht von Graefes Archiv fur klinische und experimentelle Ophthalmologie 235, 627-633.

Jonas, J.B., Gusek, G.C., Naumann, G.O., 1988. Optic disk morphometry in high myopia. Graefe's archive for clinical and experimental ophthalmology = Albrecht von Graefes Archiv fur klinische und experimentelle Ophthalmologie 226, 587-590.

Jonas, J.B., Schmidt, A.M., Muller-Bergh, J.A., Schlotzer-Schrehardt, U.M., Naumann, G.O., 1992. Human optic nerve fiber count and optic disc size. Invest Ophthalmol Vis Sci 33, 2012-2018.

Jonas, J.B., Yang, D., Wang, N., 2013. Intracranial pressure and glaucoma. Journal of glaucoma 22 Suppl 5, S13-14.

Jones, B.W., Watt, C.B., Frederick, J.M., Baehr, W., Chen, C.-K., Levine, E.M., Milam, A.H., LaVail, M.M., Marc, R.E., 2003. Retinal remodling triggered by photoreceptor degenerations. The Journal of comparative neurology 464, 1-16.

Jones, H.J., Girard, M.J., White, N., Fautsch, M.P., Morgan, J.E., Ethier, C.R., Albon, J., 2015. Quantitative analysis of three-dimensional fibrillar collagen microstructure within the normal, aged and glaucomatous human optic nerve head. Journal of the Royal Society, Interface / the Royal Society 12.

Kerrigan-Baumrind, L.A., Quigley, H.A., Pease, M.E., Kerrigan, D.F., Mitchell, R.S., 2000. Number of ganglion cells in glaucoma eyes compared with threshold visual field tests in the same persons. Invest Ophthalmol Vis Sci 41, 741-748.

Kim, D.W., Jeoung, J.W., Kim, Y.W., Girard, M.J., Mari, J.M., Kim, Y.K., Park, K.H., Kim, D.M., 2016. Prelamina and Lamina Cribrosa in Glaucoma Patients With Unilateral Visual Field Loss. Invest Ophthalmol Vis Sci 57, 1662-1670.

Knight, O.J., Girkin, C.A., Budenz, D.L., Durbin, M.K., Feuer, W.J., 2012. Effect of race, age, and axial length on optic nerve head parameters and retinal nerve fiber layer thickness measured by Cirrus HD-OCT. Archives of ophthalmology 130, 312-318.

Kotecha, A., Izadi, S., Jeffery, G., 2006. Age-related changes in the thickness of the human lamina cribrosa. The British journal of ophthalmology 90, 1531-1534.

Lee, J.W., Yau, G.S., Woo, T.T., Yick, D.W., Tam, V.T., Lai, J.S., 2015. Retinal nerve fiber layer thickness in myopic, emmetropic, and hyperopic children. Medicine 94, e699.

Leske, M.C., Heijl, A., Hussein, M., Bengtsson, B., Hyman, L., Komaroff, E., 2003. Factors for glaucoma progression and the effect of treatment: the early manifest glaucoma trial. Archives of ophthalmology 121, 48-56.

Li, C., Sredar, N., Ivers, K.M., Queener, H., Porter, J., 2010. A correction algorithm to simultaneously control dual deformable mirrors in a woofer-tweeter adaptive optics system. Optics Express 18, 16671-16684.

Li, K.Y., Roorda, A., 2007. Automated identification of cone photoreceptors in adaptive optics retinal images. J Opt Soc Am A Opt Image Sci Vis 24, 1358-1363.

Malakar, M., Askari, S.N., Ashraf, H., Waris, A., Ahuja, A., Asghar, A., 2015. Optical coherence tomography assisted retinal nerve fibre layer thickness profile in high myopia. Journal of clinical and diagnostic research : JCDR 9, NC01-03.

Marquardt, T., Gruss, P., 2002. Generating neuronal diversity in the retina: one for nearly all. Trends in neurosciences 25, 32-38.

Mayer, M.A., Hornegger, J., Mardin, C.Y., Tornow, R.P., 2010. Retinal Nerve Fiber Layer Segmentation on FD-OCT Scans of Normal Subjects and Glaucoma Patients. Biomedical optics express 1, 1358-1383.

McAllister, J.T., Dubis, A.M., Tait, D.M., Ostler, S., Rha, J., Stepien, K.E., Summers, C.G., Carroll, J., 2010. Arrested development: high-resolution imaging of foveal morphology in albinism. Vision research 50, 810-817.

Mikelberg, F.S., Drance, S.M., Schulzer, M., Yidegiligne, H.M., Weis, M.M., 1989. The normal human optic nerve. Axon count and axon diameter distribution. Ophthalmology 96, 1325-1328.

Minckler, D.S., Bunt, A.H., Johanson, G.W., 1977. Orthograde and retrograde axoplasmic transport during acute ocular hypertension in the monkey. Invest Ophthalmol Vis Sci 16, 426-441.

Mitchell, P., Hourihan, F., Sandbach, J., Wang, J.J., 1999. The relationship between glaucoma and myopia: the Blue Mountains Eye Study. Ophthalmology 106, 2010-2015.

Morrison, J.C., Jerdan, J.A., Dorman, M.E., Quigley, H.A., 1989. Structural proteins of the neonatal and adult lamina cribrosa. Archives of ophthalmology 107, 1220-1224.

Nadler, Z., Wang, B., Schuman, J.S., Ferguson, R.D., Patel, A., Hammer, D.X., Bilonick, R.A., Ishikawa, H., Kagemann, L., Sigal, I.A., Wollstein, G., 2014. In vivo three-dimensional characterization of the healthy human lamina cribrosa with adaptive optics spectral-domain optical coherence tomography. Invest Ophthalmol Vis Sci 55, 6459-6466.

Neufeld, A.H., 1999. Microglia in the optic nerve head and the region of parapapillary chorioretinal atrophy in glaucoma. Archives of ophthalmology 117, 1050-1056.

Neufeld, A.H., Hernandez, M.R., Gonzalez, M., Geller, A., 1997. Cyclooxygenase-1 and cyclooxygenase-2 in the human optic nerve head. Experimental eye research 65, 739-745.

Neufeld, A.H., Sawada, A., Becker, B., 1999. Inhibition of nitric-oxide synthase 2 by aminoguanidine provides neuroprotection of retinal ganglion cells in a rat model of chronic glaucoma. Proceedings of the National Academy of Sciences of the United States of America 96, 9944-9948.

Oliveira, C., Harizman, N., Girkin, C.A., Xie, A., Tello, C., Liebmann, J.M., Ritch, R., 2007. Axial length and optic disc size in normal eyes. The British journal of ophthalmology 91, 37-39.

Oyster, C.W., Takahashi, E.S., Hurst, D.C., 1981. Density, soma size, and regional distribution of rabbit retinal ganglion cells. The Journal of neuroscience : the official journal of the Society for Neuroscience 1, 1331-1346.

Panda, S., Jonas, J.B., 1992. Decreased photoreceptor count in human eyes with secondary angle-closure glaucoma. Invest Ophthalmol Vis Sci 33, 2532-2536.

Park, H.Y., Jeon, S.H., Park, C.K., 2012a. Enhanced depth imaging detects lamina cribrosa thickness differences in normal tension glaucoma and primary open-angle glaucoma. Ophthalmology 119, 10-20.

Park, S.C., Brumm, J., Furlanetto, R.L., Netto, C., Liu, Y., Tello, C., Liebmann, J.M., Ritch, R., 2015. Lamina cribrosa depth in different stages of glaucoma. Invest Ophthalmol Vis Sci 56, 2059-2064.

Park, S.C., Kiumehr, S., Teng, C.C., Tello, C., Liebmann, J.M., Ritch, R., 2012b. Horizontal central ridge of the lamina cribrosa and regional differences in laminar insertion in healthy subjects. Invest Ophthalmol Vis Sci 53, 1610-1616.

Patel, N.B., Lim, M., Gajjar, A., Evans, K.B., Harwerth, R.S., 2014a. Age-associated changes in the retinal nerve fiber layer and optic nerve head. Invest Ophthalmol Vis Sci 55, 5134-5143.

Patel, N.B., Sullivan-Mee, M., Harwerth, R.S., 2014b. The relationship between retinal nerve fiber layer thickness and optic nerve head neuroretinal rim tissue in glaucoma. Invest Ophthalmol Vis Sci 55, 6802-6816.

Perkins, E.S., Phelps, C.D., 1982. Open angle glaucoma, ocular hypertension, low-tension glaucoma, and refraction. Archives of ophthalmology 100, 1464-1467.

Perry, V.H., Cowey, A., 1985. The ganglion cell and cone distributions in the monkey's retina: implications for central magnification factors. Vision research 25, 1795-1810.

Quigley, H., Anderson, D.R., 1976a. The dynamics and location of axonal transport blockade by acute intraocular pressure elevation in primate optic nerve. Investigative ophthalmology 15, 606-616.

Quigley, H.A., 1996. Number of people with glaucoma worldwide. British Journal of Ophthalmology 80, 389-393.

Quigley, H.A., 2011. Glaucoma. Lancet 377, 1367-1377.

Quigley, H.A., Addicks, E.M., 1981. Regional differences in the structure of the lamina cribrosa and their relation to glaucomatous optic nerve damage. Archives of ophthalmology 99, 137-143.

Quigley, H.A., Addicks, E.M., Green, W.R., 1982. Optic nerve damage in human glaucoma. III. Quantitative correlation of nerve fiber loss and visual field defect in glaucoma, ischemic neuropathy, papilledema, and toxic neuropathy. Archives of ophthalmology 100, 135-146.

Quigley, H.A., Addicks, E.M., Green, W.R., Maumenee, A.E., 1981. Optic nerve damage in human glaucoma. II. The site of injury and susceptibility to damage. Archives of ophthalmology 99, 635-649.

Quigley, H.A., Anderson, D.R., 1976b. The Dynamics and Location of Axonal-Transport Blockade by Acute Intraocular-Pressure Elevation in Primate Optic-Nerve. Investigative Ophthalmology 15, 606-616.

Quigley, H.A., Anderson, D.R., 1977. Distribution of axonal transport blockade by acute intraocular pressure elevation in the primate optic nerve head. Invest Ophthalmol Vis Sci 16, 640-644.

Quigley, H.A., Broman, A.T., 2006. The number of people with glaucoma worldwide in 2010 and 2020. The British journal of ophthalmology 90, 262-267.

Quigley, H.A., Brown, A.E., Morrison, J.D., Drance, S.M., 1990. The size and shape of the optic disc in normal human eyes. Archives of ophthalmology 108, 51-57.

Quigley, H.A., Coleman, A.L., Dorman-Pease, M.E., 1991. Larger optic nerve heads have more nerve fibers in normal monkey eyes. Archives of ophthalmology 109, 1441-1443.

Quigley, H.A., Green, W.R., 1979. The histology of human glaucoma cupping and optic nerve damage: clinicopathologic correlation in 21 eyes. Ophthalmology 86, 1803-1830.

Quigley, H.A., Vitale, S., 1997. Models of open-angle glaucoma prevalence and incidence in the United States. Invest Ophthalmol Vis Sci 38, 83-91.

Rajagopalan;, L.P., Patel;, N.B., Sredar;, K.I.N., Viswanathan;, S., Porter;, J., Harwerth;, R.S., Frishman, L.J., 2015. Early changes in structure and inner retinal function in experimental glaucoma, ARVO. IOVS, Denver, CO.

Reis, A.S., O'Leary, N., Yang, H., Sharpe, G.P., Nicolela, M.T., Burgoyne, C.F., Chauhan, B.C., 2012. Influence of clinically invisible, but optical coherence tomography detected, optic disc margin anatomy on neuroretinal rim evaluation. Invest Ophthalmol Vis Sci 53, 1852-1860.

Ren, R., Wang, N., Li, B., Li, L., Gao, F., Xu, X., Jonas, J.B., 2009. Lamina cribrosa and peripapillary sclera histomorphometry in normal and advanced glaucomatous Chinese eyes with various axial length. Invest Ophthalmol Vis Sci 50, 2175-2184.

Rhodes, L.A., Huisingh, C., Johnstone, J., Fazio, M., Smith, B., Clark, M., Downs, J.C., Owsley, C., Girard, M.J., Mari, J.M., Girkin, C., 2014. Variation of laminar depth in normal eyes with age and race. Invest Ophthalmol Vis Sci 55, 8123-8133.

Roberts, M.D., Grau, V., Grimm, J., Reynaud, J., Bellezza, A.J., Burgoyne, C.F., Downs, J.C., 2009a. Remodeling of the Connective Tissue Microarchitecture of the Lamina Cribrosa in Early Experimental Glaucoma. Investigative Ophthalmology & Visual Science 50, 681-690.

Roberts, M.D., Grau, V., Grimm, J., Reynaud, J., Bellezza, A.J., Burgoyne, C.F., Downs, J.C., 2009b. Remodeling of the connective tissue microarchitecture of the lamina cribrosa in early experimental glaucoma. Invest Ophthalmol Vis Sci 50, 681-690.

Rudnicka, A.R., Mt-Isa, S., Owen, C.G., Cook, D.G., Ashby, D., 2006. Variations in primary open-angle glaucoma prevalence by age, gender, and race: a Bayesian meta-analysis. Invest Ophthalmol Vis Sci 47, 4254-4261.

Salinas-Navarro, M., Jimenez-Lopez, M., Valiente-Soriano, F.J., Alarcon-Martinez, L., Aviles-Trigueros, M., Mayor, S., Holmes, T., Lund, R.D., Villegas-Perez, M.P., Vidal-Sanz, M., 2009. Retinal ganglion cell population in adult albino and pigmented mice: a computerized analysis of the entire population and its spatial distribution. Vision research 49, 637-647.

Sanchez, R.M., Dunkelberger, G.R., Quigley, H.A., 1986. The number and diameter distribution of axons in the monkey optic nerve. Invest Ophthalmol Vis Sci 27, 1342-1350.

Seo, J.H., Kim, T.W., Weinreb, R.N., 2014. Lamina cribrosa depth in healthy eyes. Invest Ophthalmol Vis Sci 55, 1241-1251.

Sigal, I.A., Ethier, C.R., 2009. Biomechanics of the optic nerve head. Experimental eye research 88, 799-807.

Sigal, I.A., Flanagan, J.G., Lathrop, K.L., Tertinegg, I., Bilonick, R., 2012. Human lamina cribrosa insertion and age. Invest Ophthalmol Vis Sci 53, 6870-6879.

Sigal, I.A., Flanagan, J.G., Tertinegg, I., Ethier, C.R., 2010. 3D morphometry of the human optic nerve head. Experimental eye research 90, 70-80.

Sigal, I.A., Grimm, J., Jan, N.-J., Bilonick, R., Wollstein, G., Kagemann, L., Ishikawa, H., Schuman, J., Davoli, K., Lathrop, K., 2013. IOP Elevation Reduces the Waviness of the

Load Bearing Collagen Fibers in the Lamina Cribrosa, ARVO. Investigative Ophthalmology and Visual Science.

Silveira, L.C., Picanco-Diniz, C.W., Sampaio, L.F., Oswaldo-Cruz, E., 1989. Retinal ganglion cell distribution in the cebus monkey: a comparison with the cortical magnification factors. Vision research 29, 1471-1483.

Spoerl, E., Boehm, A.G., Pillunat, L.E., 2005. The influence of various substances on the biomechanical behavior of lamina cribrosa and peripapillary sclera. Invest Ophthalmol Vis Sci 46, 1286-1290.

Sredar, N., Ivers, K.M., Queener, H.M., Zouridakis, G., Porter, J., 2013. 3D modeling to characterize lamina cribrosa surface and pore geometries using in vivo images from normal and glaucomatous eyes. Biomedical optics express 4, 1153-1165.

Strouthidis, N.G., Fortune, B., Yang, H., Sigal, I.A., Burgoyne, C.F., 2011. Longitudinal change detected by spectral domain optical coherence tomography in the optic nerve head and peripapillary retina in experimental glaucoma. Invest Ophthalmol Vis Sci 52, 1206-1219.

Tezel, G., 2009. The role of glia, mitochondria, and the immune system in glaucoma. Invest Ophthalmol Vis Sci 50, 1001-1012.

Tezel, G., Luo, C., Yang, X., 2007. Accelerated aging in glaucoma: immunohistochemical assessment of advanced glycation end products in the human retina and optic nerve head. Invest Ophthalmol Vis Sci 48, 1201-1211.

Thakku, S.G., Tham, Y.C., Baskaran, M., Mari, J.M., Strouthidis, N.G., Aung, T., Cheng, C.Y., Girard, M.J., 2015. A Global Shape Index to Characterize Anterior Lamina Cribrosa Morphology and Its Determinants in Healthy Indian Eyes. Invest Ophthalmol Vis Sci 56, 3604-3614.

Tham, Y.C., Li, X., Wong, T.Y., Quigley, H.A., Aung, T., Cheng, C.Y., 2014. Global prevalence of glaucoma and projections of glaucoma burden through 2040: a systematic review and meta-analysis. Ophthalmology 121, 2081-2090.

Wang, B., Nevins, J.E., Nadler, Z., Wollstein, G., Ishikawa, H., Bilonick, R.A., Kagemann, L., Sigal, I.A., Grulkowski, I., Liu, J.J., Kraus, M., Lu, C.D., Hornegger, J., Fujimoto, J.G., Schuman, J.S., 2013. In vivo lamina cribrosa micro-architecture in healthy and glaucomatous eyes as assessed by optical coherence tomography. Invest Ophthalmol Vis Sci 54, 8270-8274.

Wang, J., Li, T., Sabel, B.A., Chen, Z., Wen, H., Li, J., Xie, X., Yang, D., Chen, W., Wang, N., Xian, J., He, H., 2016. Structural brain alterations in primary open angle glaucoma: a 3T MRI study. Scientific reports 6, 18969.

Weber, A.J., Kaufman, P.L., Hubbard, W.C., 1998. Morphology of single ganglion cells in the glaucomatous primate retina. Invest Ophthalmol Vis Sci 39, 2304-2320.

Wu, Z., Xu, G., Weinreb, R.N., Yu, M., Leung, C.K., 2015. Optic Nerve Head Deformation in Glaucoma: A Prospective Analysis of Optic Nerve Head Surface and Lamina Cribrosa Surface Displacement. Ophthalmology 122, 1317-1329.

Xu, L., Wang, Y., Wang, S., Jonas, J.B., 2007. High myopia and glaucoma susceptibility the Beijing Eye Study. Ophthalmology 114, 216-220.

Yang, G., Stewart, C.V., Sofka, M., Tsai, C.L., 2007a. Registration of challenging image pairs: initialization, estimation, and decision. IEEE transactions on pattern analysis and machine intelligence 29, 1973-1989.

Yang, H., Downs, J.C., Bellezza, A., Thompson, H., Burgoyne, C.F., 2007b. 3-D histomorphometry of the normal and early glaucomatous monkey optic nerve head: prelaminar neural tissues and cupping. Invest Ophthalmol Vis Sci 48, 5068-5084.

Yang, H., Downs, J.C., Burgoyne, C.F., 2009. Physiologic intereye differences in monkey optic nerve head architecture and their relation to changes in early experimental glaucoma. Invest Ophthalmol Vis Sci 50, 224-234.

Yang, H., Downs, J.C., Girkin, C., Sakata, L., Bellezza, A., Thompson, H., Burgoyne, C.F., 2007b. 3-D histomorphometry of the normal and early glaucomatous monkey optic nerve head: lamina cribrosa and peripapillary scleral position and thickness. Invest Ophthalmol Vis Sci 48, 4597-4607.

Yang, H., Ren, R., Lockwood, H., Williams, G., Libertiaux, V., Downs, C., Gardiner, S.K., Burgoyne, C.F., 2015. The Connective Tissue Components of Optic Nerve Head Cupping in Monkey Experimental Glaucoma Part 1: Global Change. Invest Ophthalmol Vis Sci 56, 7661-7678.

Yang, H., Thompson, H., Roberts, M.D., Sigal, I.A., Downs, J.C., Burgoyne, C.F., 2010. Deformation of the Early Glaucomatous Monkey Optic Nerve Head Connective Tissue Following Acute IOP Elevation within 3-D Histomorphometric Reconstructions. Invest Ophthalmol Vis Sci.

Yucel, Y.H., Zhang, Q., Gupta, N., Kaufman, P.L., Weinreb, R.N., 2000. Loss of neurons in magnocellular and parvocellular layers of the lateral geniculate nucleus in glaucoma. Archives of ophthalmology 118, 378-384.

Zwillinger, S., Paques, M., Safran, B., Baudouin, C., 2016. In vivo characterization of lamina cribrosa pore morphology in primary open-angle glaucoma. Journal francais d'ophtalmologie 39, 265-271.